Synchronisation in Open Quantum Systems

Claire Davis-Tilley, MPhys

Thesis submitted to The University of Nottingham
for the degree of Doctor of Philosophy

October 2017

"There are exactly three numbers: 0, 1, and ∞.
The use of anything else is a form of dandyism."

—*Zach Weinersmith*

Abstract

Synchronisation has been explored extensively for classical systems from the mid-1600s, and is a phenomenon widely understood in many diverse systems. In the age of technology miniaturisation, there are great incentives to develop an understanding of quantum synchronisation, where quantum fluctuations become the dominant source of noise and non-classical features become important. This thesis considers different types of synchronisation in systems that can display highly non-linear, quantum behaviours.

Phase synchronisation for a micromaser coupled to an external drive is initially considered, and it is found that for low photon numbers a semiclassical approximation underestimates phase synchronisation, but a perturbation theory can be accurate for sufficiently weak coupling in either a quantum or semiclassical regime. When a small detuning between the drive and micromaser is introduced, frequency entrainment is also found to exist.

Then two micromasers are coupled with each other, in two different configurations, and synchronisation through a relative phase preference is found for each. A semiclassical approximation once again underestimates the phase synchronisation. Entanglement and mutual information are found to behave differently to the relative phase preference depending on each system's parameters.

Finally, a mean-field theory is considered for many coupled van der Pol oscillators and micromasers respectively. As the coupling between the oscillators is increased, a critical point is reached and the systems undergo a transition to a phase synchronised state. This bistability appears via a saddle-node bifurcation, and in addition to examining a variety of properties before and after the transition the critical scaling behaviour was investigated close to the transition.

Acknowledgements

Foremost, I wish to thank Andrew Armour for his unconditional support, guidance, encouragement and kindness. It has certainly made my journey here an enjoyable one.

Thank you to my friends and colleagues in C18 and beyond, for making it a pleasure to come into work. May my happy memories be as permanent as the doge on the whiteboard.

And much appreciation goes to my family, who have always been so supportive. Thank you Freddie – the original Dr. Davis-Tilley – for continuing to be the best partner I could ask for, and for providing me with as many cups of tea as I could drink.

List of Figures

1.1 Optical microscope images of optomechanical oscillator arrays, and the frequency peaks that indicate synchronisation [14]. (Reprinted with permission from American Physical Society © 2015.) 3

2.1 An example of a limit cycle in phase space with the dashed lines illustrating the path towards the stable limit cycle from different starting conditions. 6

2.2 The Wigner distribution[1]of a van der Pol oscillator, calculated using the steady state of Eq. 2.1.5 with $\kappa_2/\kappa_1 = 0.04$. The ring shape shows a clearly defined limit cycle, and the even distribution around the ring shows that there is no phase preference. 9

2.3 The passage of an atom excited to a Rydberg state $|e\rangle$ through a microwave cavity containing n photons. The atom undergoes Rabi oscillations and emerges in either the excited state or the ground state $|g\rangle$ depending on the time it has spent travelling through the cavity. 10

2.4 (a) Average photon occupation number $\langle n\rangle$ and (b) Fano factor F as a function of the pump parameter $\Theta = \phi N^{1/2}$ and N in the steady state. 11

2.5 The Wigner distribution of a micromaser at $N = 50$ (a) before ($\Theta = 0.5$) and (b) after ($\Theta = 2$) the masing threshold. Limit cycle states only exist in the micromaser above the threshold. 13

2.6 Examples of some interesting states the micromaser can produce. (a) Probability distributions $P(n) = \langle n|\rho|n\rangle$ for the micromaser at a trapping state location, $\Theta = 9.069$. The top distribution has the number of thermal photons set to $\nu = 0.4$, whereas the lower distribution is at zero temperature ($\nu = 0$). (b) $P(n)$ is shown for a wider range of Θ for $\nu = 0$, and $\langle n\rangle$ (solid black line) is overlaid showing sharp transitions in photon numbers where there are trapping states. (c) $P(n)$ at $\Theta = 7.467$, the location of a bistable state. (d) The same bistable state shown as a Wigner distribution. $N = 50$ for all plots. 14

2.7 Capturing the quantum behaviour of the system, at $N = 5$. (a) The average number of photons $\langle n\rangle$ (solid) and the Fano factor, F (dashed). A Fano factor below one describes a sub-Poissonian photon distribution, which combined with the very low photon number is a good indication of a strongly quantum state. (b) A Wigner function for the micromaser that has large negative regions, something not possible with classical distributions, is another quantum indicator. Here $N = 5$, $\Theta = 4.97$. 16

2.8 A circuit diagram of a micromaser-like setup [68, 69]. Two Josephson junctions (with capacitances C_J) are connected to a gate voltage V_g to make a Cooper-pair transistor which can be tuned to have two prominent energy levels, chosen to resonate with the oscillator mode. The oscillator consists of an inductor L_0 and capacitor C_0, which is excited by a flow of charges when a voltage V is applied across the circuit. 17

3.1 Frequency locking, where the difference in oscillator frequencies $\Delta\omega$ reaches zero (shaded), occurs over a limited range of initial detuning $\Delta\omega_0$. The size of this range is determined by the coupling strength. 21

3.2 Schematic representation of regions where synchronisation can occur as a function of the coupling between two oscillators, ε and their initial frequency difference $\Delta = \omega_0 - \omega$. The synchronised regions take the form of Arnold tongues [2]. Usually the largest tongue is located at $\Delta = 0$. 23

3.3 An illustrative example of the phase distribution $P(\varphi)$ plotted for a driven micromaser. For zero drive the function is flat at $1/2\pi$. For the driven case, the function is sinusoidal and 2π-periodic; the stronger the drive, the higher the peak of $P(\varphi)$. 26

4.1 Wigner distributions of an undriven micromaser (left) and driven micromasers at $\varepsilon = 0.01$ (middle) and $\varepsilon = 0.1$ (right), all at $N = 50$, for (a) $\Theta = 1.040$, (b) $\Theta = 4.756$, (c) $\Theta = 7.467$ and (d) $\Theta = 9.069$. The axes are the same for each distribution. 32

4.2 Average photon occupation number $\langle n \rangle / \langle n \rangle_0$ (solid line) and Fano factor F/F_0 (dashed line) as a function of the coupling strength ε at $N = 50$, for (a) $\Theta = 1.040$, (b) $\Theta = 4.756$, (c) $\Theta = 7.467$ and (d) $\Theta = 9.069$. The same measures are inset for a larger range of ε. 33

4.3 Measuring phase synchronisation in the form of (a) $|\langle a \rangle| / \langle n \rangle^{1/2}$ (b) R, both as a function of coupling strength ε for four different values of Θ at $N = 50$. 35

4.4 The FWHM of the spectrum $S(\omega)$ as a function of Θ for (a) $N = 5$, (b) $N = 50$. The numerical calculation (solid line) is compared with the semiclassical approximation (Eq. 4.1.16, dashed line) and large-$\langle n \rangle$ approximation (Eq. 4.1.19, dot-dashed line). 38

4.5 R as a function of Θ at $\varepsilon = 0.01$ for (a) $N = 5$ and (b) $N = 50$: a comparison of (i) numerical, (ii)-(iii) perturbation and (iv)-(v) semiclassical calculations. (ii) is Eq. 4.1.22, and (iii) is Eq. 4.1.23. The semiclassical calculations use Eq. 4.1.20 with $\bar{D}$ given by (iv) Eq. 4.1.19 and (v) Eq. 4.1.16. The inset figures compare the numerical (R) and perturbation (R_{pt}) calculations for different coupling strengths ε. 42

4.6 (a) A (not to scale) illustration of the expected power spectrum for the driven micromaser system. There is a delta peak at the drive frequency ω_d, but the micromaser frequency spectrum should be described by a Lorentzian function with a peak at ω_{mm} due to noise arising from quantum fluctuations. (b) A numerical calculation of the micromaser spectrum with a detuning of $\Delta = 0.2$ for increasing drive strengths. The vertical line is a reference at ω_0, the natural frequency of the oscillator, while ω is the frequency with respect to the drive frequency so that $\Delta = \omega_0$. Here, $N = 10$, $\Theta = 2$ and the delta-peak has been subtracted off. 43

4.7 ω_{mm} as a function of detuning, Δ, at $N = 50$ for different values of ε for (a) $\Theta = 1.040$ and (b) $\Theta = 4.756$ 44

4.8 ω_{mm} as a function of detuning, Δ, at $\Theta = 2$ for (a) $N = 5$ and (b) $N = 50$. The numerical calculations (solid lines) are compared with a semiclassical approximation (dashed lines) at $\varepsilon = 0.01$. 46

4.9 (a) The potential $V(\varphi) = \Delta\varphi + (\varepsilon/\sqrt{\langle n \rangle}) \sin\varphi$ for a micromaser driven on and off-resonance, at $N = 50$, $\Theta = 2$, $\varepsilon = 1$. (b) The phase probability distribution $P(\varphi)$ on- and off-resonance, calculated at $N = 50$, $\Theta = 2$, $\varepsilon = 0.01$. 47

4.10 R as a function of detuning, Δ, at $N = 50$ for (a) $\Theta = 1.040$ and (b) $\Theta = 4.786$. The numerical calculations (solid lines) are compared with a semiclassical approximation (dashed lines) for different values of the coupling strength ε. 48

5.1 A schematic diagram of two coherently coupled micromasers. The micromasers are separately pumped and are joined by a partially reflecting mirror so that photons may tunnel between each cavity. 52

5.2 Average photon number $\langle n \rangle$ and Fano factor F as a function of Θ for increasing coupling strength at $N = 5$. (a) A single driven micromaser (b) one of two coherently coupled micromasers (c) one of two dissipatively coupled micromasers. . . 54

5.3 The photon probability distribution $P(n)$ over n with increasing ε at $N = 5$ for (a) a single driven micromaser and (b) one of two coherently coupled micromasers. For each system four values of Θ are shown (clockwise from top-left): $\Theta = 0.9619$, $\Theta = 2.998$, $\Theta = 7.022$ and $\Theta = 4.5$. 56

5.4 The photon probability distribution $P(n)$ over n with increasing ε at $N = 5$ for the bistable state at $\Theta = 5.8$. (a) A single driven micromaser, (b) one of two coherently coupled micromasers, and (c) one of two dissipatively coupled micromasers. 57

5.5 (a) The relative phase probability distributions for the coherent (black, solid) and dissipative (blue, dashed) coupled micromasers with $\varepsilon = 0.1$. (b) R as a function of the coupling strength ε, where the dotted lines are the perturbation theories developed in Sec. 5.2.2. For both, $N = 5$ and $\Theta = 2$. . . . 59

5.6 For the dissipatively coupled system at $N = 5$, a comparison over Θ of R (solid), calculated using the full master equation, with (a) the semiclassical approximation and (b) the perturbation theory of R (both dashed) for three values of the coupling strength ε. Inset are the relative values of the approximations and the numerical solutions to R, for each value of ε. (c) The behaviour of the average photon number for the same parameters and coupling values as for (a) and (b), with a dashed line as the reference for the uncoupled case. 64

5.7 For the dissipatively coupled system, the relative difference between the semiclassical and perturbation calculations for increasing values of N at $\varepsilon = 0.0001$. 65

5.8 (a) Mutual information $\mathcal{I}$ as a function of the coupling strength ε for coherent (solid) and dissipative (dashed) couplings, at $\Theta = 2$. In the dissipatively coupled system, a comparison of (b) R and (c) the mutual information as a function of the detuning for three values of the coupling strength, at $\Theta = 1$ (solid) and $\Theta = 2$ (dashed). 67

5.9 (a) Entanglement calculated by logarithmic negativity as a function of Θ at $\varepsilon = 0.5$, with the locations of trapping states indicated by the dotted lines. (b) Entanglement at the trapping state $\Theta = 4.97$ as a function of ε for the two coupled systems. The solid lines are for the coherently coupled system, and the dashed are for the dissipatively coupled system, with $N = 5$. 68

6.1 The evolution of (a) $|\langle a \rangle|$ and (b) $\langle a \rangle$ as the self-consistent master equation converges towards a steady state, from $\varepsilon = 1.5$ (dark blue) to $\varepsilon = 3.9$ (light yellow). Here, $\kappa_2/\kappa_1 = 0.04$. . 73

6.2 (a) Looking at the final decay of $|\langle a \rangle|$ for $\varepsilon = 2.9$ in detail. (b)–(f) The photon number probability distribution $P(n)$ and the Wigner function (inset) for different times in the decay, indicated in (a). Here, $\kappa_2/\kappa_1 = 0.04$. 74

6.3 An illustration of how looking at effective potentials could help in understanding the evolution of $|\langle a \rangle|$ at (a) ε above a critical value (b) close to, but below, a critical value and (c) well below a critical value. 76

6.4 (a) An illustration of how the van der Pol system displays a saddle-node bifurcation, with stable (solid) and unstable (dashed) fixed points appearing as ε is increased. (b) The evolution of $|\langle a \rangle|$ at $\varepsilon = 3$ for various values of α_{init} that create the initial state. (c) The critical values of initial conditions (green points), which represent the unstable fixed points. (b) and (c) are for $\kappa_2/\kappa_1 = 0.04$. 77

6.5 Plots of the time taken for $|\langle a \rangle|$ to decay to zero, $t_{|\langle a \rangle|=0}$, for different values of the coupling ε approaching the transition for (a) $\kappa_2/\kappa_1 = 0.04$ and (b) $\kappa_2/\kappa_1 = 0.02$. For (c) and (d) the same data is plotted on logarithmic axes, with the x-axis showing ε in relation to the estimated critical point $\varepsilon_{\text{crit}}$. The solid lines are taken from fitting the data points close to the transition. 79

6.6 (a) The steady state values of some key quantities in the system across the synchronisation transition in ε. (b) An example of how some of these quantities evolve in time below the critical coupling value, in this case $\varepsilon = 2.7$. For both, $\kappa_2/\kappa_1 = 0.04$. 82

6.7 The evolution of $|\langle a \rangle|$ with time, for $\Theta = 2$, and a range of coupling values ε up to the locking transition for (a) $N = 20$ ($\varepsilon = 0.5$–1.3), (d) $N = 50$ ($\varepsilon = 0.5$–0.7). In each case the photon number distribution $P(n)$ and the Wigner function are shown for the unlocked state [$\varepsilon = 0$ for (b) and (e)] and the locked state [(c) $\varepsilon = 1.3$, (f) $\varepsilon = 0.7$]. 84

6.8 (a) Plot of the most probable number of photons (n at which $P(n)$ is peaked) as a function of the time taken to decay into an unsynchronised steady state, with $N = 25$ and $\Theta = 2$. (b) A comparison of the most probable number of photons for $N = 20$, $\varepsilon = 1.27$ and $N = 50$, $\varepsilon = 0.67$ with $\Theta = 2$. For both values of N, $(\varepsilon_{\text{crit}} - \varepsilon) \approx 0.02$. 85

6.9 The critical value of the initial state α_{crit} plotted as a function of the distance from the critical point in ε for (a) $N = 20$ and $N = 50$, and (b) a larger range for $N = 20$, with $\Theta = 2$. The dashed lines are fits to the points, assuming a parabolic curve that is most accurate for small values of $\varepsilon - \varepsilon_{\text{crit}}$. 86

6.10 Plots of the time taken for $|\langle a \rangle|$ to decay to zero, $t_{|\langle a \rangle|=0}$, for different values of the coupling ε approaching the synchronisation transition for $\Theta = 2$ and (a) $N = 20$ and (b) $N = 50$. For (c) and (d) the same data is plotted on logarithmic axes, with the x-axis showing ε in relation to the estimated critical point $\varepsilon_{\text{crit}}$. The solid lines are taken from fitting the data points close to the transition. 87

6.11 (a) The critical value of coupling ε and (b) a predicted range for the slope that determines the power law exponent, plotted against $1/N$ for $\Theta = 2$. The semiclassical limit is approached as $1/N \to 0$. The method for creating the range in uncertainty is detailed in Appendix E.3, and for (a) the error bars are smaller than the marker size. 89

6.12 The steady-state values of some key quantities, and their uncertainties, in the micromaser systems as they transition to a synchronised regime in ε for $\Theta = 2$. Below are example evolutions of the decay to an unsynchronised state. (a), (c) $N = 20$ and (b), (d) $N = 50$. For (c) and (d) $(\varepsilon_{\text{crit}} - \varepsilon) \simeq 0.02$. 90

6.13 (a) Comparing the uncertainties in number and phase for the unsynchronised $(\Delta n_0,\ \Delta\varphi_0)$ and synchronised $(\Delta n_{\text{sync}},\ \Delta\varphi_{\text{sync}})$ states as a function of Θ. For each value of Θ, the ε value used for the synchronised state is double the value of $\varepsilon_{\text{crit}}$ for that Θ. (b) The difference between the synchronised and unsynchronised states for Δn and $\Delta\varphi$, plotted as the relative change from the first value at $\Theta = 1.35$. Here, $N = 20$ throughout. . 91

6.14 A map of how Θ affects the critical transition point in ε for (a) $N = 20$ and (b) $N = 50$. The dashed lines indicate the maximum in $\langle n \rangle$ and the dotted lines indicate the minimum in the linewidth. 92

6.15 The evolution over time of the vdP oscillator for (a) $\psi = 0$, (b) $\psi = \pi/2$, (c) $\psi = 3\pi/2$, and (d) $\psi = \pi$ with $\kappa_2/\kappa_1 = 0.04$. 95

A.1 Visualising the evolution of the density matrix in terms of the individual processes from Eq. 4.1.11 to understand the conditions needed for detailed balance in this system. 99

E.1 Showing how the value of $\varepsilon_{\text{crit}}$ affects the shape of the curve in the micromaser system with $N = 20$ and $\Theta = 2$. The different curves use the same data with $\varepsilon_{\text{crit}}$ ranging from 1.278—1.286. 115

E.2 Fitting a linear model to a range of five consecutive points, with the point closest to the transition denoted by ε_{max}, for (a) $\kappa_2/\kappa_1 = 0.04$ and (b) $\kappa_2/\kappa_1 = 0.02$ in the van der Pol oscillator system. For each selection of points, $\varepsilon_{\text{crit}}$ is varied until there is a maximum in the coefficient of determination, R^2, and then b is extracted. 116

E.3 Showing how the minimum and maximum estimated values of $\varepsilon_{\text{crit}}$ affect the value of the slope b for (a) $N = 20$ and (b) $N = 50$ in the micromaser system with $\Theta = 2$. 117

Contents

1 Introduction **1**

1.1 The Outline of the Thesis 4

2 Self-Sustained Oscillators **6**

2.1 The van der Pol Oscillator 7

2.2 The Micromaser 9

2.3 Realising Quantum Self-Sustained Oscillators 15

2.3.1 Circuit Quantum Electrodynamics 16

2.3.2 Optomechanical and Spin Systems 18

3 Synchronisation **20**

3.1 Classical Synchronisation 20

3.1.1 Noise 23

3.2 Quantum Synchronisation 24

3.2.1 Measures of Synchronisation in Quantum Systems . 25

4 A Driven Micromaser **29**

4.1 On-resonance 30

4.1.1 Properties of a driven micromaser 30

4.1.2 Predicting the phase preference 33

4.1.3 Measures of the phase preference 34

4.1.4 The micromaser linewidth 35
4.1.5 Semiclassical phase distribution 39
4.1.6 Perturbation theory description 39
4.1.7 Comparison of results 40
4.2 Off-resonance 43
4.2.1 Frequency Spectrum and Entrainment 43
4.2.2 Semiclassical approximation of the common frequency 45
4.2.3 Phase synchronisation 46
4.3 Summary and Conclusions 49

5 Two Coupled Micromasers 51
5.1 Properties of the systems 52
5.1.1 Coherent and Dissipative Couplings 52
5.1.2 Comparison of Couplings 53
5.2 Relative Phase Distribution 58
5.2.1 Semiclassical Approximation 60
5.2.2 Perturbation Theory 61
5.2.3 Comparison of Approximations to Numerical Solution 63
5.3 Mutual Information and Entanglement 65
5.3.1 Mutual information 66
5.3.2 Entanglement 66
5.4 Summary and Conclusions 69

6 Many-Body Quantum Synchronisation 71
6.1 Coupled Quantum van der Pol Oscillators 72
6.1.1 Bistability and the Nature of the Transition 75
6.1.2 Scaling at the Critical Point 78
6.1.3 Phase and number uncertainties 80

6.2 Coupled Micromasers 83
6.2.1 State Evolution and Bistability 83
6.2.2 Critical Scaling 86
6.2.3 Properties of the Transition in Parameter Space 89
6.3 Summary and Conclusions 93
6.4 Future Directions 94

Appendices **97**

A Semiclassical approximations for a single driven micromaser **98**
A.1 On-resonance calculation of the phase diffusion constant . . 98
A.2 Off-resonance 100
A.2.1 Analytic Frequency Calculation 100
A.2.2 Generalisation of the semiclassical phase distribution 102

B Perturbation theory for a single driven micromaser **104**
B.1 Full perturbation theory 104
B.2 Simplified perturbation theory 106

C Two dissipatively coupled micromasers **107**

D Semiclassical calculation for two dissipatively coupled micromasers **109**

E Methodology for Many-Body Quantum Synchronisation **112**
E.1 Runge-Kutta Method 113
E.2 Details in Methodology 113
E.3 Errors in the Critical Scaling 114

References **118**

Chapter 1

Introduction

Ever since Christiaan Huygens recorded the behaviour of two coupled clock pendulums in the 17th century [1], the phenomenon of synchronisation has been recognised and exploited in an incredibly wide-ranging assortment of physical systems. Through understanding it, we can better understand emergent properties of systems that are otherwise too large and complex to model easily. Synchronisation has been useful in describing physiological systems, astrophysical systems, ecosystems, chemistry, electronics and even music [2] to name just a few. It has been extensively studied in classical systems, but as miniaturisation of technology progresses it is becoming increasingly relevant to explore synchronisation on much smaller scales where non-classical features could have interesting effects.

Synchronisation occurs when the phase and frequency of oscillators tend towards a common value due to the oscillators' mutual influence on each other. In nature, a common form of synchronisation is the collective synchronisation of vast arrays of coupled oscillators. As this type of synchronisation can explain behaviour as diverse as animal flock behaviours to cells and neural networks, much early work was biologically and physiologically focussed [3]. In physics, a key area of study was coupled laser arrays. Though under certain circumstances they could synchronise [4], the non-linearity in laser systems could also give rise to unstable complex and chaotic behaviour [5].

In addition to the mutual, spontaneous synchronisation of many oscillators there can also exist a "forced" synchronisation of an oscillator to a more

dominant drive, which can produce quite different behaviour. Understanding how oscillators work on extremely small scales is a key step that will eventually lead to being able to manage noise and decoherence effects, primary challenges in technology miniaturisation and quantum information processing [6]. There is therefore an incentive to explore synchronisation on progressively smaller scales, and there have been several successful experimental implementations of synchronisation on these scales such as optomechanical systems [7–9] and with proposals to use superconducting circuit components such as Josephson junctions [10, 11]. In 2005, nanoscale mutual phase synchronisation was experimentally achieved with two spin torque nano-oscillators [12], with a view to eventually constructing arrays of similar oscillators that could have applications in nanoscale technology such as wireless communications.

Micro- and nanomechanical oscillators are often chosen to study synchronisation, coupled either mechanically or optically. A successful demonstration of the synchronisation of two nanomechanical oscillators coupled mechanically was achieved in 2007 [13], where multiple regions of frequency entrainment were observed. Up to this point it was experimentally challenging to observe synchronisation in arrays of more than two, but in 2015 synchronisation was demonstrated for arrays of three, four, and seven optically coupled micromechanical oscillators [14] (shown in Fig. 1.1).

Though these systems contain extremely small components, they do not yet demonstrate synchronisation in the quantum regime. Quantum synchronisation has been looked at theoretically [15, 16] for systems such as optomechanical arrays [17], quantum dipoles [18], trapped ions [19], and van der Pol oscillators with suggestions for experimental realisations [20].

Noise can significantly affect the collective behaviour of oscillators and for classical systems this is mostly thermal, but quantum systems have an additional source of noise in the form of zero-point fluctuations. Noise in classical systems can have diverse effects, from destroying synchronisation to inducing it [21, 22]. How zero-point fluctuations – plus phenomena such as entanglement – relate to synchronisation are important points to consider as quantum technology progresses. New synchronisation measures may also be considered in quantum systems, such as information-based correlations [16]. A key consideration is that quantum phase is less clearly de-

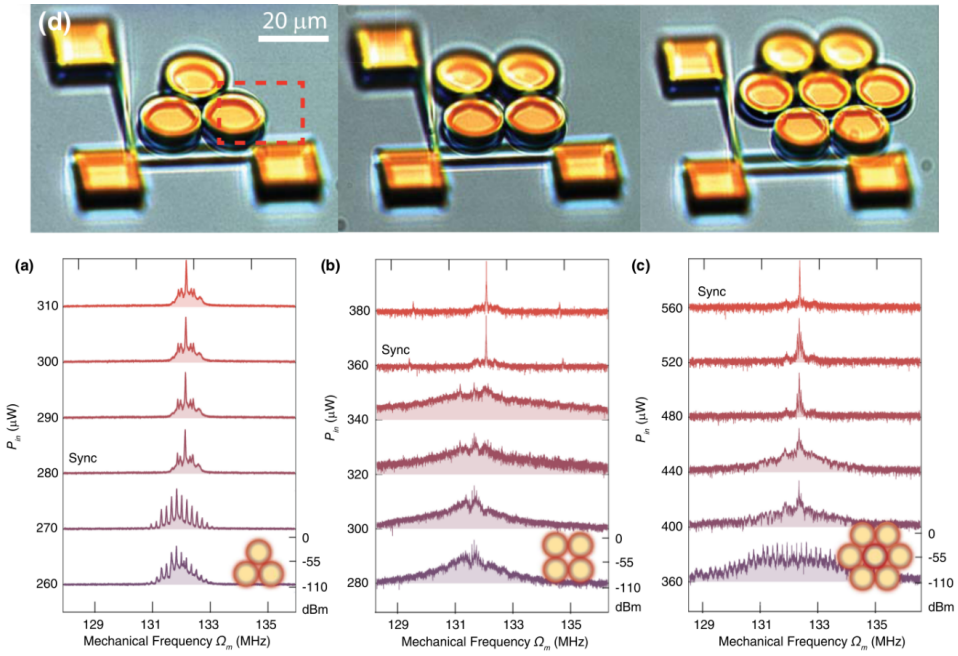


Figure 1.1: Optical microscope images of optomechanical oscillator arrays, and the frequency peaks that indicate synchronisation [14]. (Reprinted with permission from American Physical Society © 2015.)

fined than its classical counterpart, and the question of how best to quantify quantum synchronisation is still open.

In this thesis we look predominantly to the micromaser to try to address some of these questions. The micromaser is an interesting non-linear oscillator that can produce clearly defined limit cycles, and can also exhibit some complex, highly quantum behaviour with a variety of dynamical states. By tuning the parameters we are able to study these states from close to the quantum limit up to a semiclassical one, and hence gain a comprehensive picture of quantum synchronisation for the system.

1.1 The Outline of the Thesis

Chapter 2 introduces the concept of self-sustained oscillators, and looks in more detail at the van der Pol oscillator and the micromaser, the two quantum systems that will be studied in this thesis. Some other realisations of quantum self-sustained oscillators are discussed, including superconducting circuits and optomechanical systems.

Chapter 3 reviews the main topic of the thesis: synchronisation. Firstly, a brief overview of classical synchronisation is provided, including the effect that noise has in a system. This is followed by a brief summary of recent work that has been done looking at synchronisation in quantum systems, where noise from quantum fluctuations can become equally or more important than thermal fluctuations. The question of how to quantify synchronisation in quantum systems is explored, and several potential measures are discussed.

The first chapter of original research, chapter 4, looks at a micromaser subject to an external drive. This system exhibits non-linear and non-classical properties, many of which are very sensitive to the external drive. A selection of diverse states are examined, and phase synchronisation is explored throughout a range of parameters, including one that strongly influences the classicality of the system. Semiclassical approximations describe phase synchronisation well if photon numbers are high, and a perturbation theory also does well in the limit of weak drive strength. Frequency synchronisation is explored briefly using the power spectrum, and a weak frequency entrainment is discovered when the drive frequency is off-resonant.

Chapter 5 looks at two micromasers, coupled to each other in two different ways – coherently and dissipatively. After a comparison of the behaviour of the two systems, synchronisation is measured by the relative phase of the oscillators for a range of parameters. A perturbation theory for the dissipative system is accurate at predicting phase synchronisation for weak coupling. A semiclassical approximation underestimates the phase synchronisation, but an exact (numerical) solution is computationally restricted to the quantum regime, and the semiclassical approximation is expected to improve as the average photon number increases. Entanglement (calculated by the logarithmic negativity) and mutual information are found to behave quite differently to each other, and to the relative phase for both coupled micromaser systems.

Chapter 6 examines the synchronisation of many, globally coupled oscillators. Here, the van der Pol oscillator is also studied in addition to the micromaser. A transition occurs as the coupling strength is increased beyond a critical point, where a bifurcation occurs and phase synchronisation suddenly appears as a steady-state solution. The timescales taken to decay to the unsynchronised state are examined approaching the critical point, and power-law scaling is seen. Synchronisation is associated with a drop in photon numbers for both the van der Pol and micromaser systems. The expected decrease in phase uncertainty in the synchronised state is found to correspond with an increase in number uncertainty, suggesting that synchronisation in quantum systems could be considered as a transition between number-ordered and phase-ordered states.

The results in chapters 4–6 are from original research undertaken in collaboration with Andrew Armour. The key results in chapter 5 are published in [23]. The results in chapter 6 are currently being prepared for future publication.

Chapter 2

Self-Sustained Oscillators

Self-sustained oscillators are dynamical non-linear systems that have many interesting features, and are found in abundance in both the natural and technological worlds [24]. They are autonomous subsystems that interact with their environment in such a way that energy gained is equal to the energy lost and a stable oscillating state is found. All physical systems must be coupled to the environment in some way and experience dissipation, but the damping in self-sustained oscillators is in general non-linear and balanced by an internal negative damping so that their oscillations do not decay with time – the oscillations do not have a need for an external "kick" to remain constant. This balance of negative and non-linear damping is the defining feature of the self-sustained oscillator, the non-linear property being essential in achieving synchronisation.

We can visualise the properties of self-sustained oscillators using limit cycles in phase space (Fig. 2.1). The oscillations trace out a clearly defined periodic cycle in phase space, and the amplitude of the oscillators are dictated by the rates of non-linear and negative damping – independent of the

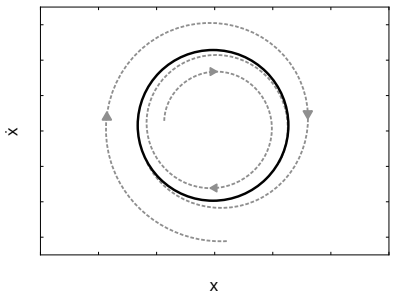


Figure 2.1: An example of a limit cycle in phase space with the dashed lines illustrating the path towards the stable limit cycle from different starting conditions.

initial conditions. They will also remain stable: if perturbed, they will reliably fall back into their limit cycle as illustrated by the grey dashed lines in Fig. 2.1.

This chapter will introduce the two self-sustained oscillators studied in this thesis: the van der Pol oscillator and the micromaser. The van der Pol oscillator, introduced in Sec. 2.1, has been studied extensively to model a wide variety of systems, and its quantum analogue has recently been used to explore quantum synchronisation [20, 25–27]. Section 2.2 discusses the micromaser, a laser on the smallest possible scale with a single atom interacting with a cavity mode at microwave frequencies. Due to its interesting quantum properties it is the self-sustained oscillator that is the primary focus of this thesis. Other types of quantum self-sustained oscillators are also briefly discussed in Sec. 2.3, covering superconducting quantum circuits, optomechanical systems and spin/two-level systems.

2.1 The van der Pol Oscillator

The classical van der Pol (vdP) oscillator [28, 29] is a simple self-sustained oscillator and is a popular choice of model to study synchronisation [30, 31]. It has the equation of motion

$$\ddot{x} - \gamma_1 \dot{x}(1 - \gamma_2 x^2) + \omega_0^2 x = 0, \tag{2.1.1}$$

where γ_1 and γ_2 are the rates which control the two necessary components for a self-sustained oscillator: negative and non-linear damping. We can work in dimensionless time so that the oscillator frequency $\omega_0 = 1$. Changing variables, we rewrite the equation of motion in terms of a complex amplitude α, so that

$$\frac{\alpha + \alpha^*}{2} = x, \qquad i\frac{\alpha^* - \alpha}{2} = \dot{x}.$$

Making the assumptions that $\gamma_1, \gamma_2 \ll 1$ we can make a rotating wave approximation and find the approximate equation of motion for the vdP takes the form

$$\dot{\alpha} = -i\alpha + \tilde{\gamma}_1 \alpha(1 - \tilde{\gamma}_2 |\alpha|^2), \tag{2.1.2}$$

where $\tilde{\gamma} = \gamma/\omega_0$. The quantity α can be written in terms of an amplitude and phase related by $\alpha = Ae^{i\varphi}$. Using this definition we can find the equa-

tions of motion for A and φ

$$\dot{A} = \frac{1}{2A}(\alpha\dot{\alpha}^* + \dot{\alpha}\alpha^*), \tag{2.1.3}$$

$$\dot{\varphi} = \frac{1}{2iA^2}(\alpha\dot{\alpha}^* - \dot{\alpha}\alpha^*). \tag{2.1.4}$$

Setting the time derivative of A to zero and finding the stable steady-state solution results in $A = 1/\sqrt{\tilde{\gamma}_2}$, which in turn gives $\dot{\varphi} = 1$. However, since we are working in dimensionless units this result means the phase is going round periodically with frequency ω_0. As the equation of motion for φ has no fixed points the behaviour at long time depends on the initial conditions, indicating no phase preference.

The simplicity of the vdP model has recently made it an attractive system for studying synchronisation near the quantum limit [32]; work has been done for single driven vdP oscillators [25, 27], two coupled oscillators [26, 33–36], and many globally coupled oscillators [25], looking at both quantum regimes and how these cross over into semiclassicality.

To model the vdP oscillator in the quantum regime we can base it on a quantum harmonic oscillator that interacts with an environment in ways that lead to negative and non-linear damping [25]. The master equation of the system in the interaction picture is

$$\begin{aligned}\dot{\rho} =& \kappa_1(2a^\dagger\rho a - aa^\dagger\rho - \rho aa^\dagger) \\ &+\kappa_2(2a^2\rho a^{\dagger 2} - a^{\dagger 2}a^2\rho - \rho a^{\dagger 2}a^2),\end{aligned} \tag{2.1.5}$$

where a and $a^\dagger$ are the annihilation and creation operators for the quantum harmonic oscillator. It is possible to perform a semiclassical analysis and introduce $\langle a\rangle = e^{i\varphi}$. Using the identity $\langle\dot{a}\rangle = \mathrm{Tr}[a\dot{\rho}]$ and performing a semiclassical approximation by neglecting higher order terms that arise from fluctuations, we find that the equation for motion for $\dot{\alpha} = \langle\dot{a}\rangle$ has the same form as Eq. 2.1.2, the classical system. The two sets of dissipation terms in Eq. 2.1.5 (κ_1 quantifying the negative damping, κ_2 the non-linear damping) are analogous to the classical damping terms governed by γ_1 and γ_2. Here, they represent the gain and loss of photons in the quantum system. When the number of photons $n = \langle a^\dagger a\rangle$ is very large, the dynamics of the quantum vdP oscillator is expected to approach its classical analogue with $n \simeq |\alpha^2|$, but the classical model does not account for any form of noise.

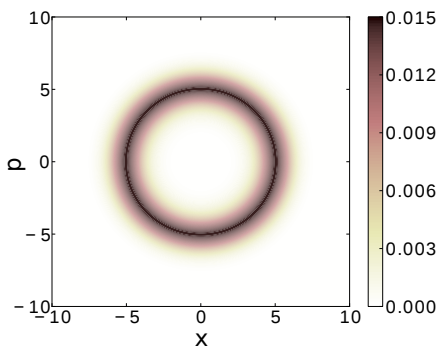


Figure 2.2: The Wigner distribution[1] of a van der Pol oscillator, calculated using the steady state of Eq. 2.1.5 with $\kappa_2/\kappa_1 = 0.04$. The ring shape shows a clearly defined limit cycle, and the even distribution around the ring shows that there is no phase preference.

The density operator obtained from the master equation contains all the information available about the system, from which we can extract properties that could indicate synchronisation. One particularly useful quantity is the Wigner function [37, 38], a quasi-probability distribution that maps out the density matrix onto phase space coordinates, defined by

$$W(x,p) = \frac{1}{\pi}\int \mathrm{e}^{-2ipy}\langle x-y|\rho|x+y\rangle \mathrm{d}y, \tag{2.1.6}$$

where x and y are position coordinates and p is a momentum coordinate [39]. As a quasi-probability distribution it can have properties that would be forbidden in classical distributions such as points where it goes negative, and this can be used as an indicator of quantum behaviour.

As the Wigner function is a phase space representation it can act as a visualisation of the vdP oscillator limit cycle, shown in Fig. 2.2, where it can be seen that there is no phase preference in the steady state. However, despite being a quantum system the quantum vdP oscillator never exhibits a negative Wigner function, or any other features that would be indicative of strongly quantum properties such as number squeezing.

2.2 The Micromaser

The micromaser is a system that is considerably more complex than the van der Pol oscillator, and retains many characteristics that make it a good choice for studying quantum synchronisation. It can form sharp limit cycles

[1] All Wigner distributions in this thesis are created using QuTiP for Python [40, 41] for which the units of x and p are scaled by $1/\sqrt{2}$ and $\hbar = 1$.

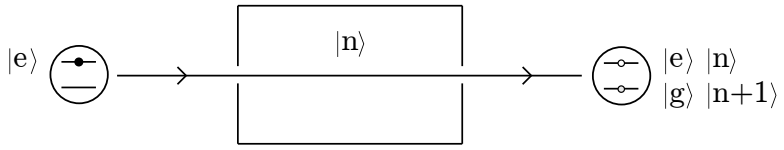


Figure 2.3: The passage of an atom excited to a Rydberg state $|e\rangle$ through a microwave cavity containing n photons. The atom undergoes Rabi oscillations and emerges in either the excited state or the ground state $|g\rangle$ depending on the time it has spent travelling through the cavity.

but also display strongly quantum characteristics, contrary to the van der Pol oscillator.

The micromaser comprises a stream of excited Rydberg atoms travelling through a high quality cavity in a Poissonian distribution, and interacting with one of the cavity modes at a microwave frequency [42, 43] (see Fig. 2.3). The atoms can be treated as two-level systems with one ground state and one excited state, with the other states being far off-resonance with small chance of interacting with the cavity. We can consider the cavity mode to be a quantum harmonic oscillator, which has non-linear and negative damping due to the interactions with the incoming flow of atoms and the environment. The long lifetimes of the photons (due to the high Q-factor of the cavity and being operated at very low temperatures to minimise thermal noise) and Rydberg atoms mean that a stream of individual atoms can effectively pump the cavity mode to reach the threshold of stimulated emission, even if we consider the case where only one atom (or fewer) is in the cavity at any time; it is this one-atom case which characterises the micromaser.

The Jaynes-Cummings model describes the interaction between the cavity mode and the atoms [44, 45]. It is possible to simplify the model by considering the cavity alone, for which a master equation can be derived by tracing out the atoms [43, 46, 47]. The resulting master equation in the interaction picture takes the form

$$\dot{\rho} = \sum_{\mu=1}^{4} \left(L_\mu \rho L_\mu^\dagger - \frac{1}{2}\{L_\mu^\dagger L_\mu, \rho\} \right), \tag{2.2.1}$$

where L_μ are Lindblad operators representing the dissipation terms in the

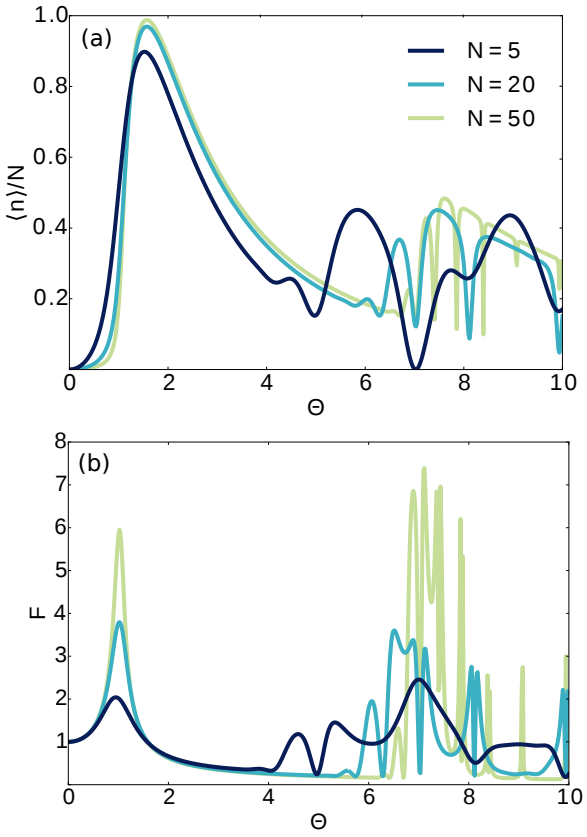


Figure 2.4: (a) Average photon occupation number $\langle n \rangle$ and (b) Fano factor F as a function of the pump parameter $\Theta = \phi N^{1/2}$ and N in the steady state.

master equation, and are given by

$$L_1 = \sqrt{N}\, a^\dagger \frac{\sin\left(\phi\sqrt{aa^\dagger}\right)}{\sqrt{aa^\dagger}}, \tag{2.2.2}$$

$$L_2 = \sqrt{N}\, \cos\left(\phi\sqrt{aa^\dagger}\right), \tag{2.2.3}$$

$$L_3 = \sqrt{\nu+1}\, a, \tag{2.2.4}$$

$$L_4 = \sqrt{\nu}\, a^\dagger, \tag{2.2.5}$$

where units are chosen such that the cavity decay rate $\gamma = 1$. Here, N is the atom beam rate in units of the rate of photon number decay and ϕ is the Rabi frequency multiplied by the time spent in the cavity by the atom, or the "accumulated Rabi angle" [47]. The average number of thermal photons is given by ν and in the interest of protecting the most interesting quantum behaviour in the system from being diminished or destroyed we will assume zero temperature, $\nu = 0$.

There are many convincing reasons for using the micromaser as a model system for quantum synchronisation. Firstly and essentially, it is a self-sustained oscillator that can form good, clear limit cycles. As we will mostly be considering the dynamics in the steady state, another advantage for the micromaser is the fact that an exact analytical solution exists, given by the number distribution [46]

$$\rho_{\text{s.s.}}(n) = \rho_{\text{s.s.}}(0) \prod_{m=1}^{n} \left(N \frac{\sin^2\left(\phi\sqrt{m}\right)}{m} \right), \tag{2.2.6}$$

where $\rho_{\text{s.s.}}(0)$ arises from the normalisation of $\rho_{\text{s.s.}}(n)$. For systems more complex than a single undriven micromaser solutions need to be calculated numerically, but Eq. 2.2.6 provides a useful starting point for approximate analytical solutions for these systems.

In the steady state, the micromaser (as with all lasers) has a threshold related to the pump rate of the atoms at $\Theta = \phi N^{1/2} = 1$ that marks a transition from spontaneous to stimulated emission of photons [46]. Figure 2.4 uses the average number of photons $\langle n \rangle$ and Fano factor $F = (\langle n^2 \rangle - \langle n \rangle^2)/\langle n \rangle$ to show the complex dependence of the system on the parameters N and Θ. The Fano factor quantifies the variance in n as a ratio of its mean $\langle n \rangle$; a value of $F = 1$ means that the distribution is Poissonian, and a sub-Poissonian value $F < 1$ is indicative of a non-classical number-squeezed state [39]. Figure 2.4 shows that the behaviour as a function of Θ is quite complex. We can see clearly the masing threshold at $\Theta = 1$, where $\langle n \rangle$ rises sharply. After this there are regions of bistability, squeezed number states, and trapping states. The characteristics and locations in Θ of these various dynamical states depend on N. Also, N correlates strongly with how many photons there are in the cavity, so low N corresponds to systems with more quantum behaviour whereas large N systems can be seen as approaching a more semiclassical regime.

Below the threshold at $\Theta = 1$, the cavity mode state fluctuates about the origin in phase space, and due to the fact there is no limit cycle it is not expected to synchronise. Figure 2.5 displays examples of Wigner functions of a micromaser below and above the threshold. Above the masing threshold, the cavity mode exists in various forms of limit cycle states. As we can see from Fig. 2.4, the locations of different dynamical states in Θ depend on the value of N.

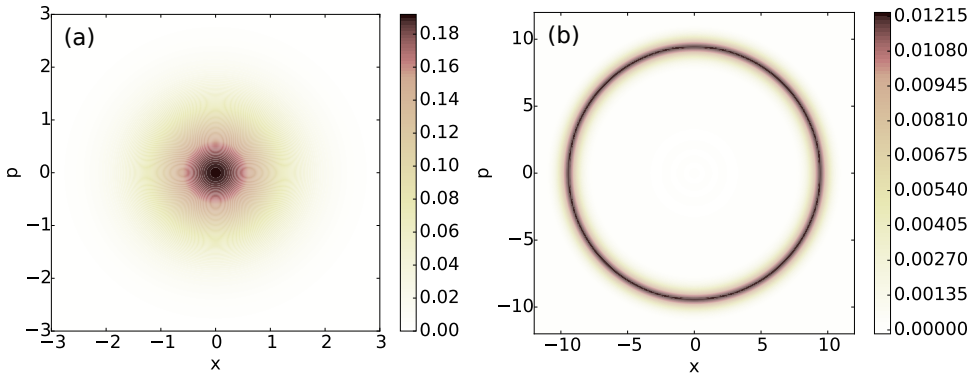


Figure 2.5: The Wigner distribution of a micromaser at $N = 50$ (a) before ($\Theta = 0.5$) and (b) after ($\Theta = 2$) the masing threshold. Limit cycle states only exist in the micromaser above the threshold.

At zero temperature where there are no thermal fluctuations, there are parameters for which the photon number is trapped below a certain value [48, 49]. Using the exact solution of the micromaser steady state Eq. 2.2.6 we can see that this happens at $\sin(\phi\sqrt{n+1}) = 0$ with $n = 0, 1, 2\ldots$, which is related to both N and Θ. Trapping states are a consequence of the rate of atoms being precisely such that the Rabi cycle completes in the same time for each atom, removing the mechanism by which more photons can enter the cavity. As Fig. 2.4 shows, for $N = 5$ the system can even be trapped in the ground state. Trapping states create sharp transitions that are easily destroyed with thermal photons [Fig. 2.6 (a) and (b)] and are interesting to look at due to the fact that they are purely the product of quantum processes and create very strongly non-classical states.

Bistable regions are also interesting dynamical states that exist in the micromaser, where the photon probability distribution is split between two distinct areas [Fig. 2.6 (c) and (d)]. The stability of trapping states and bistabilities in the presence of a drive or other micromasers is something that will be explored in later chapters.

There has also been much work on the power spectrum of the micromaser [50–52] from which we can extract information on the frequencies in the system through time correlations, a common way of looking at the properties of laser systems. The general definition of the power spectrum for an

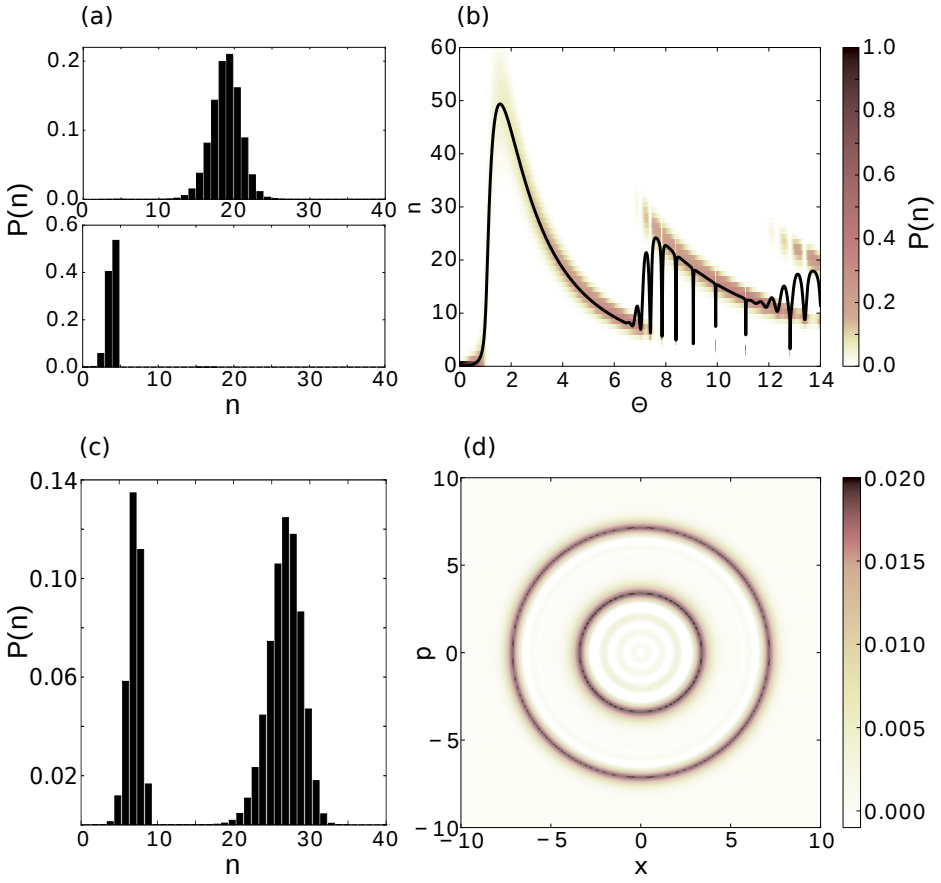


Figure 2.6: Examples of some interesting states the micromaser can produce. (a) Probability distributions $P(n) = \langle n|\rho|n\rangle$ for the micromaser at a trapping state location, $\Theta = 9.069$. The top distribution has the number of thermal photons set to $\nu = 0.4$, whereas the lower distribution is at zero temperature ($\nu = 0$). (b) $P(n)$ is shown for a wider range of Θ for $\nu = 0$, and $\langle n\rangle$ (solid black line) is overlaid showing sharp transitions in photon numbers where there are trapping states. (c) $P(n)$ at $\Theta = 7.467$, the location of a bistable state. (d) The same bistable state shown as a Wigner distribution. $N = 50$ for all plots.

electric field $E(t)$ is [53]

$$S(\omega) = \frac{1}{\pi}\mathrm{Re}\int_0^\infty \mathrm{d}\tau\, \mathrm{e}^{i\omega\tau}\langle E(t)E^*(t+\tau)\rangle. \tag{2.2.7}$$

The power spectrum for lasers typically takes the form of a Lorentzian distribution [50], and the linewidth is the full width at half-maximum (FWHM, or less frequently the full width at full-maximum) – a parameter that can give us much useful information about the system.

The finite laser linewidth can be understood in a phenomenological way using the phase diffusion model [53]. We can write the electric field as a complex quantity $E = A\mathrm{e}^{i\varphi(t)}$ with a fixed amplitude A and time dependent phase φ. The evolution of the phase is modelled as a random walk, which leads to a diffusion of phase probability over time that obeys the diffusion equation

$$\frac{\partial P}{\partial t} = D\frac{\partial^2 P}{\partial \varphi^2}, \tag{2.2.8}$$

with a phase diffusion constant D. It can be shown that this phase diffusion constant is the same quantity as the FWHM of the power spectrum, and hence describes the laser linewidth [54–56]. This description is useful when there is difficulty in calculating two-time correlation functions, and can work well even for the micromaser [53] despite being a semiclassical description.

As well as being able to produce a wide variety of dynamical limit cycle states, the micromaser can create some strongly quantum states with very low photon numbers and number-squeezed states [57–59], indicated by a sub-Poissonian Fano factor, and sometimes also by a strongly negative Wigner function (shown in Fig. 2.7). These properties make it an interesting model system for studying synchronisation in the quantum regime.

2.3 Realising Quantum Self-Sustained Oscillators

Due to its highly quantum and non-linear features, there has been quite a lot of theoretical work done on the micromaser [47, 60], including micromasers coupled to an external drive [61], and micromasers coupled to each other [62–64]. Many micromaser theories have already been experimentally confirmed [65], despite the difficult experimental set-up. To observe truly

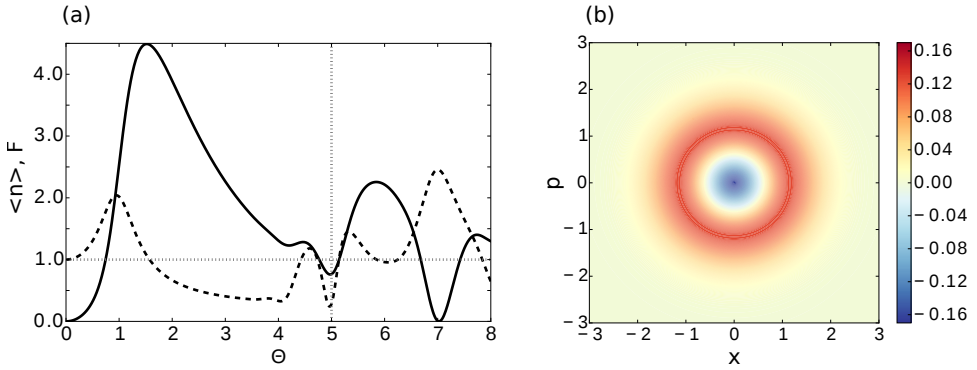


Figure 2.7: Capturing the quantum behaviour of the system, at $N = 5$. (a) The average number of photons $\langle n \rangle$ (solid) and the Fano factor, F (dashed). A Fano factor below one describes a sub-Poissonian photon distribution, which combined with the very low photon number is a good indication of a strongly quantum state. (b) A Wigner function for the micromaser that has large negative regions, something not possible with classical distributions, is another quantum indicator. Here $N = 5$, $\Theta = 4.97$.

quantum effects very low temperatures are required, the Rydberg atoms need to have very long lifetimes, the cavity must have a very high Q-factor, and the chances of multiple atoms in the cavity must be reduced to be extremely small. This section discusses alternative ways to study micromaser-like physics that are more flexible experimentally and could have wide applications. There is also some brief discussion of other types of quantum self-sustained oscillator systems that have been proposed for studying synchronisation.

2.3.1 Circuit Quantum Electrodynamics

Though it exhibits quite complex behaviour, the micromaser essentially amounts to two key components: a two-level system coupled to an oscillator. There are many different ways to build this type of system in cavity quantum electrodynamics (QED) [66], circuit QED [67–69], and optomechanical realisations [70].

Circuit QED opens up a wide range of possibilities for studying cavity QED by using superconducting circuit components to form systems that are analogous to light-matter interactions [71–74]. In the form of a circuit, the

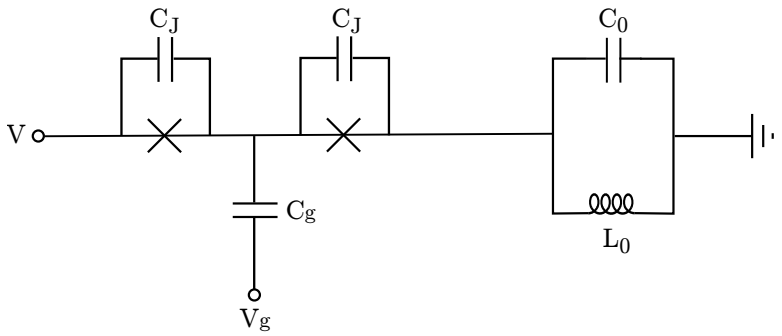


Figure 2.8: A circuit diagram of a micromaser-like setup [68, 69]. Two Josephson junctions (with capacitances C_J) are connected to a gate voltage V_g to make a Cooper-pair transistor which can be tuned to have two prominent energy levels, chosen to resonate with the oscillator mode. The oscillator consists of an inductor L_0 and capacitor C_0, which is excited by a flow of charges when a voltage V is applied across the circuit.

systems become customisable and highly tunable in comparison to atom-photon experiments.

In superconducting circuits, stripline resonators act like optical cavities in the microwave frequency range [75], with each mode acting as a quantum harmonic oscillator. Other more complex resonators can also be used such as SQUIDs [76]. Artificial atoms in a superconducting circuit require that the energy levels are not evenly spaced, and can be made a number of different ways by exploiting the non-linear properties of Josephson junctions [77–79]. These devices have the advantage of having extremely large dipole moments whilst still being able to behave quantum mechanically. For the purpose of studying the micromaser, artificial atoms require an energy level spectrum with two levels that are distinct and able to resonate with the chosen oscillator mode. These two-level systems are often called qubits, in reference to their potential application in quantum computing.

Many superconducting circuit micromaser analogues have been proposed [67, 68]. An example of a superconducting circuit set-up analogous to the micromaser is illustrated in Fig. 2.8. To the right, an inductor and capacitor are connected in parallel to form a simple harmonic oscillator. To the left, two Josephson junctions (JJs) are connected via a gate voltage V_g and gate capacitor with C_g to form a Cooper pair transistor (CPT), a popular choice for an artificial atom [69]. JJs consist of an insulating layer of material be-

tween two superconducting layers, and a current is created by Cooper pairs tunnelling coherently through the insulating layer. This gap creates an additional capacitance, C_J, associated with the JJ. The gate voltage and capacitance can be tuned to adjust the properties of the circuit to create a system where finite numbers of Cooper pairs can be found in the island between the JJs. At very low temperatures this can be simplified to a two-level system where the "ground" state $|0\rangle$ is represented by no additional Cooper pairs on the island, and the "excited" state $|1\rangle$ is represented by one additional Cooper pair. The size, shape and material of the circuit components, together with the temperature of the system and bias voltage/current tuning, creates a highly customisable arrangement that can achieve regimes currently unattainable for cavity QED systems [69, 80].

Synchronisation in superconducting circuits has recently begun to be explored theoretically [81]. In an era where quantum mechanical effects are being proposed to expand information processing, encryption and more [6, 75, 82], the applications of understanding how micro- and mesoscopic circuit components interact with each other are clear. Noise and decoherence are great challenges in this field, so understanding, for instance, the relationship between noise and synchronisation in circuit QED can bring us closer to controlling these effects.

2.3.2 Optomechanical and Spin Systems

Synchronisation has also begun to be explored in other types of quantum self-oscillating systems. Optomechanical systems contain an optical mode that is coupled to some type of micro- or nanomechanical device. By tuning the frequency of the laser light, anti-damping effects can be achieved and together with the required non-linearity in the system this enables limit cycles to be formed [83]. Due to the small scale of these systems a quantum regime is possible to achieve [84], and experimentally there are many different options for forming optomechanical arrays. One example that has been experimentally realised is optomechanical crystals [85, 86], devices that take advantage of structural periodicity to allow interacting photonic and phononic modes, which have been shown theoretically to display synchronisation [87].

Various driven two-level systems have also been investigated from the per-

spective of quantum synchronisation [88]. Synchronisation has been studied theoretically in ensembles of driven two-level atoms coupled to a cavity mode [89, 90], where quantum phase transitions were found to occur. A mean-field approach to studying an ensemble of quantum dipoles has also been undertaken, and compared with quantum correlations and entanglement as indicators of synchronisation [18]. Systems of trapped ions, driven and damped with lasers, have also been suggested as candidates for studying quantum synchronisation [19, 25].

Chapter 3

Synchronisation

Having now introduced the systems that will be considered in this thesis, this chapter presents the key concept that will be studied in these systems: synchronisation. Initially, there is a brief summary of classical synchronisation, including behaviour in noisy systems. Then we progress to quantum synchronisation, with a discussion of how this has already been studied and the differences that have been found compared with classical analogues. Finally, various suggestions of how to define and quantify quantum synchronisation are examined.

3.1 Classical Synchronisation

A self-sustained oscillator has no phase preference and the frequency is entirely determined by its intrinsic properties. When it is coupled to one or more other oscillators – or a weak external drive – the interaction between the oscillators can induce a change in their phase and frequencies; this is known as synchronisation. Phase and frequency locking occur in a perfect noiseless system when all oscillators in the system fully synchronise. Otherwise partial synchronisation occurs, indicated by an emerging phase preference and frequency entrainment towards (but not locked onto) a common value. Synchronisation arises through complex mutual influence of the oscillators on each other, or through a drive, and some prerequisites are that the coupling must be weak, and initial conditions (such as detuning) similar amongst the oscillators. Figure 3.1 illustrates frequency locking as a

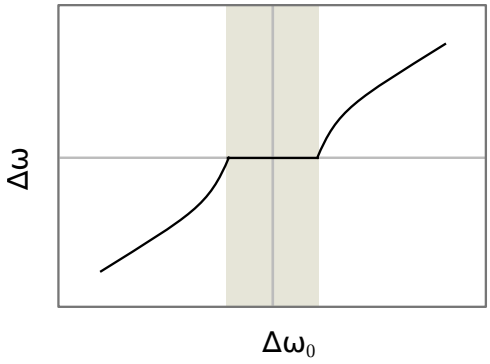


Figure 3.1: Frequency locking, where the difference in oscillator frequencies $\Delta\omega$ reaches zero (shaded), occurs over a limited range of initial detuning $\Delta\omega_0$. The size of this range is determined by the coupling strength.

function of the initial detuning of the oscillators.

There are several different types of synchronisation that can occur. A single self-sustained oscillator can synchronise with an external driving oscillation. The phase is highly sensitive to perturbations whereas the amplitude is not, so synchronisation takes place even for very weak couplings where the amplitude is minimally affected. This is particularly important in the case of a driven oscillator, as eventually an external source of energy will dominate the system when the coupling is strong enough. For this system, synchronisation can be identified by the locking of the oscillator phase to that of the drive, or the oscillator frequency deviating from its intrinsic value. In the case of phase locking, any phase preference that emerges is an indication of synchronisation (as the undriven oscillator has no preference), and this can be measured in a number of different ways that depend on the system.

We can also consider systems of several self-sustained oscillators that mutually synchronise. For two oscillators, we will introduce two quantities in order to identify phase locking: the total phase $\varphi_+ = \varphi_1 + \varphi_2$ and relative phase $\varphi_- = \varphi_1 - \varphi_2$. When two self-sustained oscillators are coupled, synchronisation typically appears as the emergence of a preference for one or more values of the relative phase [2]. In this case there is no external drive in the system so the amplitudes of the oscillator limit cycles are more constrained, however weak coupling is still of most interest.

For many coupled oscillator systems the Kuramoto model is a well-known description [91, 92], which relates the phases φ and frequencies ω of the

oscillators (for which the values are given by a chosen distribution) by

$$\dot{\varphi}_i = \omega_i + \sum_{j=1}^{M} K_{ij} \sin(\varphi_j - \varphi_i) \tag{3.1.1}$$

for each oscillator $i = 1, \ldots, M$ and where K_{ij} is the coupling matrix. A mean-field approximation is often used [92–94] to describe systems where there is a very large number of oscillators all coupled to each other, so that the coupling effect on one oscillator can be described by an average of its neighbours. In this case Eq. 3.1.1 then becomes

$$\dot{\varphi}_i = \omega_i + Kr \sin(\psi - \varphi_i), \tag{3.1.2}$$

where ψ is the average phase and r is the order parameter

$$re^{i\psi} = \frac{1}{M} \sum_{i=1}^{M} e^{i\varphi_i} \tag{3.1.3}$$

In the steady state the order parameter r is greater than zero when the system is synchronised and it goes to zero when it is not. As $K \to \infty$, $r \to 1$ i.e. all oscillators are completely synchronised. For the mean-field model, $0 > r > 1$ indicates synchronisation for a subset of the oscillators in the system, i.e. partial synchronisation. Coupled oscillators in these networks become synchronised via a phase transition when a critical coupling value is achieved. However, finite size effects and noise induced fluctuations can add complexity to the model and affect this transition [94].

For all types of self-oscillator systems, synchronisation is a phenomenon that arises from the complex interactions that occur due to feedback in nonlinear systems – the appearance of frequency and phase locking alone is not sufficient to say that something is synchronised. If for example an oscillator is linear, or if an external drive has an amplitude much larger than the oscillator, then the mechanisms by which the frequency and phase are being influenced do not fall under the "mutual influence" definition of synchronisation [2].

Even for oscillators with these prerequisites, synchronisation is not guaranteed to occur. If the difference in frequencies between the oscillators (detuning) is too high and the coupling strength not sufficiently strong then frequency entrainment will not occur (as seen in Fig. 3.1). The relationship between coupling strength, frequency and synchronisation often takes a form known as Arnold tongues [95], examples of which are shown in Fig. 3.2.

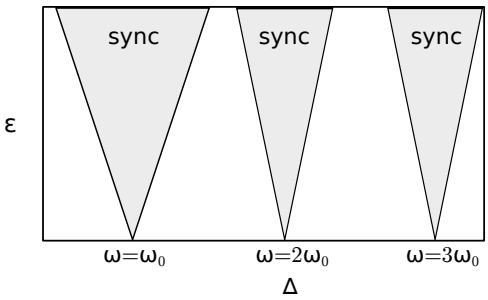


Figure 3.2: Schematic representation of regions where synchronisation can occur as a function of the coupling between two oscillators, ε and their initial frequency difference $\Delta = \omega_0 - \omega$. The synchronised regions take the form of Arnold tongues [2]. Usually the largest tongue is located at $\Delta = 0$.

3.1.1 Noise

In perfect noiseless systems, synchronisation leads to phase and frequency locking. However, interaction with an environment also gives rise to noise so that partial synchronisation is seen – in the form of either an emerging phase preference or frequency entrainment, where a common value is preferred but no locking occurs [96]. Noise has the effect of softening the transition between synchronised and unsynchronised regimes, but can also prevent synchronisation from occurring altogether or even enhance [97] or induce [21, 22] it in chaotic systems. The phase in particular is very sensitive to any changes in the system, so fluctuations due to noise in an isolated self-sustained oscillator cause the phase to do a "random walk" [98], a process known as phase diffusion. In systems where a phase preference exists, noise causes fluctuations around a preferred value and can also give rise to phase slips [99–101], where the phase of an oscillator jumps 2π in either direction (the direction of the phase slip and how often they occur is governed by the detuning).

Noise can be modelled by finding the equation of motion for the amplitude or phase, and adding a small fluctuation term to create a Langevin equation. The corresponding Fokker-Planck equation can then be solved. When considering a weakly driven classical self-sustained oscillator with noise, Stratonovich [98] showed that if the amplitudes of the fluctuations are not too strong in comparison to the amplitude of the limit cycle then non-linearities in the Fokker-Planck equation may be neglected, meaning that the amplitude distribution is close to Gaussian.

The amplitude of the limit cycle may be robust to fluctuations, but the phase

is highly sensitive to them. Stratonovich found that the phase probability distribution is given by the Fokker-Planck equation

$$\frac{\partial P(\varphi)}{\partial t} = -\frac{\partial}{\partial \varphi}\left[A_\varphi P(\varphi)\right] + D\frac{\partial^2 P(\varphi)}{\partial \varphi^2}, \tag{3.1.4}$$

where the first term describes the phase drift A_φ, which is dependent on the properties of the system and absent for an undriven oscillator, and the second term describes the diffusion (as in Eq. 2.2.8) with D the diffusion constant (independent of φ). We are interested in the steady state where $\dot{P}(\varphi) = 0$, and have two conditions: that the solution is periodic, i.e. $P(\varphi + 2\pi) = P(\varphi)$, and that it is normalised, so that $\int_0^{2\pi} P(\varphi)\,\mathrm{d}\varphi = 1$. We can then solve the Fokker-Planck equation to yield the phase probability distribution, which is in general non-Gaussian due to the non-linear nature of the self-sustained oscillators.

Classical, and semiclassical systems such as lasers, are well described by the Fokker-Planck model [102]. This description relies on the assumption that the source of noise is small relative to the average amplitude of the oscillations. For classical systems the most common source of noise is thermal, which for the most part can be controlled as required. In the quantum limit, where amplitudes are small and quantum fluctuations are present, this model can break down and other descriptions may be required [103].

The next section discusses the differences between classical and quantum synchronisation. The quantisation of the field means that many of the quantities used for identifying classical synchronisation must be adjusted for quantum systems. Additionally, quantum correlations and information-based quantities can be considered as gauges of synchronisation.

3.2 Quantum Synchronisation

Even at zero temperature, quantum systems contain an unavoidable source of noise in the form of zero-point fluctuations. Some direct comparisons between quantum and classical models have been studied using the van der Pol oscillator [20, 25] and have found that quantum noise does affect the nature of synchronisation. For a driven self-sustained oscillator, a classical case of frequency locking would show a delta peak at the drive frequency, but in the quantum case this is spread out in a broader spectrum [20]. The

transition from an unlocked to locked regime as a function of detuning is sharp for the classical system, but smoothed out in the quantum limit. A more detailed comparison between a quantum mechanical model and a closely related semiclassical model (with noise) suggested that synchronisation could be more robust in the quantum case. For example, in the case of many coupled oscillators treated with a mean-field model [25] where a transition to a synchronised regime occurs at a critical value of coupling, this occurred at consistently lower coupling values for the quantum model than the semiclassical one, with the effect strongest in the quantum limit with small limit cycles.

For quantum systems the usual measures of synchronisation may have to be adjusted, and entirely new measures may be considered. The next section covers some of the key quantities that have been used in measuring quantum synchronisation, and discusses the systems for which they are most appropriate.

3.2.1 Measures of Synchronisation in Quantum Systems

The frequency of a quantised electromagnetic field can be found by taking the Fourier transform of the two-time correlation function of a cavity mode, resulting in the quantum power spectrum [20, 104] (the quantum equivalent of Eq. 2.2.7)

$$S(\omega) = \int_{-\infty}^{\infty} \mathrm{d}t\, \mathrm{e}^{i\omega t} \langle a^\dagger(t) a(0) \rangle. \tag{3.2.1}$$

Finding the peak of this spectrum gives us the average frequency of the cavity mode, which during frequency entrainment will be a value pulled away from its natural frequency. Even with no thermal noise, the distribution will be broadened by quantum fluctuations.

There are a number of ways in which the emergence of a phase preference can be measured in a quantum system. One already discussed is the Wigner function, a representation of the system in phase space. A simpler way to view phase information is to use the parameter $\alpha \equiv \langle a \rangle = A\mathrm{e}^{i\varphi}$. Lee and Sadeghpour [25] use $|\langle a \rangle|$ as an order parameter for the phase synchronisation of many vdP oscillators, the quantum equivalent of r (Eq. 3.1.3). This is a useful parameter for the system, as it goes to zero in the steady state when the oscillators are not synchronised. However, it is less helpful in the

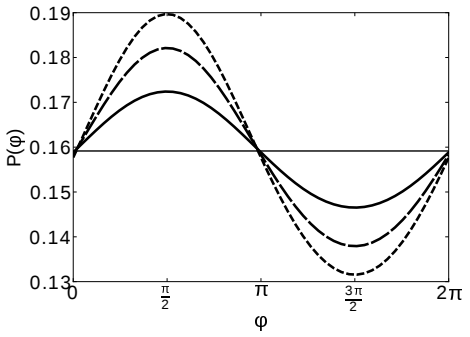


Figure 3.3: An illustrative example of the phase distribution $P(\varphi)$ plotted for a driven micromaser. For zero drive the function is flat at $1/2\pi$. For the driven case, the function is sinusoidal and 2π-periodic; the stronger the drive, the higher the peak of $P(\varphi)$.

case of a system developing a preference for more than one phase value.

A method that targets phase more directly is to extract the parts of the density matrix that contain phase information to give the phase probability density function, given by [39]

$$P(\varphi) = \frac{1}{2\pi}\langle\varphi|\rho|\varphi\rangle = \frac{1}{2\pi}\sum_{n=0}^{\infty}\sum_{n'=0}^{\infty}\rho_{nn'}\,\exp\left[\mathrm{i}(n'-n)\varphi\right]. \tag{3.2.2}$$

The phase operator here is an eigenstate of the Susskind-Glogower phase operator $\sum_{n=0}^{\infty}|n\rangle\langle n+1|$, and is defined by $|\varphi\rangle = \sum_{n=0}^{\infty}\mathrm{e}^{in\varphi}|n\rangle$. This phase probability distribution also arises from the Pegg-Barnett formalism [105]. Figure 3.3 depicts this distribution for a driven micromaser. For a system with no phase preference, the phase probability density is constant at a value of $1/2\pi$. To obtain a more concise measure of synchronisation, we can use [19]

$$R = 2\pi\max[P(\varphi)] - 1, \tag{3.2.3}$$

which takes the peak of the phase probability density function and scales it so that $R = 0$ when there is no phase synchronisation. Equation 3.2.2 yields the phase information for one oscillator – for two coupled oscillators, the *relative* phase probability distribution can be used [19, 106, 107]

$$\begin{aligned} P(\varphi_-) \;=\; & \frac{1}{2\pi}\sum_{n,m=0}^{\infty}\sum_{k=\max(n,m)}^{\infty}\mathrm{e}^{i\varphi_-(m-n)} \\ & \times\langle n, k-n|\rho|m, k-m\rangle, \end{aligned} \tag{3.2.4}$$

for the relative phase $\varphi_- = \varphi_A - \varphi_B$ of two subsystems A and B.

As well as trying to directly measure the frequency and phase of the oscillators, there have also been efforts to use broader criteria to identify synchro-

nisation. In quantum systems there are various information-based measures that have been proposed [108].

Simply looking at correlations between variables can give us useful information on what is happening in a system. Such correlations can be described by quantities that are as simple as $\langle A\rangle\langle B\rangle/\langle AB\rangle$ or more sophisticated measures such as the Pearson factor [109]. Several different types of correlations between variables such as quantum discord [114] and internal degrees of freedom [19] have been used for quantum systems.

Entanglement, a truly quantum phenomenon, has also been explored in conjunction with synchronisation in quantum systems [15, 16, 25]. Entanglement for a bipartite system can be quantified using the logarithmic negativity [111]

$$E_N(\rho) = \log_2[2N(\rho) + 1], \tag{3.2.5}$$

where the negativity is $N(\rho) = \frac{1}{2}\sum_i (|\lambda_i| - \lambda_i)$, with λ_i the eigenvalues of ρ^{T_A}, the partial transpose of the density operator of the total system. Lee et al. [26] present an "entanglement tongue", the equivalent of an Arnold tongue, as evidence of entanglement coexisting with synchronisation in the system. Arnold tongues show that coupled oscillators synchronise above a certain critical value of coupling, and that this critical value increases as detuning increases, as shown in Fig. 3.2. This relationship is replicated for entanglement in the case of two dissipatively coupled van der Pol oscillators in a strongly quantum regime where the average occupation number is very low.

Entropy is also proposed as another information-based measure, frequently in the form of mutual information. Mutual information for a bipartite system composed of subsystems A and B is defined as [112]

$$I(\rho) = S(\rho_A) + S(\rho_B) - S(\rho_{AB}), \tag{3.2.6}$$

where $S(\rho) = -\mathrm{Tr}(\rho\log\rho)$ is the von Neumann entropy. A classical version of mutual information has been used as a signature of synchronisation for chaotic systems [113]. More recently Ref. [34] uses mutual information as an order parameter to identify synchronisation in a system of classical and quantum coupled van der Pol oscillators, and also in a system of coupled qubits and oscillators. However, in other systems [110] mutual information is less successful as a measure of synchronisation.

Recently, new quantities have been proposed for describing quantum synchronisation in continuous variable systems [15]. Defining canonical variables $p_1(t)$ and $q_1(t)$ for subsystem S_1, and similar for subsystem S_2, the differences of these variables $p_-(t) = (1/\sqrt{2})[p_1(t) - p_2(t)]$ (and $q_-(t) = (1/\sqrt{2})[q_1(t) - q_2(t)]$) should vanish at large t if the subsystems achieve complete synchronisation i.e. all trajectories of the subsystems are identical. Phase synchronisation occurs when only the phases are locked, with the individual phases defined by $\varphi_j(t) = \arctan[p_j(t)/q_j(t)]$. However, as these are quantum mechanical canonical operators they must obey the uncertainty principle, which constrains the system so that it can never reach complete synchronisation as it could in a classical description. Two synchronisation measures are suggested [15]:

$$\mathcal{S}_c(t) = \langle q_-(t)^2 + p_-(t)^2 \rangle^{-1} \tag{3.2.7}$$

$$\mathcal{S}_p(t) = \frac{1}{2}\langle p'_-(t)^2 \rangle^{-1}, \tag{3.2.8}$$

where the second specifically describes phase synchronisation by introducing the notation $a_j(t) = (1/\sqrt{2})[q_j(t) + ip_j(t)] = [r_j(t) + a'_j(t)]e^{i\varphi_j(t)}$ and $\langle a_j(t) \rangle = r_j(t)e^{i\varphi_j(t)}$. The Hermitian and anti-Hermitian parts of $a'_j(t) = [q'_j(t) + ip'_j(t)]/\sqrt{2}$ are interpreted as the fluctuations in the amplitude and phase, and this leads us to look at fluctuations in $p'(t) = [p'_1(t) - p'_2(t)]/\sqrt{2}$ as a measure of phase synchronisation. Interestingly, even with the maximal synchronisation allowed by these measures, the subsystems do not necessarily have to be entangled [15].

There have been many different recent proposals to define and measure synchronisation for quantum systems. However, it is as yet unclear which methods are preferable for identifying quantum synchronisation and how they might vary from system to system. In this thesis we investigate some of these measures, along with semiclassical methods, focussing on phase synchronisation in a range of different systems.

Chapter 4

A Driven Micromaser

In this chapter we consider the steady state of a single micromaser that is coupled to an external drive. As seen in Sec. 2.2 the micromaser can produce many dynamical states, including trapping states that are strongly quantum in nature. Two key parameters that describe the behaviour of the micromaser are N and Θ, related by the Rabi angle $\phi = \Theta/N^{1/2}$. By controlling these parameters we can change the locations and characteristics of the various limit cycle states, and to some extent also control the classicality of the system. This chapter will look at a range of N, Θ and the coupling strength of the external drive ε, to see how synchronisation can be affected by the many diverse states the micromaser exhibits.

The majority of this chapter will focus on phase synchronisation in the resonant regime where the drive frequency and the frequency of the cavity mode are equal (Sec. 4.1), but we also look at some off-resonant behaviour (Sec. 4.2). Section 4.1.1 begins by looking at how adding an external drive to a micromaser affects its properties, and in Sec. 4.1.2 the question of how a phase preference can be identified is addressed. Then in Sec. 4.1.3 various phase preference quantities are compared for the system. The linewidth, a concept introduced in Sec. 2.2, is described in more detail for the micromaser in Sec. 4.1.4. Sections 4.1.5 and 4.1.6 provide semiclassical and perturbation theory descriptions respectively, as analytical approximations for the system. These are then compared to solutions found numerically in Sec. 4.1.7. There is then an expansion into the off-resonance regime, where frequency entrainment (Sec. 4.2.1) and phase synchronisation (Sec. 4.2.3)

are looked at with non-zero detuning, the former by utilising the quantum power spectrum. The semiclassical approximation is developed to account for non-zero detuning in Sec. 4.2.2, and is qualitatively compared to numerical results. Finally, some conclusions are discussed in Sec. 4.3.

4.1 On-resonance

Equation 2.2.1 gives the master equation for an undriven micromaser in the interaction picture. Adding a coherently coupled drive ε, and moving to a rotating frame at the drive frequency ω_{d}, the Hamiltonian becomes

$$H = \hbar\varepsilon(a^\dagger + a) + \hbar\Delta a^\dagger a, \tag{4.1.1}$$

where $\Delta = \omega_0 - \omega_{\mathrm{d}}$ is the detuning between the micromaser and the external drive, and from this point on we will work in units such that $\hbar = 1$. In this section we will consider the on-resonance case where $\Delta = 0$, before generalising to non-zero detuning in Sec. 4.2. With no difference in the oscillator and drive frequencies, the focus in this section is on how a weak coupling to the drive causes a phase preference to emerge for the micromaser.

4.1.1 Properties of a driven micromaser

Although a single undriven micromaser has an exact analytical solution, adding any other complexity to the system means that it will have to be solved numerically (or analytically using approximations). For most numerical results in this thesis we make use of QuTiP [40, 41], a quantum optics toolbox written for Python. As with all numerical approximations the state space must be truncated, so care is taken throughout to include a sufficient number of states to accurately represent the behaviour of the system.

Before considering the synchronisation of the micromaser, we will first look in general terms at the effect of a drive on the steady state of the micromaser. When adding an external drive to the system, we must make sure that it does not affect the energy of the system too strongly. Eventually, the external drive will be able to "force" an oscillator to its frequency and phase

if it is a dominating source of energy in the system. We are interested in the weak coupling regime, where there is little change to the energetics whilst still allowing the potential for strong phase changes.

Figures 4.1 and 4.2 show how the amplitude of the limit cycle changes with ε. Figure 4.1 shows the limit cycles in the form of Wigner distributions for four values of Θ, both undriven and with drive strengths $\varepsilon = 0.01$, 0.1 allowing a comparison between weak and stronger drive strengths. These values of Θ are chosen to represent different dynamical states of the micromaser for $N = 50$. (a) $\Theta = 1.040$ is just above the threshold, and therefore has a poorly defined limit cycle. (b) $\Theta = 4.756$ has a large, well-defined limit cycle, but has the same average number of photons $\langle n \rangle$ as $\Theta = 1.040$ when the micromaser is undriven. (c) $\Theta = 7.467$ is a bistable state, with two clear limit cycles. Finally, (d) $\Theta = 9.069$ is located in the middle of a trapping state, and therefore has a limit cycle with a much smaller amplitude.

When comparing the undriven system with the driven ones, Fig. 4.1 (a) shows a state that is very sensitive to the drive and shows a strong phase preference at $\varepsilon = 0.1$. The state is not altered significantly except for exhibiting phase locking even from a very weak drive. This is not true for (b), which shows that the state for $\Theta = 4.756$ is mostly unchanged when a small drive is added, and the phase preference that emerges is visible for only the larger drive with a higher peak at the bottom of the limit cycle. There is still a small phase preference at $\varepsilon = 0.01$ but this is not easily discerned by simply looking at the Wigner function. The bistable state in (c) at $\Theta = 7.467$ is largely unaffected by the weaker drive. However, the stronger drive almost completely destroys the bistability to favour the larger state, which has a mostly unaltered amplitude. The trapping state in (d) is especially sensitive to the drive, and makes a jump to a state with a much larger amplitude as the drive strength increases. For most of the four Θ values, it is clear that a drive strength of $\varepsilon = 0.1$ is strong enough to dramatically change the entire state, rather than the phase alone.

Figure 4.2 looks at the effect of the drive from another perspective, using $\langle n \rangle$ and F (scaled by their undriven values $\langle n \rangle_0$ and F_0). We look at these properties as a function of ε for the same four values of Θ. We see in Fig. 4.2 that while $\Theta = 4.756$ is quite resistant to the effects of a drive in terms of

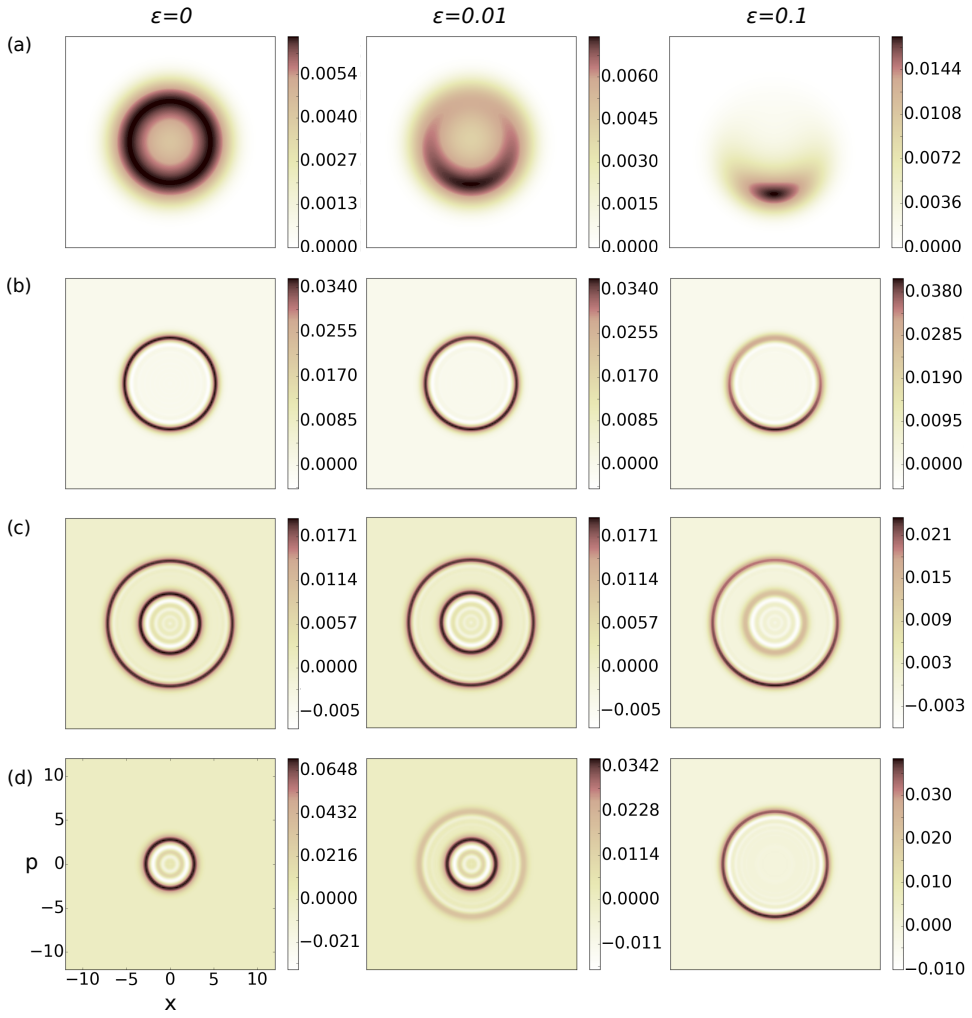


Figure 4.1: Wigner distributions of an undriven micromaser (left) and driven micromasers at $\varepsilon = 0.01$ (middle) and $\varepsilon = 0.1$ (right), all at $N = 50$, for (a) $\Theta = 1.040$, (b) $\Theta = 4.756$, (c) $\Theta = 7.467$ and (d) $\Theta = 9.069$. The axes are the same for each distribution.

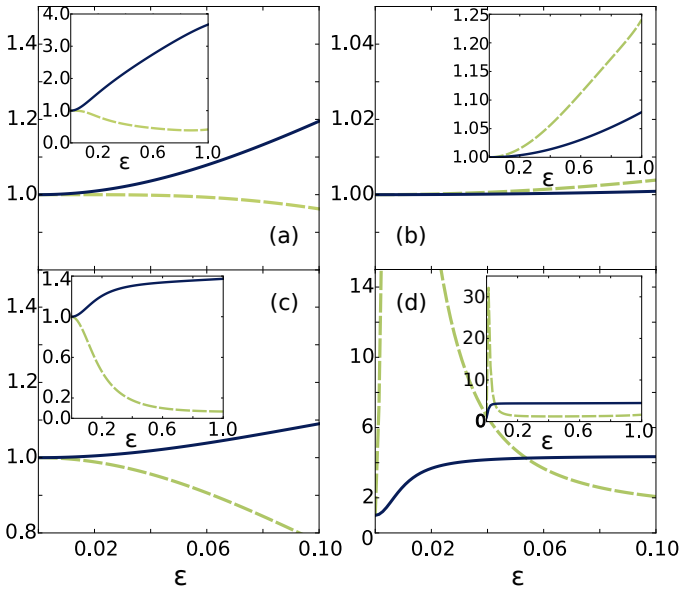


Figure 4.2: Average photon occupation number $\langle n \rangle / \langle n \rangle_0$ (solid line) and Fano factor F/F_0 (dashed line) as a function of the coupling strength ε at $N = 50$, for (a) $\Theta = 1.040$, (b) $\Theta = 4.756$, (c) $\Theta = 7.467$ and (d) $\Theta = 9.069$. The same measures are inset for a larger range of ε.

photon numbers the other chosen values of Θ are more sensitive, in agreement with Fig. 4.1. In particular, the trapping state is highly sensitive to even a very small drive. The state closest to the threshold, $\Theta = 1.040$, appears to behave similarly to the bistable state in Fig. 4.2 for low ε. In Fig. 4.1 however, it is clear that these two states are completely different, and that $\Theta = 1.040$ is more sensitive to a weak drive than $\Theta = 7.467$. Despite the Wigner function containing more information about a state, it is difficult to identify a phase preference visually when it is small. The next section introduces more quantitative ways to distinguish changes in the phase.

4.1.2 Predicting the phase preference

We can predict the phase preference for the on-resonance driven micromaser by considering the quantity

$$\langle a \rangle = \alpha = A e^{-i\varphi}. \tag{4.1.2}$$

We know that a stable phase preference emerges when the system is in the steady state, so we can find the fixed points of the equation of motion in α

to find this phase preference.

There is no phase preference for the undriven system – the dissipation terms in the master equation do not contain any phase information. We will only need to consider the coherent terms, which produces the equation of motion

$$\dot{\alpha} = \mathrm{Tr}[a\dot{\rho}] = -i\mathrm{Tr}\left[a[H,\rho]\right], \tag{4.1.3}$$

where H is given in Eq. 4.1.1. Using the cyclic property of the trace, we obtain

$$\dot{\alpha} = -i\varepsilon. \tag{4.1.4}$$

Using Eq. 4.1.2 we then find the equation of motion for the phase, φ, to be

$$\dot{\varphi} = \frac{\varepsilon}{A}\cos\varphi. \tag{4.1.5}$$

We are interested in the steady-state case. We can see that $\dot{\varphi} = 0$ when $\varphi = \pi/2$ or $\varphi = 3\pi/2$, so to find out which of these fixed points is stable we can add a perturbation

$$\delta\dot{\varphi} = \frac{\varepsilon}{A}\cos(\varphi_0 + \delta\varphi). \tag{4.1.6}$$

At the fixed points $\cos\varphi_0 = 0$, and

$$\delta\dot{\varphi} = -\frac{\varepsilon}{A}\sin\delta\varphi \qquad \text{at} \quad \varphi = \pi/2, \tag{4.1.7}$$

$$\delta\dot{\varphi} = \quad \frac{\varepsilon}{A}\sin\delta\varphi \qquad \text{at} \quad \varphi = 3\pi/2. \tag{4.1.8}$$

We can see that the perturbation of $\dot{\varphi}$ decays at $\pi/2$ and grows at $3\pi/2$. Therefore, $\varphi = \pi/2$ is the stable fixed point, which is seen in Fig. 4.1.

4.1.3 Measures of the phase preference

We can measure the magnitude of this phase preference by using the quantity $|\langle a\rangle|/\langle n\rangle^{1/2}$. Figure 4.3 (a) shows this measure of phase as a function of the coupling strength for the four previously seen values of Θ. We can directly compare this quantity to the maximum amplitude of the phase probability density function of the system, R (Eq. 3.2.3), shown in Fig. 4.3 (b).

At first glance, these two measures appear to be similar. However, the two measures of phase behave differently as a function of ε over this range. The value of Θ for which the phase preference grows most quickly is the

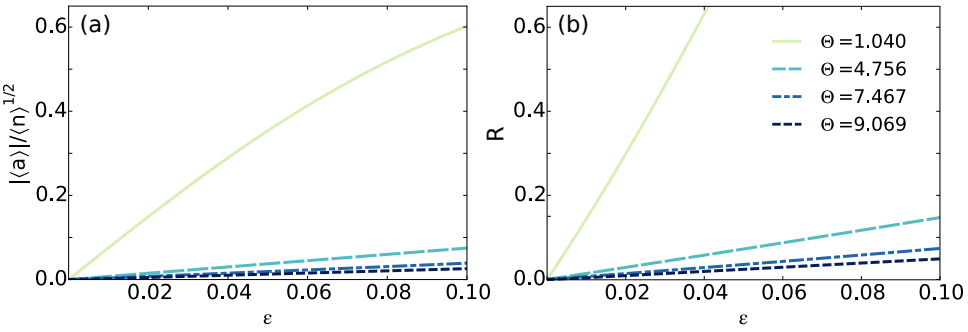


Figure 4.3: Measuring phase synchronisation in the form of (a) $|\langle a\rangle|/\langle n\rangle^{1/2}$ (b) R, both as a function of coupling strength ε for four different values of Θ at $N = 50$.

near-threshold Θ, a behaviour that is seen in both quantities. The largest difference between the measures is seen for this Θ value, where R grows much more quickly than $|\langle a\rangle|/\langle n\rangle^{1/2}$. At weak coupling they both appear linear, but $|\langle a\rangle|/\langle n\rangle^{1/2}$ loses this linearity before R does. The other three Θ values are qualitatively very similar for both measures, but again R grows with ε more quickly than $|\langle a\rangle|/\langle n\rangle^{1/2}$.

For all three of our phase measures – the Wigner distribution, $|\langle a\rangle|/\langle n\rangle^{1/2}$, and R – there is no phase preference measured in the undriven system, whereas one emerges in all three measures for even a very weak drive. Hereafter, we shall use R as the primary measure of a phase preference in the system.

4.1.4 The micromaser linewidth

As we've seen in Sec. 3.1.1, for lasers the evolution of the phase is often described as a random walk that can be modelled as a diffusion process [98]. A fuller description of the time-dependent phase distribution can be found in a Fokker-Planck equation, Eq. 3.1.4, which also includes phase drift. While some form of phase diffusion always exists (as it describes the system noise) A_φ arises only when the system is driven and a non-zero value indicates a phase preference. For lasers, D is also the linewidth of the laser – the full width at half maximum (FWHM) of its frequency spectrum [53]. The linewidth gives enough information for lasers to be described well by

Fokker-Planck equations [102, 115, 116] – even in the presence of quantum noise – as they are semiclassical systems and the large number of photons allows the dynamics to be described well with this single parameter. It would be interesting to see how well the linewidth could do at describing similar systems in the quantum limit. The micromaser not only has noise in the form of quantum fluctuations, but much more complex quantum behaviour that is not seen for ordinary lasers.

The linewidth of the micromaser is obtained from the FWHM of its spectrum, given in Eq. 3.2.1. Since the master equation for the micromaser is Markovian (the evolution of the state is independent of any past states) the quantum regression theorem [104] can be applied, which means the two-time correlation function $\langle a^\dagger(t)a(0)\rangle$ evolves in the same way as $\langle a^\dagger(t)\rangle$. This was used by Scully et al. [53] to derive an approximate expression for the micromaser linewidth, which turns out to be similar description to that of an ordinary laser, where [53]

$$\langle a^\dagger(t)a(0)\rangle = \mathrm{e}^{-D|t|/2}\langle n\rangle, \tag{4.1.9}$$

with D as the phase diffusion constant. This simple form for the correlation function leads to the spectrum

$$S(\omega) = \frac{\langle n\rangle D}{\frac{D^2}{4}+\omega^2}, \tag{4.1.10}$$

a Lorentzian distribution with a FWHM of D.

Following the approach of Scully et al. [54], we can rewrite the master equation for the micromaser in the form

$$\dot{\rho}_n^{(k)} = -\frac{1}{2}\mu_n(k)\rho_n^{(k)} + c_{n-1}\rho_{n-1}^{(k)} - d_n\rho_n^{(k)} - c_n\rho_n^{(k)} + d_{n+1}\rho_{n+1}^{(k)} \tag{4.1.11}$$

where $\rho_n^{(k)} \equiv \rho_{n,n+k} \equiv \langle n|\rho|n+k\rangle$, and

$$\frac{\mu_n(k)}{2} = 2N\sin^2\left[\frac{\phi}{2}\left(\sqrt{n+1+k}-\sqrt{n+1}\right)\right] + \left(n+\frac{k}{2}-\sqrt{n(n+k)}\right), \tag{4.1.12}$$

$$c_{n-1}(k) = N\sin(\phi\sqrt{n})\sin(\phi\sqrt{n+k}), \tag{4.1.13}$$

$$d_n(k) = \sqrt{n(n+k)}. \tag{4.1.14}$$

We make an assumption that the evolution of the density matrix meets certain detailed balance conditions to reach the steady state, and also that the

elements of the density operator evolve according to the ansatz

$$\rho_n^{(k)}(t) = \mathrm{e}^{-D_n(t)}\rho_n^{(k)}(0), \tag{4.1.15}$$

where $D_n(t)$ is a function whose form can be derived self-consistently. Using this, we can obtain an approximate semiclassical expression for the linewidth

$$\begin{aligned}\bar{D} &= \mu_{\langle n\rangle}(k=1)\\ &= 4N\sin^2\left[\frac{\phi}{2}\left(\sqrt{\langle n\rangle+2}-\sqrt{\langle n\rangle+1}\right)\right]\\ &+2\left[\left(\langle n\rangle+\frac{1}{2}\right)-\sqrt{\langle n\rangle(\langle n\rangle+1)}\right].\end{aligned} \tag{4.1.16}$$

This is a semiclassical approximation, indicated by the bar $\bar{}$, where a single narrow peak in the number distribution is assumed so that all instances of n have been replaced with $\langle n\rangle$. (A more detailed explanation of how to arrive at this expression can be found in Appendix A.1.) Equation 4.1.16 is the full expression for $\bar{D}$, but we can make further approximations to simplify it. Assuming $\langle n\rangle \gg 1$, we have

$$\sqrt{\langle n\rangle+2}-\sqrt{\langle n\rangle+1} \approx \frac{1}{2\sqrt{\langle n\rangle}} \tag{4.1.17}$$

and also,

$$\langle n\rangle+\frac{1}{2}-\sqrt{\langle n\rangle\left[\langle n\rangle+1\right]} \approx \frac{1}{2}\frac{1}{4\langle n\rangle}. \tag{4.1.18}$$

Hence our final expression, valid for large $\langle n\rangle$, is

$$\bar{D} = 4N\sin^2\left(\frac{\phi}{4\sqrt{\langle n\rangle}}\right)+\frac{1}{4\langle n\rangle}. \tag{4.1.19}$$

We now have three linewidth quantities to compare for the micromaser: the FWHM of the numerically calculated spectrum, a semiclassical approximation Eq. 4.1.16, and a large-$\langle n\rangle$ approximation Eq. 4.1.19. Figure 4.4 compares these quantities over a range of Θ values at (a) $N = 5$ and (b) $N = 50$.

In the quantum regime $N = 5$, the approximations do well for low Θ but quickly lose their accuracy as Θ increases. Closer towards the semiclassical limit at $N = 50$ the approximations do much better, as expected. When the number of photons $\langle n\rangle$ is at its peak, for $1 \lesssim \Theta \lesssim 3$, the approximations do very well. At $N = 50$, photon numbers are much higher for all values of Θ

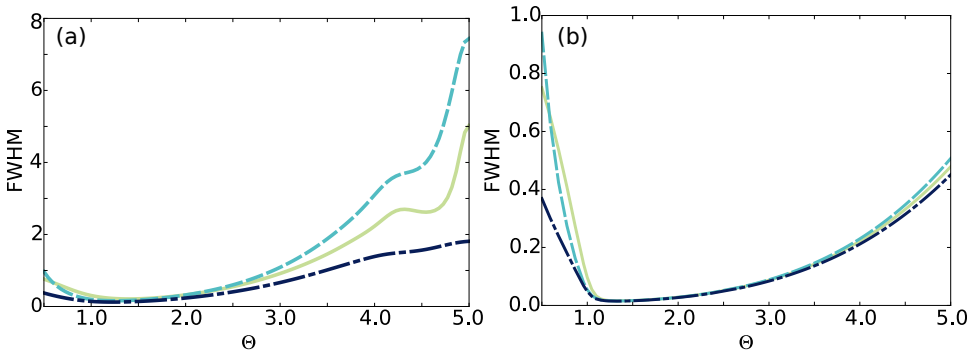


Figure 4.4: The FWHM of the spectrum $S(\omega)$ as a function of Θ for (a) $N = 5$, (b) $N = 50$. The numerical calculation (solid line) is compared with the semiclassical approximation (Eq. 4.1.16, dashed line) and large-$\langle n \rangle$ approximation (Eq. 4.1.19, dot-dashed line).

than for $N = 5$ and both approximations continue to be reasonably accurate at larger Θ values[1]. Although the semiclassical and large-$\langle n \rangle$ approximations tend to overestimate or underestimate the FWHM respectively, they do so by similar amounts suggesting that when the system is in a regime considered semiclassical enough for the semiclassical approximation to be accurate, $\langle n \rangle$ will already be large enough for the large-$\langle n \rangle$ assumption to also be valid. In Fig. 4.4 (b), all calculations of the FWHM make a sharp transition at $\Theta = 1$ indicating the masing threshold. For Fig. 4.4 (a) this is smeared out so much that a clear location of the threshold is not easily identified. Below the $\Theta = 1$ threshold, a limit cycle no longer exists for the micromaser at any N. The linewidth for all lasers becomes much larger below the threshold, when the system is more dominated by spontaneous emission. The change in the FWHM for $\Theta < 1$ is clear, particularly for $N = 50$, and the approximations also diverge from the numerical results probably due to assumptions that are not valid in this region such as a distribution of n that is strongly peaked around a single large value.

[1]For $\Theta > 5$ the complex states of the micromaser such as bistable regions mean that the assumptions made about the number distribution break down [52, 55].

4.1.5 Semiclassical phase distribution

As we discussed in Sec. 3.1.1, for noisy classical oscillators the phase can be expected to behave in accordance with a Fokker-Planck equation Eq. 3.1.4 with a drift term (that arises from the drive) and a noise term that creates phase diffusion (with the linewidth as the diffusion constant). The average movement in φ, or drift, for the driven micromaser has already been calculated in Eq. 4.1.5, so we find that $A_\varphi = (\varepsilon/\sqrt{\langle n \rangle})\cos\varphi$. The semiclassical approximation of the linewidth found in the previous section gives us the phase diffusion constant D, yielding a Fokker-Planck equation with exactly the same form analysed by Stratonovich [98]. Following the approach in Ref. [117] we can therefore solve the Fokker-Planck equation for the steady-state phase distribution of $P(\varphi)$ with periodic boundary conditions in terms of $\bar{D}$,

$$P(\varphi) = \left[2\pi \mathrm{I}_0\left(\frac{2\varepsilon}{\sqrt{\langle n \rangle}\bar{D}}\right)\right]^{-1} \mathrm{e}^{\left(\frac{2\varepsilon}{\sqrt{\langle n \rangle}\bar{D}}\right)\sin\varphi}, \tag{4.1.20}$$

where $\mathrm{I}_0(x)$ is the first modified Bessel function. This semiclassical phase distribution can now be compared to our numerical solutions of R.

4.1.6 Perturbation theory description

One very appealing attribute of the micromaser is that it can be exactly solved for the undriven case. We are already restricting ourselves to a regime of small ε for studying synchronisation. It is therefore natural to make use of the analytic solution to create a perturbation theory where we assume ε is a small enough quantity that any terms with a higher-order dependence on ε may be neglected.

We begin with the master equation for a single undriven micromaser in the form given in Eq. 4.1.11, with $\rho_n^{(k)} \equiv \langle n|\rho|n+k\rangle$. To this we can add new terms that arise when we introduce a coherent drive ε

$$\dot{\rho}_n^{(k)}\Big|_{\text{drive}} = -i\varepsilon\left[\sqrt{n+1}\,\rho_{n+1}^{(k-1)} + \sqrt{n}\,\rho_{n-1}^{(k+1)} - \sqrt{n+k}\,\rho_n^{(k-1)} - \sqrt{n+k+1}\,\rho_n^{(k+1)}\right]. \tag{4.1.21}$$

When Eq. 4.1.21 is added to Eq. 4.1.11 we have the master equation for the driven system. The value of k characterises how "off-diagonal" the terms are, with $\rho_n^{(0)}$ describing only the diagonal terms with no ε dependence, for

which we know the exact analytical steady-state solution. These terms then generate $\rho_n^{(1)}$, the first off-diagonal terms at first-order in ε, which in turn give $\rho_n^{(2)}$ terms that are second-order in ε^2, etc. When ε is small enough we can work to first order, neglecting higher-order terms, and only consider $k = 0, \pm 1$. Full details of how these terms are calculated can be found in Appendix B.1

Once we have $\rho_n^{(1)}$ we can use it to find $P(\varphi)$. We can rewrite the phase distribution [118] to obtain $P(\varphi)$ for the driven system

$$P(\varphi) = \frac{1}{2\pi}\left(1 + 2\,\mathrm{Re}\left[\mathrm{e}^{i\varphi}\sum_{n=0}^{\infty}\rho_n^{(1)}\right]\right). \tag{4.1.22}$$

Although this solution still requires numerics, it only requires them to calculate the first-order terms for the driven system by using the exact analytical solution for the undriven one. It is therefore a much easier problem to solve in comparison to the full numerical solution and would prove extremely useful for more complex systems (for example, those with multiple oscillators). However, it is also possible to make some further assumptions to simplify the perturbation theory.

We can make the assumption that $\rho_n^{(0)}$ and $\rho_n^{(1)}$ have distributions that are strongly-peaked around $\langle n\rangle$ so that we can make the replacement $n \to \langle n\rangle$. Eventually, after some re-sums and substitutions (details in Appendix B.2) we arrive at the expression

$$P(\varphi) \simeq \frac{1}{2\pi}\left[1 - 2X\sin\varphi\right] \tag{4.1.23}$$

with

$$X = \frac{2i\varepsilon}{\mu_{\langle n\rangle}^{(1)}}\left(\rho_0^{(0)} + \sqrt{\langle n\rangle + 1} - \sqrt{\langle n\rangle}\right), \tag{4.1.24}$$

and where $\mu_{\langle n\rangle}^{(1)}$ is given by Eq. 4.1.12 with n replaced by $\langle n\rangle$. This simplified version of the perturbation theory will only work well for single-peaked, narrow distributions of n, something that will depend on both Θ and N.

4.1.7 Comparison of results

The phase distribution for the driven micromaser is illustrated in Fig. 3.3. The distribution is 2π-periodic, and the maximum in φ agrees with what

is predicted in Sec. 4.1.2. For increased coupling the size of the peak (and dip) also increases, and for the undriven system the distribution is flat with constant value $1/2\pi$. We use the quantity $R = 2\pi \max[P(\varphi)] - 1$ to determine the amount of phase synchronisation that is occurring in the system, a parameter that is scaled so that it goes to zero when the system is undriven.

There are now several expressions for R that we can compare to the numerical results obtained using the full master equation. Figure 4.5 compares them in the small-ε regime over a range of Θ.

The semiclassical approximations do better at $N = 50$ than $N = 5$ as expected as photon numbers are much larger at higher values of N. However, they are inaccurate before the threshold at $\Theta = 1$ due to the fact that they rely on the linewidth as a phase diffusion parameter, a quantity that behaves very differently below the threshold as we have seen in Fig. 4.4. The large-$\langle n \rangle$ approximation consistently underestimates the phase locking and is worse than the unsimplified semiclassical approximation, which does very well once Θ is large enough.

The perturbation theory does well for all values of Θ at low-ε, not being restricted to the above-threshold region. It works better in the more quantum regime, as it uses assumptions that we are dealing with small quantities. The perturbation theory does most poorly at $N = 50$ just above the threshold, when there are the highest numbers of photons in the cavity and a strong phase preference, as it is an approximation that assumes weak phase synchronisation. The inset figures also show that although it works well for a very weak drive it does much worse when ε is increased, particularly for $N = 50$.

The simplified perturbation theory Eq. 4.1.23 takes the middle ground between the perturbation theory and the semiclassical approximation. It works well for small-ε, and about the same as the perturbation theory for both values of N well above the threshold. At low values of N the threshold is smeared out over a greater range of Θ, so the range for which Eq. 4.1.23 works well is slightly more restricted for $N = 5$ than $N = 50$.

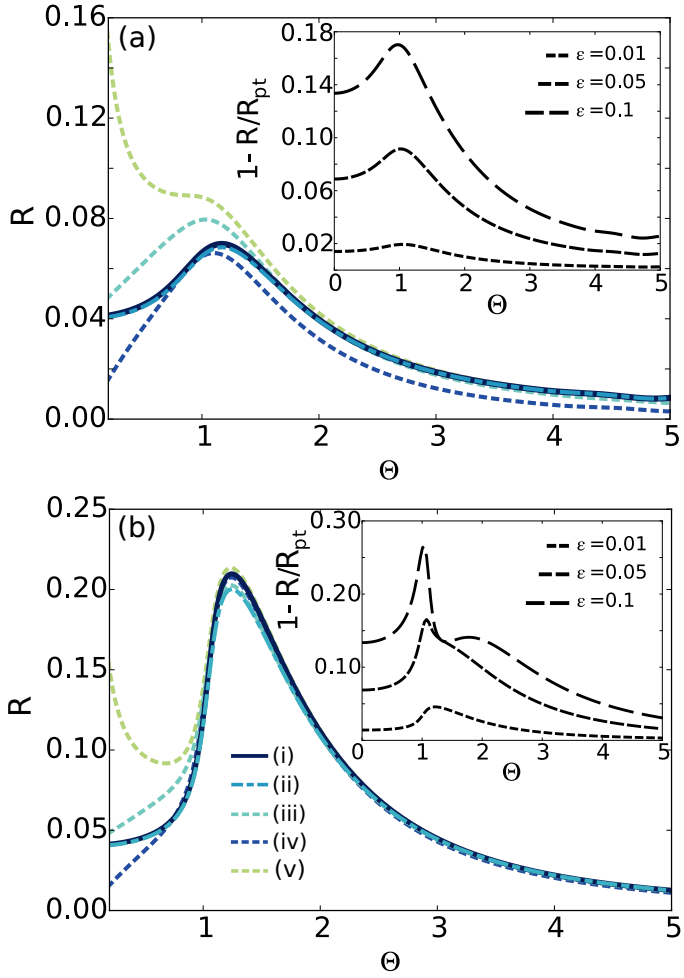


Figure 4.5: R as a function of Θ at $\varepsilon = 0.01$ for (a) $N = 5$ and (b) $N = 50$: a comparison of (i) numerical, (ii)-(iii) perturbation and (iv)-(v) semiclassical calculations. (ii) is Eq. 4.1.22, and (iii) is Eq. 4.1.23. The semiclassical calculations use Eq. 4.1.20 with $\bar{D}$ given by (iv) Eq. 4.1.19 and (v) Eq. 4.1.16. The inset figures compare the numerical (R) and perturbation (R_{pt}) calculations for different coupling strengths ε.

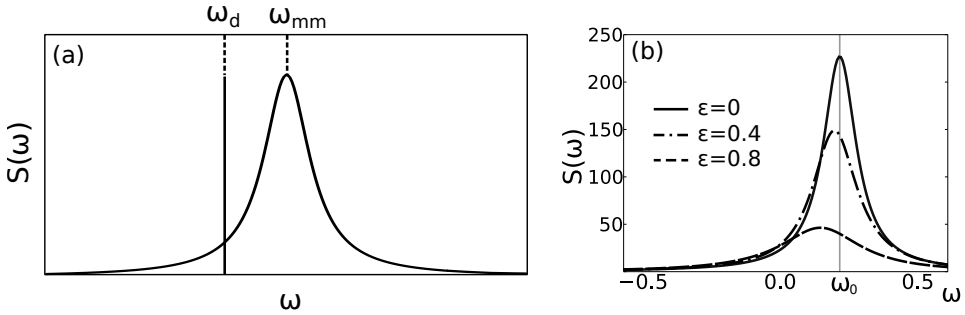


Figure 4.6: (a) A (not to scale) illustration of the expected power spectrum for the driven micromaser system. There is a delta peak at the drive frequency $\omega_{\rm d}$, but the micromaser frequency spectrum should be described by a Lorentzian function with a peak at $\omega_{\rm mm}$ due to noise arising from quantum fluctuations. (b) A numerical calculation of the micromaser spectrum with a detuning of $\Delta = 0.2$ for increasing drive strengths. The vertical line is a reference at ω_0, the natural frequency of the oscillator, while ω is the frequency with respect to the drive frequency so that $\Delta = \omega_0$. Here, $N = 10$, $\Theta = 2$ and the delta-peak has been subtracted off.

4.2 Off-resonance

4.2.1 Frequency Spectrum and Entrainment

When the drive is off-resonance it is also interesting to look at how the frequency of the micromaser is affected. The limit cycle of the micromaser will have its own intrinsic frequency, and the introduction of a drive with its own distinct frequency will draw the micromaser frequency away from its original value towards the drive frequency. In a noisy system the two frequencies will not lock to a single common value, but frequency entrainment provides important evidence of synchronisation.

To determine the frequency in the micromaser we can use the power spectrum Eq. 3.2.1, which is the Fourier transform of the two-time correlation function of the photons in the cavity, and gives the spectrum of the light. Finding the peak of the spectrum gives the micromaser frequency, $\omega_{\rm mm}$.

The expected behaviour of the frequency spectrum is shown schematically in Fig. 4.6 (a). The external drive gives rise to a delta function at $\omega_{\rm d}$. There is also a broad peak centred at frequency $\omega_{\rm mm}$ and as the drive strength is

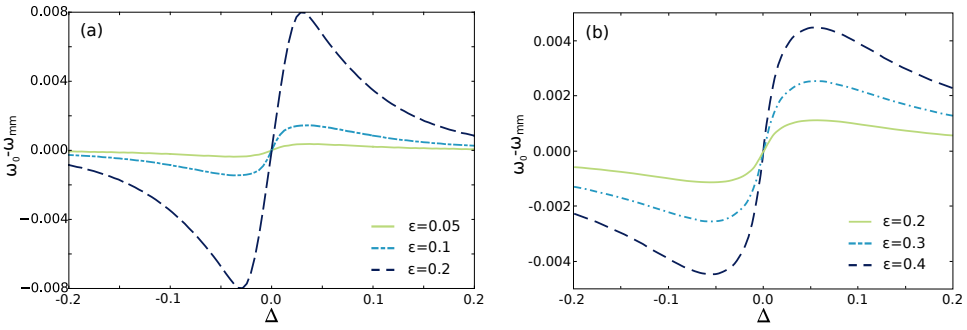


Figure 4.7: ω_{mm} as a function of detuning, Δ, at $N = 50$ for different values of ε for (a) $\Theta = 1.040$ and (b) $\Theta = 4.756$

increased, the peak at ω_{mm} is expected to be pulled towards the drive frequency. Figure 4.6 (b) gives an example of this for the micromaser, with exaggerated drive strengths and parameters chosen for illustrative purposes. Here, the spectrum is calculated by solving the two-time correlation function numerically. The calculation uses the correlation function minus the uncoupled average $\langle a \rangle \langle a^\dagger \rangle$. As it is this part that produces the drive peak, the delta function is not captured in the spectrum given in Fig. 4.6 (b) or in any other numerical spectrum calculation in this chapter. However, we can see how the behaviour of the micromaser frequency ω_{mm} responds as the drive strength is varied. The undriven micromaser has a spectrum peak indicating its initial detuning, $\Delta = \omega_0 - \omega_{\mathrm{d}} = 0.2$. As the drive strength ε is increased, the noise peak drops and is pulled towards a value of zero detuning, i.e. towards the drive frequency. The decrease in the height of the noise peak corresponds with the increase in the drive peak (i.e. increase in $\langle a \rangle$) as the system synchronises. The location of the noise peak in ω is a direct measure of frequency entrainment in the system [20].

Figure 4.7 compares the micromaser frequency of the driven micromaser ω_{mm} to the frequency of the undriven micromaser ω_0 as a function of Δ for two values of Θ. With weaker drive strengths the relative movement of the spectrum peak is extremely small, however some frequency entrainment does occur though it decays quite quickly with Δ. Close to the threshold the micromaser is much more sensitive to the strength of the drive than for $\Theta = 4.756$, as was found with phase synchronisation.

4.2.2 Semiclassical approximation of the common frequency

It is possible to calculate a semiclassical approximation for the common frequency of the system ω_c, an average that takes into account both the noise peak at ω_{mm} and the noiseless peak at the drive frequency. While this is not quantitatively comparable to ω_{mm}, the average frequency of the system will shift due to the fact that the micromaser frequency is being pulled towards towards the drive frequency, ω_d, so the two frequencies ω_{mm} and ω_c may be qualitatively compared.

In the phase diffusion picture, where we assume that the system is well-described with a Fokker-Planck equation, it is possible to find a relation between the common frequency and the average rate of change of the phase [2]

$$\omega_c = \langle \dot{\varphi} \rangle + \omega_d, \tag{4.2.1}$$

where we will use the notation $\omega_\varphi = \langle \dot{\varphi} \rangle$. We can obtain a value of ω_φ by using the Fokker-Planck equation 3.1.4, which has the same form but now with $A_\varphi = -\Delta - (\varepsilon/\sqrt{\langle n \rangle}) \cos\varphi$, obtained from the equation of motion for phase Eq. 4.1.5 (details in Appendix A.2.1). Using this we get

$$\omega_\varphi = -\Delta - \frac{2\pi\varepsilon}{\langle n \rangle} \mathrm{Re}[P_1]. \tag{4.2.2}$$

where the quantity P_1 is found through numerically solving an iterative equation to convergence.

Figure 4.8 compares the frequency entrainment of the numerically calculated micromaser frequency to the semiclassical approximation of the common frequency at (a) $N = 5$ and (b) $N = 50$ over a range of Δ. Despite being two different quantities, the qualitative behaviour is the same, as expected. The synchronisation transition is much sharper in the more classical regime and much more spread out in the quantum regime where quantum noise is more dominant in the system. Interestingly, the magnitude of frequency entrainment is almost the same for both values of N. The semiclassical approximation has a different magnitude to the numerical calculation however, despite the similar behaviour in Δ. Stronger entrainment is found for the semiclassical frequency ω_c, which is expected due to the fact that this quantity contains the delta function peak at ω_d, unlike the numerical frequency.

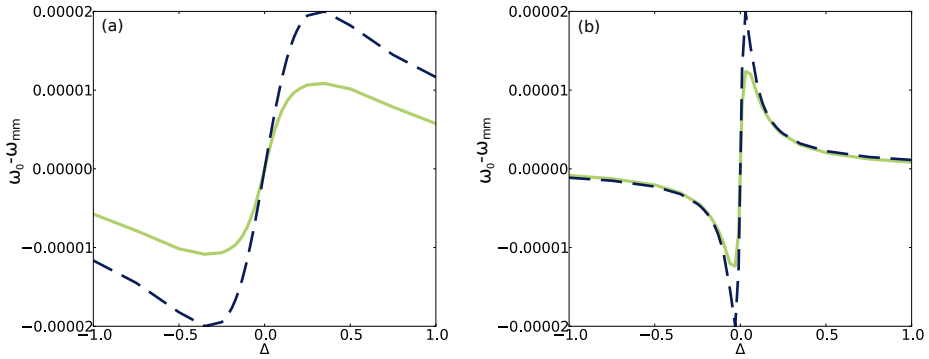


Figure 4.8: ω_{mm} as a function of detuning, Δ, at $\Theta = 2$ for (a) $N = 5$ and (b) $N = 50$. The numerical calculations (solid lines) are compared with a semiclassical approximation (dashed lines) at $\varepsilon = 0.01$.

4.2.3 Phase synchronisation

When the detuning is non-zero several attributes of the system change that affect the phase synchronisation of the driven micromaser. The main difference we would anticipate is that the phase synchronisation drops rapidly above a certain magnitude of detuning, as we have seen with frequency entrainment. This is a sharp transition for an ideal classical system, but we would expect it to be smoothed out for the micromaser due to quantum noise.

The semiclassical description of the phase distribution can be generalised for non-zero detuning. For the steady state, following Ref. [98], we get

$$\frac{d^2P}{d\varphi^2} - \frac{d}{d\varphi}\left[\tilde{D} - \tilde{D}_s\cos\varphi\right]P(\varphi) = 0, \tag{4.2.3}$$

where $\tilde{D} = -2\Delta/D$ and $\tilde{D}_s = 2\varepsilon/\sqrt{\langle n\rangle}D$. A solution to this equation is a little more involved than in the on-resonance case and is laid out in Appendix A.2.2. The generalised semiclassical phase distribution is found to be

$$P(\varphi) = \frac{1}{X}\mathrm{e}^{\tilde{D}\varphi - \tilde{D}_s\sin\varphi}\int_{\varphi}^{\varphi+2\pi}\mathrm{e}^{-\tilde{D}\psi+\tilde{D}_s\sin\psi}\,\mathrm{d}\psi, \tag{4.2.4}$$

where the factor of normalisation is

$$X = 4\pi^2\mathrm{e}^{-\pi\tilde{D}}\mathrm{I}_{-i\tilde{D}}(\tilde{D}_s)\mathrm{I}_{i\tilde{D}}(\tilde{D}_s) \tag{4.2.5}$$

and $\mathrm{I}_y(x)$ are modified Bessel functions.

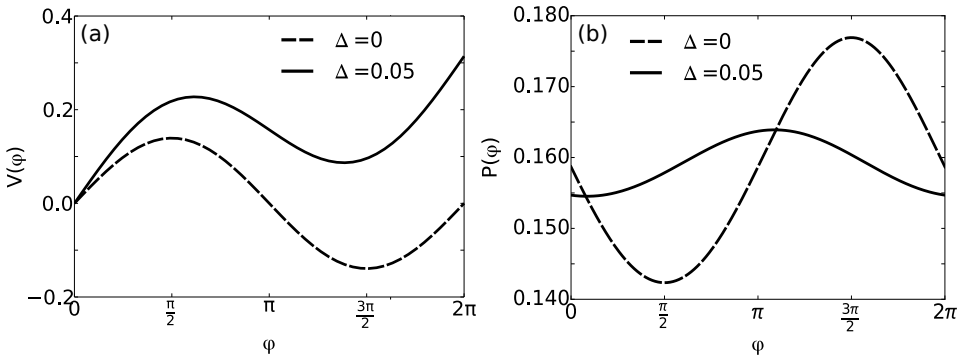


Figure 4.9: (a) The potential $V(\varphi) = \Delta\varphi + (\varepsilon/\sqrt{\langle n \rangle})\sin\varphi$ for a micromaser driven on and off-resonance, at $N = 50$, $\Theta = 2$, $\varepsilon = 1$. (b) The phase probability distribution $P(\varphi)$ on- and off-resonance, calculated at $N = 50$, $\Theta = 2$, $\varepsilon = 0.01$.

One way of visualising the effect of a non-zero detuning is by introducing the concept of a particle in a phase potential, $V(\varphi)$, whose behaviour describes the movement of the phase [96]. Integrating the drift term in the $\Delta \neq 0$ Fokker-Planck equation with respect to the phase gives us the phase potential

$$V(\varphi) = \Delta\varphi + \frac{\varepsilon}{\sqrt{\langle n \rangle}}\sin\varphi. \tag{4.2.6}$$

The shape of the phase potential, shown in Fig. 4.9 (a), has an overall gradient whose magnitude is related to the detuning. Figure 4.9 (b) shows how the phase probability distribution changes with the detuning. The location in φ of the peak of the distribution changes with Δ, and it has a much lower amplitude without changing the period of the distribution, making it appear much more spread out. At high enough Δ the distribution will become almost flat, showing very low phase synchronisation.

Figure 4.10 shows the comparison of the numerical solution and the semiclassical solution to $P(\varphi)$ over a range of Δ for three different values of drive strength. Figure 4.10 (a) looks at a near-threshold value of Θ whereas (b) has a value of Θ that has a more clearly defined limit cycle (both values of Θ have the same $\langle n \rangle$ at $\varepsilon = 0$). The inset shows the difference between the semiclassical and numerical calculations for the same parameters.

As expected, the phase density distribution is strongly peaked on-resonance and drops quickly as Δ increases. The semiclassical approximation is much

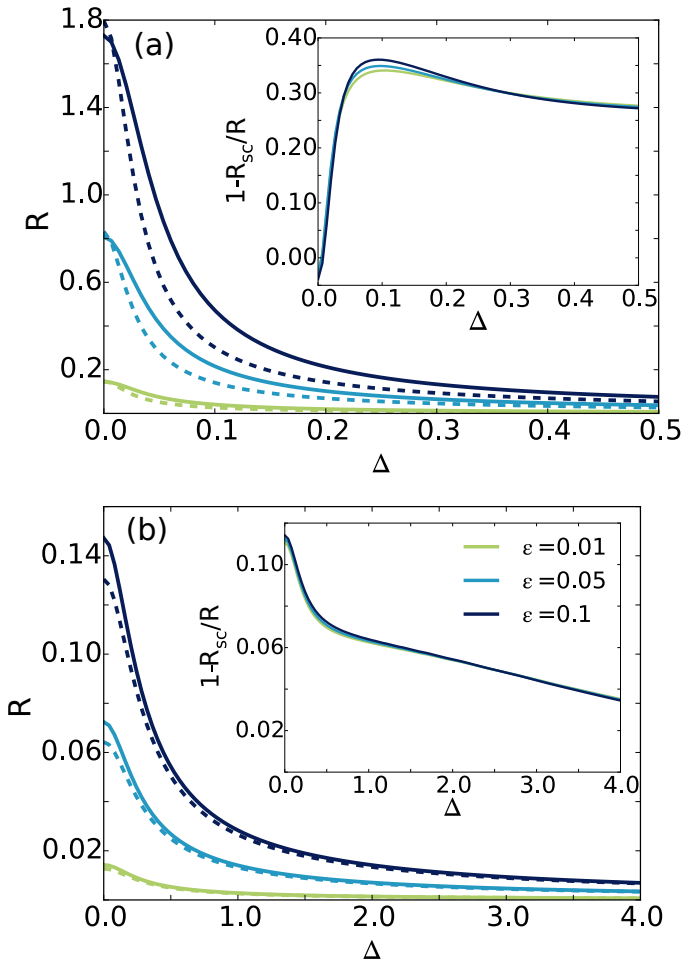


Figure 4.10: R as a function of detuning, Δ, at $N = 50$ for (a) $\Theta = 1.040$ and (b) $\Theta = 4.786$. The numerical calculations (solid lines) are compared with a semiclassical approximation (dashed lines) for different values of the coupling strength ε.

less accurate for the near-threshold regime (a) for most of the range of Δ. It overestimates the phase synchronisation near resonance, but then drops to underestimating it as Δ increases. The semiclassical description only overestimates near the threshold, as can be seen in Fig. 4.5 (b). For all values of Θ, the accuracy of the semiclassical description remains very similar regardless of the strength of the drive, ε. This makes it a better option than perturbation theory for larger drive strengths.

4.3 Summary and Conclusions

For a single micromaser, the number of atoms that travel through the cavity during its lifetime N is related to the average number of the photons in the cavity $\langle a^\dagger a \rangle = \langle n \rangle$, so when N is large so is $\langle n \rangle$ and the system behaves more classically. There are several different types of dynamical states that the micromaser can produce, and these are located at different values of Θ, the micromaser pump rate, and change depending on the value of N. The masing threshold occurs at $\Theta = 1$, below which limit cycle states for the cavity mode do not exist.

When a drive is added to the system, many dynamical states such as trapping and bistable states are destroyed. We maintained a mainly weak drive strength to focus on phase synchronisation rather than changes in the system energetics, and to preserve the dynamical states as much as possible.

We considered both the on- and off-resonance cases. On-resonance we predominantly used R, the normalised maximum of the phase probability density distribution, as a measure of phase synchronisation. We found that the behaviour of the phase preference with drive strength varies considerably depending on Θ. By using a Fokker-Planck phase diffusion model and assuming that the micromaser linewidth (the FWHM of its power spectrum) is the phase diffusion constant, semiclassical approximations of R were found. Additionally, using the fact that an undriven micromaser has an exact analytical solution, perturbation theories for the system (and therefore R) were found. The semiclassical approximations did not work well below $\Theta = 1$, as the linewidth here cannot be described simply by a phase diffusion constant, but otherwise did surprisingly well. The best agreement was obtained for large N as expected, but as long as the large photon

number assumption was not required the semiclassical approach provided reasonable estimates for $N = 5$ well above the threshold. The perturbation theories were more accurate at all values of N and Θ, but only for very weak drives ($\varepsilon \simeq 0.01$).

Going off-resonance allowed us to look at frequency entrainment using the power spectrum of the system. Finding the peak of this spectrum yields the micromaser frequency, ω_{mm}. The fact that this is a noisy system means that there is a broad noise peak in the spectrum at ω_{mm} distinct from the drive peak at ω_{d}. As the system synchronises the drive peak increases in magnitude and the noise peak decreases and shifts towards the drive frequency. A semiclassical calculation of a third frequency ω_{c} was carried out, which provides an overall average frequency of the system. Though different to ω_{mm}, they can be qualitatively compared. It was found that frequency entrainment drops off much faster for large N whereas for small N it is more spread out, despite the magnitude of the frequency entrainment being the same. The average frequency ω_{c} was also much closer to ω_{mm} in the large N system, implying that the drive peak is less significant. We were also able to look at the phase distribution for the off-resonance case, which flattens and shifts with the detuning becoming almost flat when Δ is large. The semiclassical approximation calculated previously was generalised for non-zero Δ, and it was found that as before it works well for large N and away from the threshold. It was also found that the accuracy does not decline if ε is increased, unlike in the perturbation theory.

Chapter 5

Two Coupled Micromasers

Despite sharing the umbrella term of "synchronisation", the phenomenon of an oscillator being weakly influenced by a more dominant external drive is in many ways quite distinct from two or more similar oscillators mutually influencing each other. In this chapter we explore these differences by looking at a system of two identical micromasers weakly coupled to each other in two different ways. For two oscillators, we must consider the *relative* phase distribution as a measure of phase synchronisation. In addition to the relative phase, in a two-oscillator system we now have the option of considering information-based measures such as entanglement and entropy.

Before considering synchronisation measures, in Sec. 5.1 we look at the properties of the coherent and dissipative couplings (Sec. 5.1.1), and then see how they compare to each other and to the system explored in the previous chapter in Sec. 5.1.2. In Sec. 5.2 we consider the relative phase distribution as a synchronisation measure for both systems. We then make two approximations: a semiclassical one (Sec. 5.2.1) and a perturbation theory (Sec. 5.2.2) concentrating on the simpler case of the dissipatively coupled system. A comparison of these approximations is made with the numerics in Sec. 5.2.3. Next, mutual information and then entanglement are considered for both systems in Sec. 5.3. Both these quantities behave quite differently depending on the details of the coupling in the system. Finally, Sec. 5.4 gives a summary of the findings of this chapter.

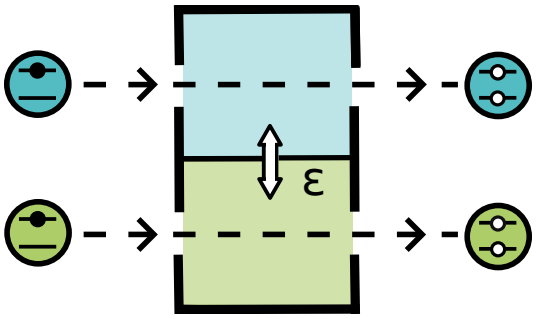


Figure 5.1: A schematic diagram of two coherently coupled micromasers. The micromasers are separately pumped and are joined by a partially reflecting mirror so that photons may tunnel between each cavity.

5.1 Properties of the systems

Current work on coupled micromasers has mostly focussed on "pump-coupled" regimes [62, 63] where two cavities are connected via the same stream of excited atoms. Here, we are interested in the interaction between the cavities of two independently pumped micromasers. We look at two specific cases: coupling via the Hamiltonian of the system (coherent coupling) or via the dissipative Lindblad operators (dissipative coupling). In this section we shall compare the properties of both systems with each other and with the case of a single driven micromaser that was explored in the previous chapter.

5.1.1 Coherent and Dissipative Couplings

We consider two identical micromasers, A and B, each with the master equation form given in Eq. 2.2.1. The master equation for the entire system is

$$\dot{\rho} = \mathcal{L}_A[\rho] + \mathcal{L}_B[\rho] + \mathcal{L}_c[\rho] \tag{5.1.1}$$

where the superoperator $\mathcal{L}_{A(B)}$ contains the Lindblad operators 2.2.2—2.2.5 for cavity A (B) and $\mathcal{L}_c$ arises from the coupling between the two cavities. To couple them, we can add a term to the coherently evolving part of the density matrix so that the Hamiltonian becomes

$$H_c = \hbar\varepsilon(a^\dagger b + b^\dagger a). \tag{5.1.2}$$

In this case the coupling term is

$$\mathcal{L}_c^{(\mathrm{coh})}[\rho] = -\frac{i}{\hbar}[H_c, \rho]. \tag{5.1.3}$$

Figure 5.1 illustrates how coherently coupled micromasers might be achieved, with photon tunnelling between the cavities [64] allowed by a partially reflective mirror.

Alternatively, we can couple the cavities via the dissipation terms. This could be achieved by introducing a third cavity into the system between the micromasers, similar to what is discussed in Ref. [33] for dissipatively coupled van der Pol oscillators, where the nature of the coupling term can be changed by adjusting the coupling of each oscillator to the third cavity.

Here, we choose dissipative coupling of the form

$$L_c = \varepsilon(a - b). \tag{5.1.4}$$

Up to this point we have been working in units where $\gamma = 1$ and $\varepsilon = \varepsilon/\gamma$. We can simplify things by adjusting this scaling and introducing

$$\tilde{\varepsilon} = \frac{\varepsilon}{\gamma + \varepsilon}, \;\; \tilde{N} = \frac{N}{\gamma + \varepsilon}, \tag{5.1.5}$$

so that we can absorb some of the coupling terms into $\mathcal{L}_A$ and $\mathcal{L}_B$ (details in Appendix C). As a result, the (rescaled) coupling terms are reduced to

$$\mathcal{L}_c^{(\mathrm{diss})}[\rho] = -\tilde{\varepsilon}\left[a\rho b^\dagger + b\rho a^\dagger - \frac{1}{2}\left\{a^\dagger b\rho + ab^\dagger\rho + \rho a^\dagger b + \rho a b^\dagger\right\}\right]. \tag{5.1.6}$$

In the next section we will look at how the effects of these two couplings, $\mathcal{L}_c^{(\mathrm{coh})}$ and $\mathcal{L}_c^{(\mathrm{diss})}$, differ from each other and from a micromaser coupled to an external drive.

5.1.2 Comparison of Couplings

We now have three systems that we can compare the properties of: the driven micromaser discussed in chapter 4, and one of the oscillators in the coherently coupled and dissipatively coupled micromaser systems. In each case we look at the steady state of the system, solved numerically. An immediate difference between the one- and two-micromaser systems is the range in N that we are able to explore. For quantum oscillators, an infinite number of states are required to describe the system, but when solving the system numerically we must use a finite number of states that is sufficiently large to describe the system accurately. For a single micromaser, the higher N is the more states M we will need; for two micromasers this scales with

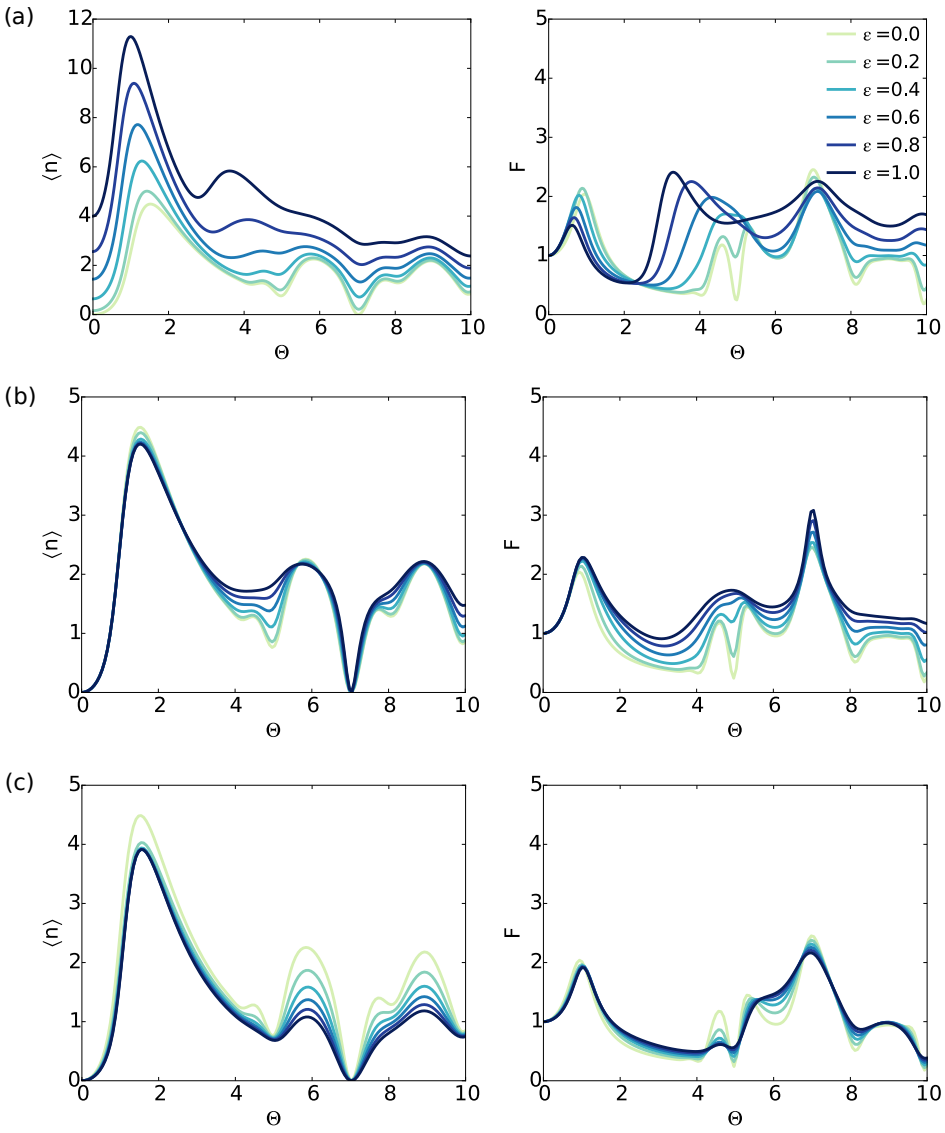


Figure 5.2: Average photon number $\langle n \rangle$ and Fano factor F as a function of Θ for increasing coupling strength at $N = 5$. (a) A single driven micromaser (b) one of two coherently coupled micromasers (c) one of two dissipatively coupled micromasers.

M^2. Limitations in computer memory meant we were restricted to $N = 5$, which means that we can only explore the more quantum regime if we use numerics.

Figures 5.2—5.4 compare different properties of the systems. Figure 5.2 looks at the average number of photons $\langle n \rangle$ and the Fano factor, F, over a range of Θ at $N = 5$. Figure 5.2 (a) is the single driven micromaser, and confirms the results found in chapter 4 that the amplitude of the limit cycle is very sensitive to the drive in almost all regions of Θ. There is a trapping state for an undriven micromaser at $\Theta \simeq 7$, where $\langle n \rangle$ is trapped in the ground state. In the case of a driven micromaser, the external energy coming into the system quickly destroys the trapping state. However, for both of the two coupled micromaser systems there is no external mechanism to allow an escape from the trapping state, regardless of the strength of coupling.

Though the variation in $\langle n \rangle$ is much more constrained in the coupled micromaser systems, the effect of the coupling is quite different in each one. The coherently coupled system has more resemblance to the coherently driven single micromaser in that the effect of the coupling tends to increase the average photon numbers; the opposite is true for the dissipatively coupled system. There is another, less severe, trapping state located at $\Theta \simeq 5$. Here, the effect of coupling in the coherently coupled system is to immediately destroy this state, as in the driven micromaser case. For the dissipatively coupled system the $\Theta \simeq 5$ trapping state is hardly affected, as is the $\Theta \simeq 7$ trapping state. At $\Theta \simeq 6$ there is very little movement in $\langle n \rangle$ for the coherently coupled micromasers, yet this is the location of the most movement in $\langle n \rangle$ for the dissipatively coupled micromasers. Looking at the Fano factor, for the coherently coupled micromasers an increase in coupling strength seems to consistently make the photon distribution more super-Poissonian, whereas this is not true for dissipative coupling.

Figure 5.3 compares the photon probability distributions over a range of drive strengths of (a) a driven micromaser with (b) two coherently coupled micromasers. Four values of Θ were chosen at $N = 5$: $\Theta = 0.9619$ (near the masing threshold), $\Theta = 2.998$ (has the same $\langle n \rangle$ value as $\Theta = 0.9619$ when $\varepsilon = 0$), $\Theta = 4.5$ and $\Theta = 7.022$ (a trapping state). For the four values of Θ chosen, $P(n)$ for the dissipatively coupled system is very similar to

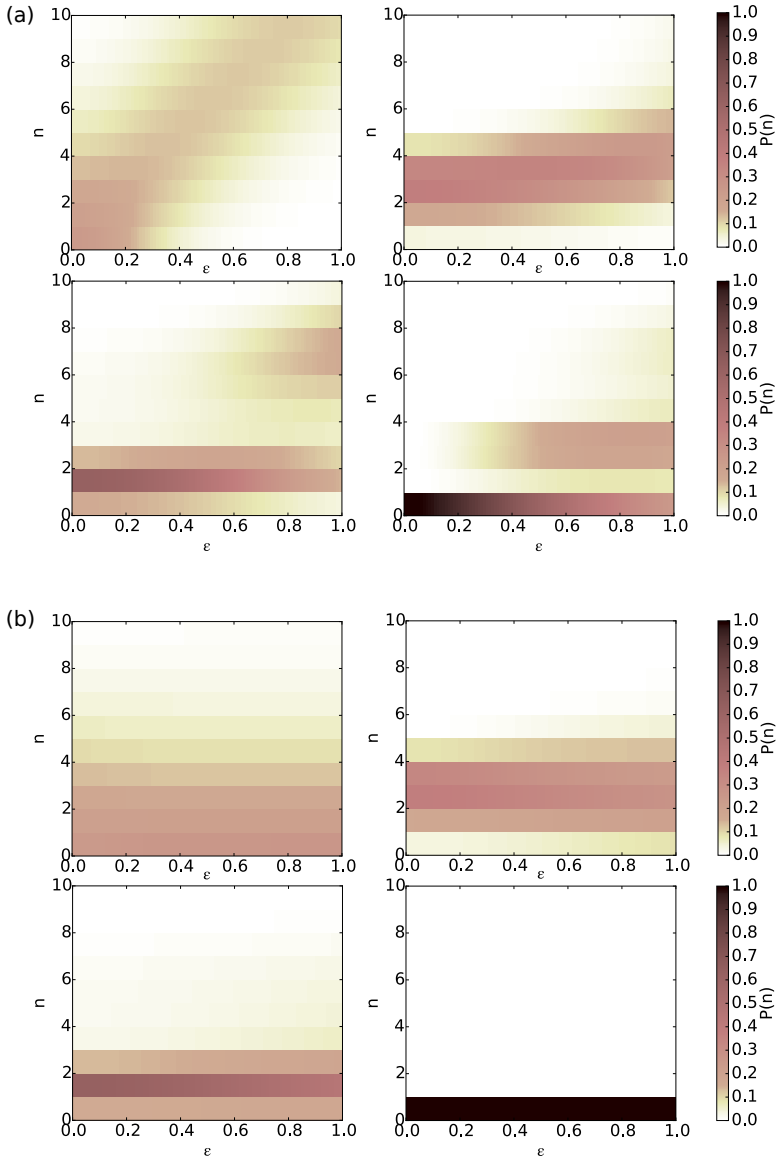


Figure 5.3: The photon probability distribution $P(n)$ over n with increasing ε at $N = 5$ for (a) a single driven micromaser and (b) one of two coherently coupled micromasers. For each system four values of Θ are shown (clockwise from top-left): $\Theta = 0.9619$, $\Theta = 2.998$, $\Theta = 7.022$ and $\Theta = 4.5$.

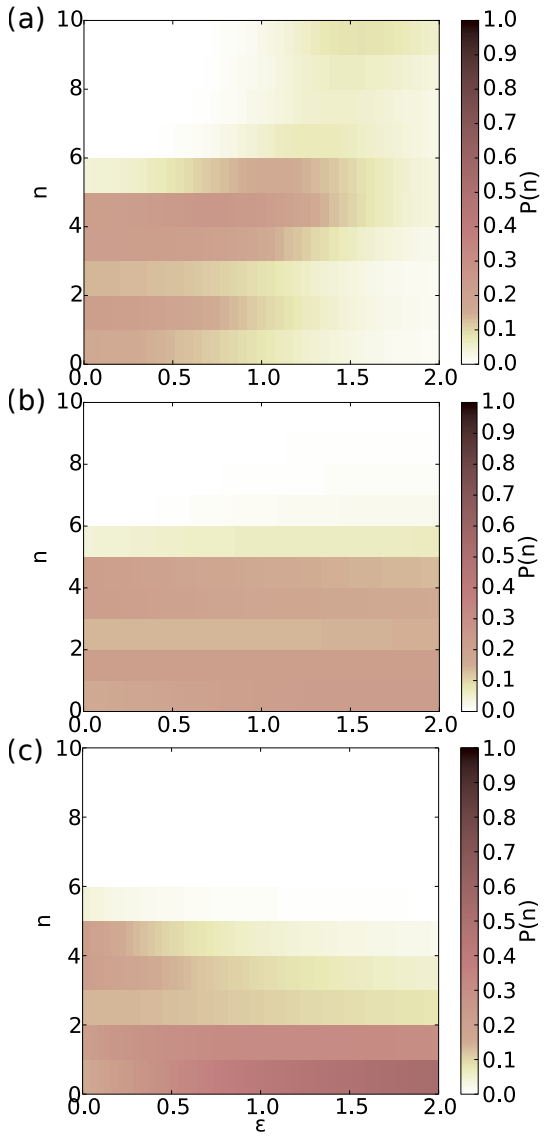


Figure 5.4: The photon probability distribution $P(n)$ over n with increasing ε at $N = 5$ for the bistable state at $\Theta = 5.8$. (a) A single driven micromaser, (b) one of two coherently coupled micromasers, and (c) one of two dissipatively coupled micromasers.

(b), so is not shown. Once again there is a clear difference in how the coupling strength affects each system. For the externally driven micromaser the drive dramatically changes the distribution near the threshold even at a very weak coupling. The trapping state quickly becomes a bistable state. For the other two values of Θ the distribution remains stable at first, but at higher drive strength becomes more distorted. In contrast, the distributions in the coherently coupled micromasers remain quite resistant to the coupling strength and form a very different picture to the single micromaser system.

Figure 5.4 looks at the photon probability distribution for all three systems at $\Theta = 5.8$, a value that has a bistability for an uncoupled micromaser. The bistability is less well-defined at the low value of $N = 5$ but it is clear that the effect of the coupling strength is quite different in each system. For the driven micromaser the bistability is sustained until enough external energy is in the system to distort the photon distribution. The coherently coupled system sustains the bistability with an increase in coupling strength, moving slightly towards a wide single distribution at large ε values. For the dissipatively coupled system the bistability is destroyed with a moderate value of ε, moving towards a stronger peak close to the ground state.

The comparison with the driven micromaser has shown that the amplitude of the limit cycle for two coupled micromasers is less sensitive to the coupling strength. However, synchronisation is still a property that emerges with weak coupling, so we will remain in the small-ε regime.

5.2 Relative Phase Distribution

Previously, our main measure of phase synchronisation was the phase probability distribution, which is determined by the off-diagonal elements of the steady-state density matrix containing phase information. For a system with two oscillators, we must instead measure the relative phase between the oscillators, given in Eq. 3.2.4, which can also be written in the form of a Fourier series

$$P(\varphi_-) = \frac{1}{2\pi} + \frac{1}{\pi}\mathrm{Re}\left[\sum_{k=1}^{\infty} \mathrm{e}^{ik\varphi_-} \sum_{n=0,m=0}^{\infty} \rho_{n,m}^{(k)}\right], \tag{5.2.1}$$

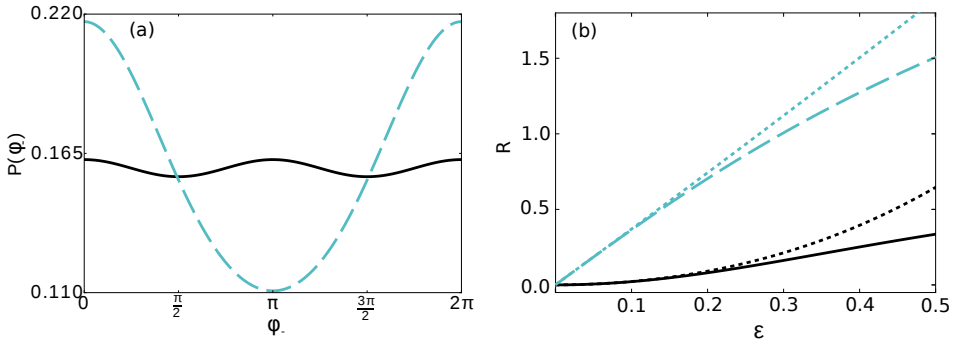


Figure 5.5: (a) The relative phase probability distributions for the coherent (black, solid) and dissipative (blue, dashed) coupled micromasers with $\varepsilon = 0.1$. (b) R as a function of the coupling strength ε, where the dotted lines are the perturbation theories developed in Sec. 5.2.2. For both, $N = 5$ and $\Theta = 2$.

for the relative phase $\varphi_- = \varphi_A - \varphi_B$ of two oscillators A and B, where $\rho^{(k)}_{n,m} = \langle n, m+k|\rho|n+k, m\rangle$ in the number state basis.

We can see what this distribution looks like in Fig. 5.5 (a). For the dissipative coupling, the function is 2π-periodic as the phase distribution was for a driven micromaser in Fig. 3.3. The amplitude of the relative phase distribution is also similar to that of the driven micromaser case, but the function is shifted by $\pi/2$. In contrast, the relative phase distribution for the coherent coupling has an amplitude much smaller than the dissipative coupling, and it is π-periodic. The difference in periodicities of the distributions can be predicted by following the same method shown from Eq. 4.1.2 onwards. For the coherently coupled system, two stable fixed points for the phase are found, at $\varphi_0 = \pi$ and $\varphi_0 = 2\pi$.

Once again, we can condense the information in the phase distribution to a number that we can use as a measure of phase synchronisation: $R = 2\pi \max[P(\varphi_-)] - 1$. Figure 5.5 (b) shows R for each coupled micromaser system as a function of the coupling strength, for the same parameters used in Fig. 5.5 (a). For weak coupling, R in the dissipatively coupled system rises much more rapidly than for the coherently coupled system, and as a different function of ε. For dissipative coupling the relationship is approximately linear for small ε, but for the coherent coupling it is approximately

quadratic.

The two-micromaser systems are limited to a low-N regime if we want to solve them numerically for the steady state, so it is useful to develop approximations that could allow us to extend the range of parameters that we are able to investigate. The next sections look at semiclassical and perturbation approximations, and in Sec. 5.2.3 these are compared to the numerics.

5.2.1 Semiclassical Approximation

For the semiclassical description, we will only look at the dissipatively coupled system, which is the simpler case. We begin with the equation of motion for the relative phase

$$\dot{P}(\varphi_-,t) = \frac{1}{\pi}\mathrm{Re}\left[\sum_{k=1}^{\infty} \mathrm{e}^{ik\varphi_-} \sum_{n,m=0}^{\infty} \dot{\rho}^{(k)}_{n,m}\right], \tag{5.2.2}$$

which contains the master equation of the system $\dot{\rho}^{(k)}_{n,m}$. The master equation written in the number state basis is

$$\begin{aligned}\dot{\rho}^{(k)}_{n,m} = &-\left[\frac{\mu^{(k)}_n + \mu^{(k)}_m}{2} + c^{(k)}_n + d^{(k)}_n + c^{(k)}_m + d^{(k)}_m\right]\rho^{(k)}_{n,m} \\ &+ c^{(k)}_{n-1}\rho^{(k)}_{n-1,m} + c^{(k)}_{m-1}\rho^{(k)}_{n,m-1} + d^{(k)}_{n+1}\rho^{(k)}_{n+1,m} + d^{(k)}_{m+1}\rho^{(k)}_{n,m+1} \\ &+ \Lambda^{(k)}_{n,m},\end{aligned} \tag{5.2.3}$$

where $\Lambda^{(k)}_{n,m}$ are the coupling terms, which for the dissipative coupling are

$$\begin{aligned}\Lambda^{(k)}_{n,m} = -\tilde{\varepsilon}\Big[&\sqrt{(n+1)(m+1)}\rho^{(k-1)}_{n+1,m+1} + \sqrt{(n+k+1)(m+k+1)}\rho^{(k+1)}_{n,m} \\ &- \frac{1}{2}\sqrt{n(m+k+1)}\rho^{(k+1)}_{n-1,m} - \frac{1}{2}\sqrt{(n+k+1)m}\rho^{(k+1)}_{n,m-1} \\ &- \frac{1}{2}\sqrt{(n+1)(m+k)}\rho^{(k-1)}_{n+1,m} - \frac{1}{2}\sqrt{(n+k)(m+1)}\rho^{(k-1)}_{n,m+1}\Big].\end{aligned} \tag{5.2.4}$$

Now we can introduce some approximations. Firstly we assume we are in the semiclassical limit so that $\langle n\rangle \gg 1$. We will also assume that we have weak coupling where $\tilde{\varepsilon} \ll 1$ so that $k \ll n, m$. This is due to the fact that larger k terms have a higher-order dependence on ε. The final assumption is that the photon number distribution is strongly peaked around its average value so that $n \to \langle n\rangle$; this occurs when the limit cycle is well-defined. In

micromaser systems this is valid when Θ is above the threshold, but before bistable or other more complex states appear.

Applying these approximations to the master equation (details in Appendix D) yields a much simpler master equation, which can be used in Eq. 5.2.2. We can then rewrite the simplified phase evolution equation so that it takes the form of a Fokker-Planck equation

$$\dot{P}(\varphi_-) = \left(\frac{\mathrm{d}}{\mathrm{d}\varphi_-} A_{\varphi_-} + \tilde{D} \frac{\mathrm{d}^2}{\mathrm{d}\varphi_-^2} \right) P(\varphi_-), \tag{5.2.5}$$

where $A_{\varphi_-} = -\tilde{\varepsilon} \sin \varphi_-$ and $\tilde{D} = \frac{\tilde{N}\phi^2+1}{4\langle n \rangle}$ is the micromaser linewidth. We can now find the standard steady-state solution for an equation of this form [98] to end up with

$$P(\varphi_-) = \frac{1}{2\pi I_0(\tilde{\varepsilon}/\tilde{D})} \mathrm{e}^{\tilde{\varepsilon} \cos \varphi_- / \tilde{D}}. \tag{5.2.6}$$

The form of the semiclassical relative phase distribution is similar to that of the single driven micromaser in Eq. 4.1.20. However, the two-micromaser system has a cosine term instead of sine in the exponential term, and the phase drift term A_φ does not have any dependence on the average number of photons in the system, unlike the driven micromaser.

5.2.2 Perturbation Theory

As with the single driven micromaser, for the two-micromaser systems we can make use of the analytical expression for an uncoupled micromaser and add a perturbation in the coupling terms to provide a solution for the weak coupling limit, where any higher-order terms of ε are considered small enough to be neglected.

Coherent Coupling

The master equation for the system is given by Eq. 5.2.3, to which we can add the terms that arise due to the coherent coupling

$$\begin{aligned} \Lambda_{n,m}^{(k)} \;=\; & -i\varepsilon \Big[\sqrt{n(m+k+1)}\rho_{n-1,m}^{(k+1)} + \sqrt{(n+1)(m+k)}\rho_{n+1,m}^{(k-1)} \\ & - \sqrt{m(n+k+1)}\rho_{n,m-1}^{(k+1)} - \sqrt{(n+k)(m+1)}\rho_{n,m+1}^{(k-1)} \Big]. \end{aligned} \tag{5.2.7}$$

In the steady state $\dot{\rho}^{(k)}_{n,m} = 0$, and we have a set of linear equations that can be solved for $\rho^{(k)}_{n,m}$, using the same method set out in Appendix B. For $\varepsilon = 0$ in the off-diagonal case ($k \neq 0$) the solutions are $\rho^{(k)}_{n,m} = 0$. To first order, since the terms in Eq. 5.2.7 are replaced with the unperturbed values and the only non-zero unperturbed terms are the diagonal ones $\rho^{(0)}_{n,m} = P_n P_m$ (here P_n is the steady-state number distribution of a single unperturbed micromaser), we only need to look at the $k = 1$ case. This means that the coupling terms in Eq. 5.2.7 become

$$\Lambda^{(1)}_{n,m} = -i\varepsilon\sqrt{(n+1)(m+1)}\,(P_{n+1}P_m - P_{m+1}P_n)\,. \tag{5.2.8}$$

Since $P_{n(m)}$ are real, this makes $\rho^{(1)}_{n,m}$ imaginary. However, $\Lambda^{(1)}_{n,m} = -\Lambda^{(1)}_{m,n}$ and therefore $\rho^{(1)}_{n,m} = -\rho^{(1)}_{m,n}$. Using Eq. 3.2.4 we can see that this means the sum of all the $k = 1$ elements is zero and that $P(\varphi_-) = 1/2\pi$ to first order.

To obtain the phase information then, we will need to go to second order. Despite the first-order coupling terms $\Lambda^{(1)}_{n,m}$ not contributing to $P(\varphi_-)$, they do contribute to the second-order terms in $\rho^{(2)}_{n,m}$. The $\Lambda^{(2)}_{n,m}$ terms are now real and proportional to ε^2, so the relative phase distribution takes the form

$$P(\varphi_-) = \frac{1}{2\pi}\left[1 + \varepsilon^2 C_0 \cos(2\varphi_-)\right], \tag{5.2.9}$$

where C_0 is a constant which depends on the properties of the uncoupled micromasers (ϕ and N).

Dissipative coupling

We now look at what happens for dissipative coupling described by Eq. 5.1.6. We can write the coupling terms in the form in Eq. 5.2.4, remembering that we have rescaled the parameters $\tilde{N} = N/(1+\varepsilon)$, $\tilde{\varepsilon} = \varepsilon/(1+\varepsilon)$.

Working through the same steps that were made in the coherent coupling case, we can see that at first order only the $k = 1$ term is non-zero,

$$\Delta^{(1)}_{n,m} = \frac{\tilde{\varepsilon}}{2}\sqrt{(n+1)(m+1)}\,[P_{n+1}P_m + P_n P_{m+1} - 2P_{n+1}P_{m+1}]\,. \tag{5.2.10}$$

Contrary to the coherent coupling case, the non-zero components of $\rho^{(1)}_{n,m}$ are all real with $\rho^{(1)}_{n,m} = \rho^{(1)}_{m,n}$ and the sum in Eq. 3.2.4 contributes to $P(\varphi_-)$. Therefore, for dissipative coupling the relative phase distribution (to lowest order) is

$$P(\varphi_-) = \frac{1}{2\pi}\left[1 + \varepsilon C_1 \cos(\varphi_-)\right]. \tag{5.2.11}$$

The forms of the perturbation calculations 5.2.9 and 5.2.11 are general, with only the constants C_0 and C_1 giving information on the properties of the micromaser systems. Even before calculating these constants, we can see that these general forms match the numerical calculations in Fig. 5.5 for low coupling. We must solve for the constants numerically using the method described in Appendix B.1, but since this is far less computationally difficult than solving the full system exactly it is useful for exploring system parameters that would otherwise be impracticable.

5.2.3 Comparison of Approximations to Numerical Solution

For dissipative coupling, we can compare the three different calculations: semiclassical, perturbation theory and numerics using the full master equation. Figure 5.6 shows R as a function of Θ and compares the numerical solution to (a) the semiclassical calculation and (b) the perturbation theory. The shape of the phase locking over Θ is very similar to that of the average number of photons shown in Fig. 5.6 (c). The strongest phase locking corresponds to the largest number of photons, and there is a dip in phase locking in the $\Theta = 4.97$ trapping state. The strength of the drive appears to increase the phase locking relatively much more than the average photon number; the large movement in phase together with small movement in amplitude of the limit cycle is indicative of synchronisation.

Figure 5.6 (a) shows that the semiclassical calculation consistently underestimates the phase locking beyond the initial peak close to the threshold. This is the same as for the driven micromaser case, where a semiclassical approximation that assumed $\langle n \rangle \gg 1$ also underestimated the phase locking for $N = 5$. The perturbation theory does much better above the threshold, only overestimating the phase locking slightly. The inset figures show that the relative accuracy of the semiclassical calculation remains the same regardless of the coupling strength, whereas the perturbation theory works better at low values of ε. Despite this, the perturbation theory still does much better than the semiclassical approximation at $\varepsilon = 0.1$, particularly in the $2 < \Theta < 4$ region.

Both approximations are far less computationally demanding than the full numerical solution, so by ensuring ε is sufficiently small we may treat the perturbation theory as a close approximation of R and see how the semi-

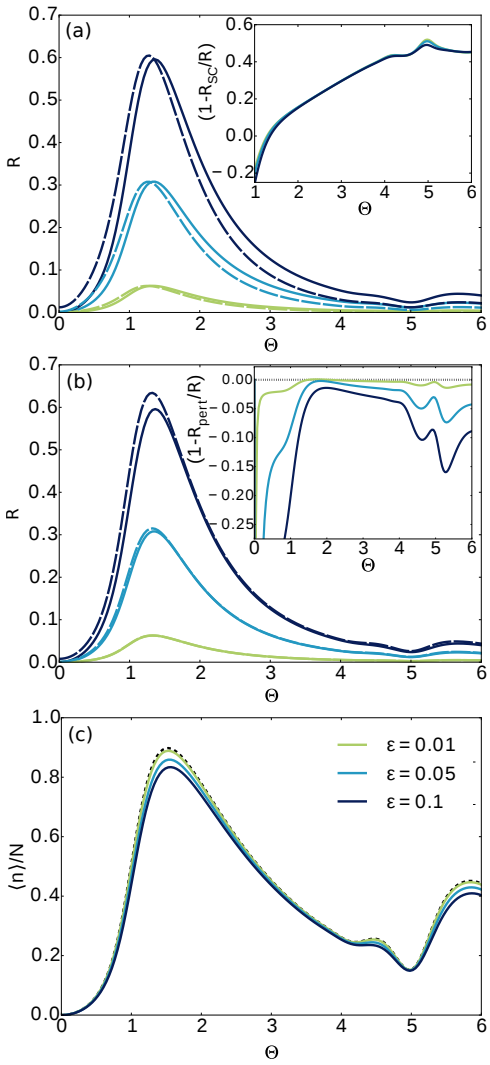


Figure 5.6: For the dissipatively coupled system at $N = 5$, a comparison over Θ of R (solid), calculated using the full master equation, with (a) the semiclassical approximation and (b) the perturbation theory of R (both dashed) for three values of the coupling strength ε. Inset are the relative values of the approximations and the numerical solutions to R, for each value of ε. (c) The behaviour of the average photon number for the same parameters and coupling values as for (a) and (b), with a dashed line as the reference for the uncoupled case.

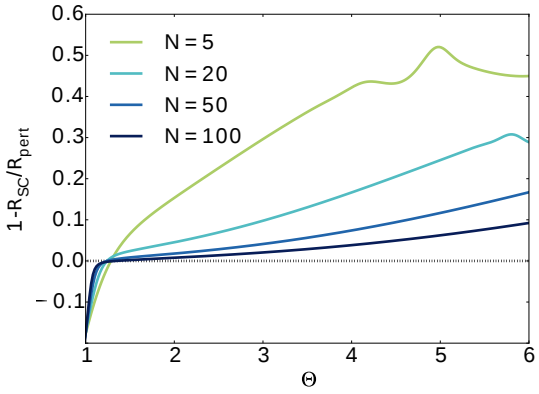


Figure 5.7: For the dissipatively coupled system, the relative difference between the semiclassical and perturbation calculations for increasing values of N at $\varepsilon = 0.0001$.

classical calculation does at higher values of N. Figure 5.7 directly compares the perturbation theory and semiclassical calculations over a range of Θ up to $N = 100$. It is clear that although the semiclassical calculation did not fare very well in the more quantum regime of $N = 5$, it gets much more accurate at large values of N, showing that it does indeed capture the behaviour in the limit of large photon numbers. Due to the fact that the accuracy of the semiclassical approximation seems not to depend very much on the coupling strength, when both N and ε are large it will be more accurate than the perturbation theory for most values of Θ.

5.3 Mutual Information and Entanglement

Two coupled micromasers are a bipartite system and as such we can examine various correlations between the subsystems to see how they compare with the relative phase, our synchronisation measure of choice up to this point. Many different information-based witnesses and correlations have been suggested [108], as discussed in Sec. 3.2.1, but here we will look at two in particular: mutual information and entanglement.

5.3.1 Mutual information

Mutual information has been proposed as an order parameter for synchronisation in quantum systems [34] and appears to be a good measure for certain parameters in coupled quantum van der Pol oscillators and qubits.

Mutual information is defined as

$$\mathcal{I} = \mathcal{S}(\rho_A) + \mathcal{S}(\rho_B) - \mathcal{S}(\rho), \tag{5.3.1}$$

using the von Neumann entropy, $\mathcal{S}(\rho) = -\mathrm{Tr}[\rho \ln \rho]$, where $\rho_{A\,(B)}$ is the reduced density matrix of micromaser $A\,(B)$ and ρ is the density matrix of the full system.

Figure 5.8 (a) compares the mutual information for both the coherent and dissipative couplings. For low-ε both systems behave very similarly, and they both grow quadratically. Figure 5.5 (b) shows a completely different picture; the growth of the relative phase for each system is distinct even from very weak coupling. Figures 5.8 (b) and (c) extend the comparison between R and $\mathcal{I}$ to non-zero detuning between the dissipatively coupled micromasers. Regardless of the coupling strength, the behaviour between the two measures is quite different in how the two Θ values decay with Δ.

For all types of coupled systems, the strength of any correlations will increase with the strength of the coupling, so it is important to select correlations that contain the relevant information. For these micromaser systems, the information that is captured in the mutual information is not similar enough to that captured in the relative phase distribution for it to be a useful measure of synchronisation.

5.3.2 Entanglement

Entanglement is a truly quantum phenomenon, and although it cannot be calculated for classical or semiclassical systems we have seen that the micromaser can exhibit very quantum behaviour – such as sub-Poissonian distributions, number squeezing, and negative Wigner functions – so it will be useful to see if entanglement could be used for describing quantum synchronisation in this case.

Here we will use the logarithmic negativity (introduced in Sec. 3.2.1) to

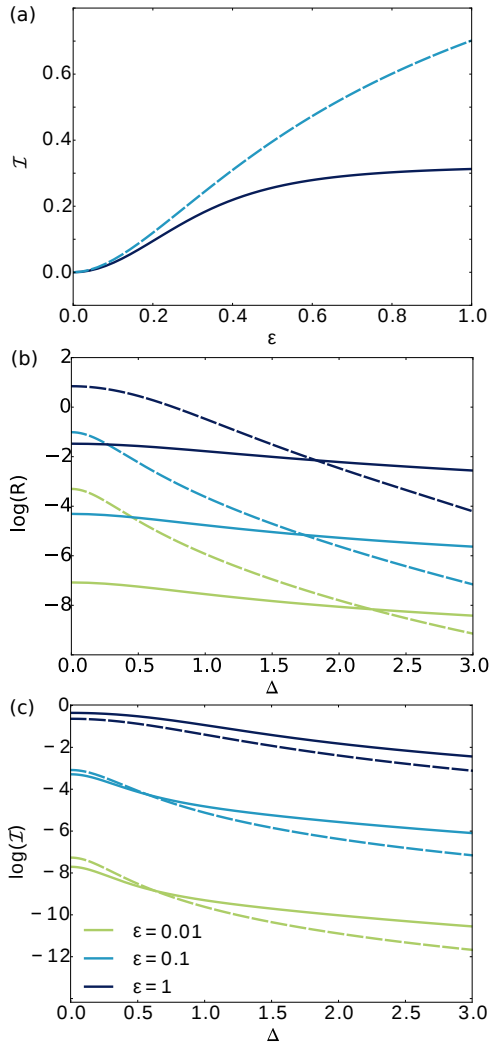


Figure 5.8: (a) Mutual information $\mathcal{I}$ as a function of the coupling strength ε for coherent (solid) and dissipative (dashed) couplings, at $\Theta = 2$. In the dissipatively coupled system, a comparison of (b) R and (c) the mutual information as a function of the detuning for three values of the coupling strength, at $\Theta = 1$ (solid) and $\Theta = 2$ (dashed).

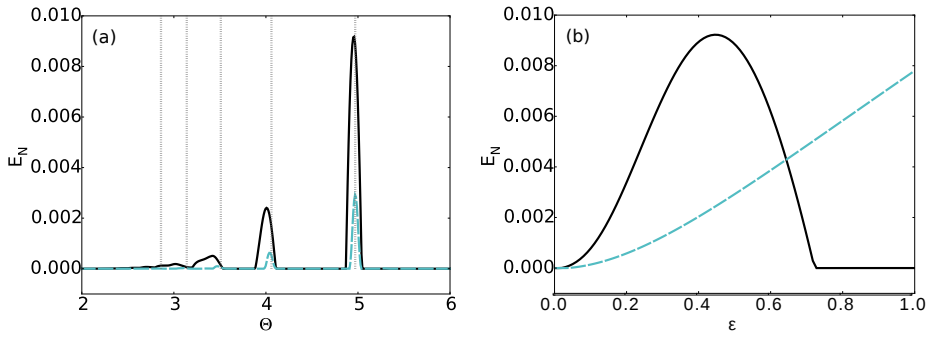


Figure 5.9: (a) Entanglement calculated by logarithmic negativity as a function of Θ at $\varepsilon = 0.5$, with the locations of trapping states indicated by the dotted lines. (b) Entanglement at the trapping state $\Theta = 4.97$ as a function of ε for the two coupled systems. The solid lines are for the coherently coupled system, and the dashed are for the dissipatively coupled system, with $N = 5$.

quantify the entanglement in the micromasers. The negativity is $N(\rho) = \frac{1}{2}\sum_i (|\lambda_i| - \lambda_i)$ where λ_i are the eigenvalues of the partial transpose of the density operator of the system. The logarithmic negativity is given by [111]

$$E_N(\rho) = \log_2 [2N(\rho) + 1] . \tag{5.3.2}$$

Figure 5.9 (a) shows the entanglement for both coupled micromaser systems as a function of Θ. Even for a relatively large coupling strength of $\varepsilon = 0.5$ and with low photon numbers at $N = 5$, very little entanglement is observed for either system. In fact, the only non-zero entanglement occurs at the trapping state locations in Θ, indicated by the dotted lines. As we saw in Sec. 2.2, these correspond to the locations where $\sin(\phi\sqrt{n+1}) = 0$, and from right to left in the figure the dashed lines show the locations for $n = 1, 2, 3, 4, 5$. In this figure, despite the dissipative coupling showing less entanglement the two couplings appear to behave similarly. However, this is not the case in general. Figure 5.9 (b) looks at the trapping state at $\Theta = 4.97$ and shows that the two couplings behave very differently when the coupling strength is varied. The dissipative coupling increases steadily whereas the coherent coupling reaches a peak, then drops back to zero (though there is a revival at larger ε). This could potentially be linked to the restricted state space, as was found in a similar system [71].

5.4 Summary and Conclusions

This chapter looked at two identical micromasers coupled coherently (via Hamiltonian terms) and dissipatively (via Lindblad terms). The properties of these two systems were compared with the single driven micromaser that was discussed in chapter 4. However, due to constraints on the numerics for two coupled micromasers, the parameter N was limited to $N = 5$.

For the single micromaser, the external drive meant that the properties of the system were very sensitive to the coupling strength, and in particular the average photon number in the cavity was affected by this. For the two-micromaser systems the photon numbers were much more constrained, and states that were easily destroyed in the driven system (such as trapping and bistable states) behaved quite differently. The different types of coupling in the two-micromaser systems also led to quite different behaviour depending on the value of Θ – a clear example of this was the bistability at $\Theta = 5.8$, which was stable for coherent coupling, but collapsed with increased dissipative coupling.

To measure synchronisation in these two-oscillator systems the relative phase distribution was used. Once again there were large differences when comparing the two systems. The coherent coupling gave a π-periodic distribution with a smaller amplitude, whereas the dissipative coupling was 2π-periodic and had a much larger amplitude. The maxima of the distributions, measured by R, also evolved differently to each other as a function of the coupling strength.

Two analytic approximations were developed: a semiclassical approximation and a perturbation theory. To compare the approximations to the numeric solutions, we focussed on the dissipatively coupled system. As expected due to the nature of the assumptions made in the approximations, the perturbation calculation did well for very small coupling values. At $N = 5$, the semiclassical calculation fared slightly less well, but was consistent over all coupling strengths. Both approximations were far less computationally demanding than the full numerical solution. Ensuring a sufficiently weak coupling strength so that the perturbation calculation is very accurate, we could then compare the two approximations at larger values of N and found that the accuracy of the semiclassical calculation improved

vastly as N was increased, which is what we would expect given the increase in average photon numbers with N. The semiclassical approximation, based on a Fokker-Planck equation, underestimated synchronisation – this is consistent with a similar semiclassical approximation made for coupled van der Pol oscillators [25], which also underestimated the strength of synchronisation.

Finally, we explored the role of information measures as synchronisation witnesses in bipartite systems. We looked at the mutual information, calculated using the von Neumann entropy, and entanglement. Mutual information increased with the strength of coupling for both the coherent and dissipative systems, but in a very different way to the phase measure R, and this continued even when off-resonance. Despite the fact that micromasers can exhibit very quantum properties and we were in a low-photon number regime, there was very little entanglement in either coupled system. There were, however, small peaks in entanglement corresponding to the locations of the trapping states in Θ, where there were the lowest photon numbers. At the trapping state $\Theta = 4.97$, the entanglement as a function of the coupling was very different depending on whether the micromasers were coherently or dissipatively coupled. Whilst the entanglement consistently rose with dissipative coupling, it peaked then fell back to zero with coherent coupling, though there was a revival at even larger coupling strengths.

Chapter 6

Many-Body Quantum Synchronisation

The previous two chapters have looked at the synchronisation of a self-sustained oscillator with a drive and the mutual synchronisation of two coupled oscillators. This chapter examines a third type of synchronisation: that of a large array of globally coupled oscillators. In classical systems of this type, phase synchronisation typically emerges spontaneously once the coupling has exceeded a critical value. Adding noise tends to increase this critical value and decrease the maximum synchronisation of the oscillators [119].

Recently, coupled cavity or circuit QED arrays treated using a mean-field model have been shown to exhibit non-equilibrium quantum phase transitions [120, 121]. How quantum noise affects transitions to synchronisation is a new area of research [17] and an interesting exploration of synchronisation of many quantum oscillators was undertaken by Lee and Sadeghpour in 2013 [25], who directly compared mean-field models of coupled classical and quantum van der Pol oscillators. They found that there were clear distinctions between the two cases, with synchronisation occurring at weaker coupling in the quantum case.

In the first part of this chapter, Sec. 6.1, we consider the mean-field quantum van der Pol model and significantly expand on the work in [25] by exploring various system properties as a transition occurs. In Sec. 6.1.1 we look in detail at the evolution of the state, and the nature of the bistability

that occurs. We explore the critical scaling behaviour close to the transition in Sec. 6.1.2, then go on to look at the steady-state properties in Sec. 6.1.3 including the phase/number uncertainty behaviour. The second half of the chapter, Sec. 6.2, investigates a similar many-body system but with coupled micromasers. Once again the evolution and transition are studied in detail (Sec. 6.2.1) before the critical scaling is examined (Sec. 6.2.2). In Sec. 6.2.3 the steady-state properties are compared over a wider range of the system parameters. A summary of the chapter is provided in Sec. 6.3, and finally the future directions this work could take are discussed in Sec. 6.4.

6.1 Coupled Quantum van der Pol Oscillators

The master equation for an uncoupled quantum van der Pol oscillator is Eq. 2.1.5, where the rates κ_1 and κ_2 describe the gain and loss of photons in the system. To model a large array of oscillators with all-to-all coupling, a self-consistent mean-field approach is used [17, 25]. The Hamiltonian that describes the simplest form of coherent coupling between the oscillators is

$$H_{\mathrm{vdP}} = \frac{\varepsilon}{M} \sum_{i<j} \left(a_i a_j^\dagger + a_i^\dagger a_j \right) \tag{6.1.1}$$

where M is the total number of oscillators and ε is a parameter that describes the strength of coupling between them. Using a Gutzwiller ansatz [122] $O_i^\dagger O_j \approx \langle O_i^\dagger \rangle O_j + O_i^\dagger \langle O_j \rangle - \langle O_i^\dagger \rangle \langle O_j \rangle$ we can simplify Eq. 6.1.1, and in the limit of a large number of coupled oscillators ($M \to \infty$) the approximation approaches an exact description. We will also be considering identical oscillators, so the sum reduces to a single index. Although all-to-all coupling is considered to simplify the calculations, work has recently been done to suggest that this can in fact be achievable in certain quantum systems [123].

Combined, these approximations reduce the Hamiltonian to [25]

$$H_{\mathrm{vdP}} = \varepsilon \left(\langle a \rangle a^\dagger + \langle a^\dagger \rangle a \right). \tag{6.1.2}$$

This approach looks at a single site in the array, whose state depends on the average of its neighbours. In order to find the steady state, an initial trial value of ρ is assumed from which a value of $\langle a \rangle$ is obtained, then both ρ

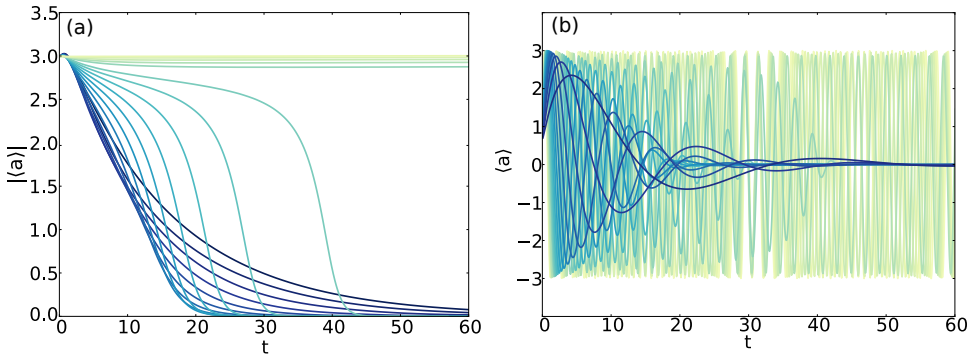


Figure 6.1: The evolution of (a) $|\langle a \rangle|$ and (b) $\langle a \rangle$ as the self-consistent master equation converges towards a steady state, from $\varepsilon = 1.5$ (dark blue) to $\varepsilon = 3.9$ (light yellow). Here, $\kappa_2/\kappa_1 = 0.04$.

and $\langle a \rangle$ are updated each time step until convergence (details are provided in Appendix E).

In classical systems, the usual order parameter for phase locking is the average amplitude of the phase preference over all oscillators [92], $r = (1/M)|\sum_{m=1}^{M} \alpha_m|$, with $\alpha_m = R_m e^{i\varphi_m}$ the amplitude for each oscillator. For mean-field models r is usually zero for weak coupling values, until a critical value is reached and a bifurcation occurs [92]. Any value $r > 0$ indicates a partial synchronisation, or synchronisation of some of the oscillators in the system, and as the coupling between the oscillators increases this approaches full synchronisation of the entire system. The equivalent of α_m in the quantum system is a_m [25], and in the mean-field model where $M \to \infty$, $r = |\langle a \rangle|$. Most classical cases that use this model initiate the oscillators with a distribution of similar but non-identical frequencies, and do not account for noise in the system. Here, we (as per the Lee and Sadeghpour approach [25]) have identical oscillators in a system that has quantum noise.

Figure 6.1 shows the iterative evolution to a steady state for $|\langle a \rangle|$ and $\langle a \rangle$ with a variety of couplings strengths ε. In Fig. 6.1 (a) there appear to be three main types of evolution. At low ε, there is an approximate exponential decay to zero. We can see from Fig. 6.1 (b) that the phase is actually oscillating in time, but for low ε the period of the oscillations are longer and they decay quickly to zero, indicating no preferred phase. For high ε, above a critical value, the period of the oscillations is much shorter and the

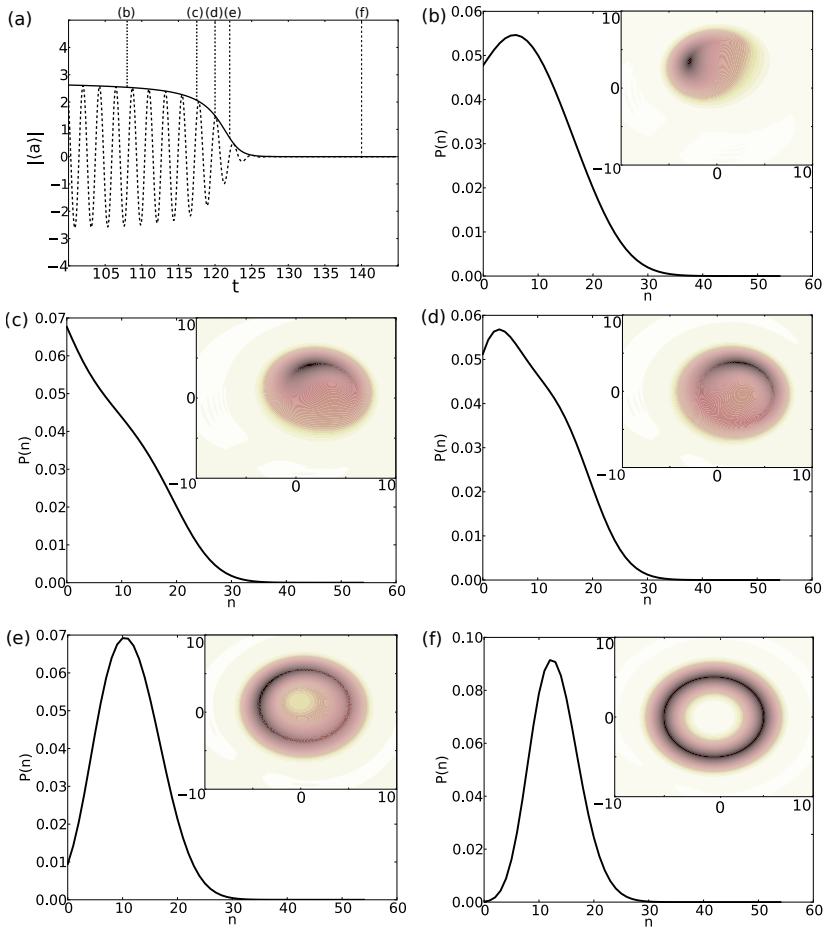


Figure 6.2: (a) Looking at the final decay of $|\langle a \rangle|$ for $\varepsilon = 2.9$ in detail. (b)–(f) The photon number probability distribution $P(n)$ and the Wigner function (inset) for different times in the decay, indicated in (a). Here, $\kappa_2/\kappa_1 = 0.04$.

amplitude settles to a constant value leading to a steady state (albeit one with an oscillatory phase). In between the high and low ε behaviours, a different type of decay is seen. The amplitude of the phase oscillations seems to reach an almost constant value, decaying very slowly with time, until it decays on a much more rapid timescale to zero. The closer ε gets to the critical value where the non-decaying steady state with $|\langle a \rangle| = 0$ appears, the longer the slow timescale decay becomes.

During the slow timescale evolution, the state behaves similarly to the synchronised steady state, but is slowly decaying. It is informative to see how this rapidly decays to its final, unsynchronised steady state. Figure 6.2 looks at exactly how the fast timescale decay occurs, using both the number dis-

tribution and Wigner function. The photon number n begins with a fairly broad distribution with a peak at low photon numbers. As the state decays, this peak becomes less well-defined and the distribution broadens even further. However, close to the steady state it narrows again, and finally settles with a sharper distribution than where it began, with a peak at higher photon numbers. During the decay the peak passes through zero, which seems to provide an effective mechanism for destroying phase information. The Wigner distribution can give us additional information about the phase during this transition. It starts with one peak, off-centre, that rotates with time, showing that there is always a preferred phase but the value of this phase oscillates with time (as we can see looking at $\langle a \rangle$ in Fig. 6.1). As the decay progresses, the amplitude of the Wigner function increases and the peak begins to smear around a central dip. Finally, it shows a clear limit cycle state with no phase preference – the equivalent of an uncoupled van der Pol oscillator. It is interesting to note that at no point is the Wigner function negative, as can sometimes happen with strongly non-classical states.

6.1.1 Bistability and the Nature of the Transition

As the coupling strength reaches a critical value, there is a discontinuous jump in the steady-state values of $|\langle a \rangle|$ indicating a transition from an unsynchronised to a synchronised state. The behaviour of a new timescale emerging close to (and appearing to diverge at) the transition is reminiscent of the "critical slowing down" seen in classical critical dynamics close to a second-order transition [124], but similar behaviour is also seen by Marcuzzi et al. in a nonequilibrium quantum system [125]. Here, nonequilibrium dynamics causes a dynamical transition to occur around the spinodal lines of the mean-field phase diagram.

Marcuzzi et al. introduce a phenomenological potential model to help explain the dynamics of their system. Likewise, we can suggest an effective potential for $r = |\langle a \rangle|$,

$$V(r) = r_0 + \frac{r^2}{8\varepsilon} - \frac{r^4}{4} + \frac{r^6}{6}, \tag{6.1.3}$$

where r_0 is a constant. Figure 6.3 presents a qualitative picture using the effective potential to explain why $|\langle a \rangle|$ might decay with strongly differing timescales. The rate of change of r in time is assumed to depend only on the

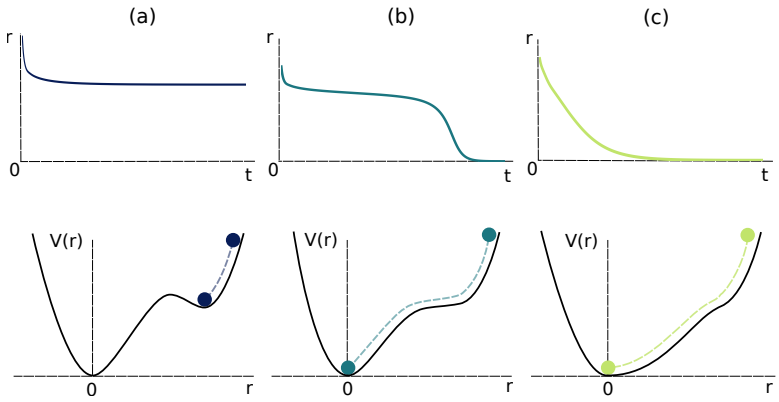


Figure 6.3: An illustration of how looking at effective potentials could help in understanding the evolution of $|\langle a \rangle|$ at (a) ε above a critical value (b) close to, but below, a critical value and (c) well below a critical value.

gradient, $\dot{r} = -\partial V/\partial r$, and (since there is no kinetic component) as soon as the gradient in the potential becomes zero r will reach a steady state. The form of the potential has been chosen so that a stable solution at $r = 0$ always exists (as noted in [25]), however a non-zero steady state can also exist depending on the value of ε and initial position in r.

As we vary ε we move from a single stable fixed point to a pair of stable and unstable fixed points, plus the original fixed point. This type of bifurcation is known as a saddle-node bifurcation in non-linear dynamics [126]. Above the critical value of ε in Fig. 6.3 (a) two stable steady-state solutions exist, $r = 0$ and $r > 0$. However we can also see a third, unstable solution in the form of a peak between the two minima in the potential. Figure 6.3 (b) shows the potential close to, but below the critical value of ε. There is only one solution at $r = 0$, but the gradient of the potential becomes very shallow, and correspondingly the long timescale decay behaviour in r appears. When ε is exactly at the critical point the gradient in $V(r)$ is flat, and the fixed point that exists here is half-stable. Figure 6.3 (c) shows that for small ε we would expect the long timescale decay to disappear.

As well as gaining insight into the role that ε has in the transition, the effective potential model shows that initial conditions influence which steady state is found. Lee and Sadeghpour [25] show that after the transition to the synchronised regime, the $|\langle a \rangle| = 0$ solution exists in addition to the $|\langle a \rangle| > 0$ state. The $|\langle a \rangle| = 0$ solution always exists as you can always set

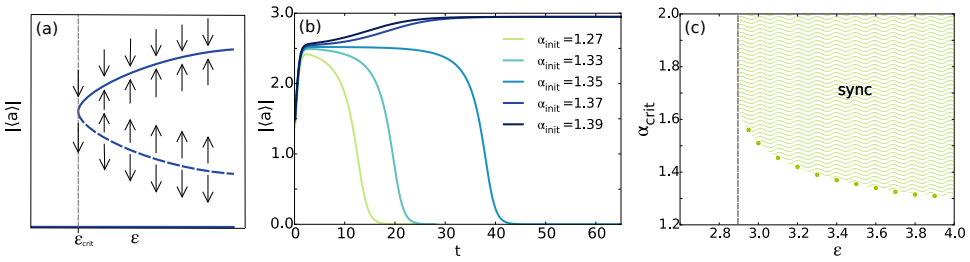


Figure 6.4: (a) An illustration of how the van der Pol system displays a saddle-node bifurcation, with stable (solid) and unstable (dashed) fixed points appearing as ε is increased. (b) The evolution of $|\langle a \rangle|$ at $\varepsilon = 3$ for various values of α_{init} that create the initial state. (c) The critical values of initial conditions (green points), which represent the unstable fixed points. (b) and (c) are for $\kappa_2/\kappa_1 = 0.04$.

the initial condition $\langle a \rangle = 0$, from which no phase preference can develop. However, the $|\langle a \rangle| = 0$ solution for couplings beyond the critical point is not trivial: there exists a true bistability for all couplings above the critical coupling value, as a range of initial conditions can lead to either the synchronised or unsynchronised state. Where the unstable fixed point exists, any value of r not exactly located there moves away from it, towards one of the two stable fixed points. We can therefore locate the position in r of the unstable fixed point by considering a range of initial conditions.

Figure 6.4 shows how the initial conditions affect the evolution of $|\langle a \rangle|$ in time, and the location of the unstable fixed point for different values of coupling[1]. Figure 6.4 (a) illustrates the phase diagram of $|\langle a \rangle|$ and ε, showing one stable state before $\varepsilon_{\text{crit}}$ and two stable, plus one unstable, states after this point. As indicated using the arrows, $|\langle a \rangle|$ flows away from the unstable state towards either the synchronised or unsynchronised states depending on the initial conditions.

In Fig. 6.4 (b) we see the different initial states evolving in time towards one of two stable steady states at a fixed value of ε. Above a critical initial value of α_{init}, all states converge to the synchronised steady state for those partic-

[1]The initial conditions were created by approximating $|\langle a \rangle|$ as the eigenvalue of a coherent state α, so ρ_{init} is in the form of a coherent state density matrix. This is a convenient method for creating a predictable range of initial states; however, other results in this chapter used different choices of initial states, the details of which can be found in Appendix E.2.

ular parameters. Below the critical point all states evolve to the unlocked steady state. We once again see a slow timescale emerging as the gradient of $V(r)$ becomes very shallow as the unstable fixed point is approached. As the coupling strength increases, the basins of attraction for the two stable states varies so that a greater range of initial conditions can lead to a synchronised state (and correspondingly the basin of attraction leading to the unsynchronised state shrinks). Figure 6.4 (c) shows the location of the critical points in α_{init} as a function of ε. The shape of the unstable fixed points' dependence on ε is very reminiscent of the saddle-node bifurcation illustrated in (a), which is generally parabolic close to the transition [126]. At the critical point in ε the unstable fixed point vanishes, leaving only the unsynchronised steady state.

Similar bifurcations have been seen in other nonequilibrium quantum systems [125] in which a mean-field treatment was also used. A prediction of this type of bifurcation is that the timescales of the evolution to the stable fixed points will experience a critical slowing down close to the transition, which we have already seen exists here. The next section explores this phenomenon in detail for the van der Pol oscillator system.

6.1.2 Scaling at the Critical Point

Below the critical coupling, the state will decay to an unsynchronised state in a time that depends on ε and the initial state. However, approaching the critical value of ε there is a slow timescale decay that allows an "almost steady state" to emerge, but which eventually moves into a fast decay to the final unsynchronised steady state. As the coupling strength gets closer to the transition the total decay time increases, and in the saddle-node bifurcation model we would expect a divergence at the transition with the approaching timescales following a power law. Similar power-law scaling close to a critical point has been predicted in a range of quantum systems far from equilibrium [125, 127, 128].

Approaching the transition, the long timescales required to reach the steady state make it difficult to find the critical coupling value precisely. Figure 6.5 plots the time taken for the order parameter $|\langle a \rangle|$ to reach zero (here defined to be $< 5 \times 10^{-3}$) as a function of the coupling strength scaled by the distance from the critical point, $(\varepsilon_{\text{crit}} - \varepsilon)$. Using logarithmic axes it is clear

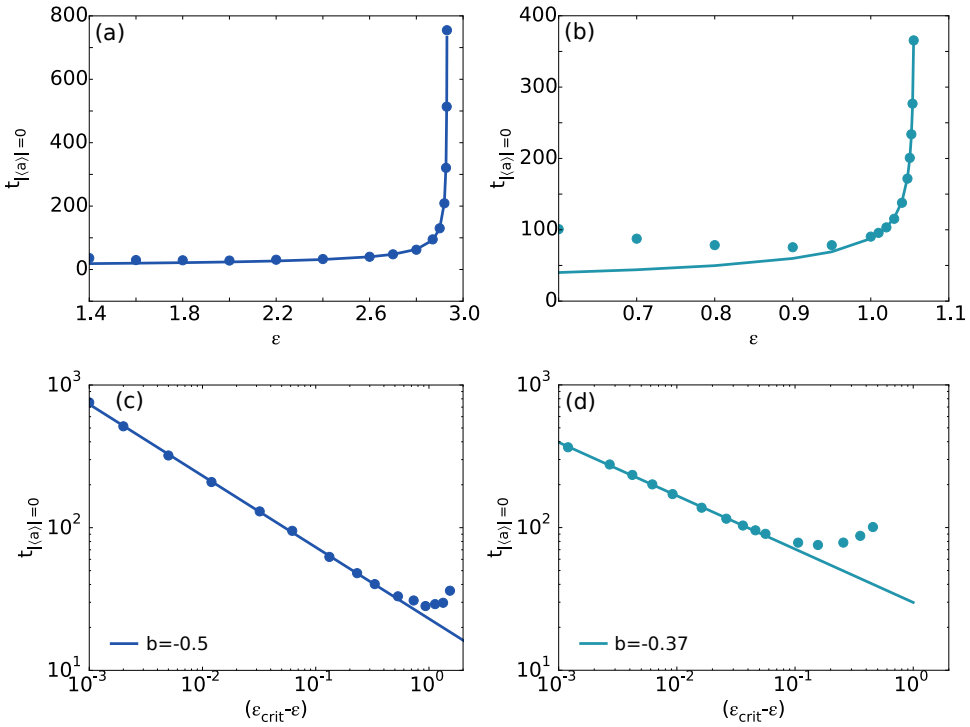


Figure 6.5: Plots of the time taken for $|\langle a\rangle|$ to decay to zero, $t_{|\langle a\rangle|=0}$, for different values of the coupling ε approaching the transition for (a) $\kappa_2/\kappa_1 = 0.04$ and (b) $\kappa_2/\kappa_1 = 0.02$. For (c) and (d) the same data is plotted on logarithmic axes, with the x-axis showing ε in relation to the estimated critical point ε_{crit}. The solid lines are taken from fitting the data points close to the transition.

that as $(\varepsilon_{\text{crit}} - \varepsilon)$ becomes small close to the transition, the timescale divergence does indeed follow a power law. This is demonstrated by the linear relationship on logarithmic axes, following

$$\log(t_{|\langle a\rangle|=0}) = \log(a) + b\log(\varepsilon_{\text{crit}} - \varepsilon) \tag{6.1.4}$$

$$t_{|\langle a\rangle|=0} = a(\varepsilon_{\text{crit}} - \varepsilon)^b. \tag{6.1.5}$$

By adjusting $\varepsilon_{\text{crit}}$ we can find a best fit for the data and extract an estimate of the critical point, and also find the slope of the fitted line to determine the power law exponent b.

Figure 6.5 compares two transitions for the van der Pol oscillator, at $\kappa_2/\kappa_1 = 0.04$ and $\kappa_2/\kappa_1 = 0.02$ (smaller κ_2/κ_1 ratios are closer to the semiclassical limit with larger limit cycles). Though they appear to be very similar, there are differences in behaviour. Most obviously, the fit drops off far more quickly for $\kappa_2/\kappa_1 = 0.02$. When $(\varepsilon_{\text{crit}} - \varepsilon)$ becomes too high the behaviour no longer follows a power law – this corresponds to the decay of $|\langle a\rangle|$ no longer having a slowly evolving part, instead decaying rapidly to zero. It appears that for lower values of κ_2/κ_1, ε is required to be much closer to the transition for the power law behaviour to occur. The slopes of the linear best fit lines are also different. Finding the best fit for the data becomes more accurate when there are more points close to the transition – however, the smaller the quantity $(\varepsilon_{\text{crit}} - \varepsilon)$ is, the more important the precise location of the critical point becomes and errors grow large. The behaviour of $\varepsilon_{\text{crit}}$, the slope, and the distance from $\varepsilon_{\text{crit}}$ that the power law fails can all be used to see how the characteristics of the transition change with the parameters of the system.

The greatest source of error is the value of $\varepsilon_{\text{crit}}$, as this completely changes the shape of the curve that we are trying to fit (an example of this is detailed in Appendix E.3). As we are only able to find $\varepsilon_{\text{crit}}$ with limited accuracy and precision it seems safer to seek an estimate of the slope b over a range. This is something that will be discussed further in Sec. 6.2.2, where a prediction for b based on the saddle-node nature of the bifurcation is also discussed.

6.1.3 Phase and number uncertainties

We have already seen in Fig. 6.2 that there are changes to both the photon numbers and phase during the decay. As number and phase are known

to be conjugate variables a relationship between them would not be surprising, and it is interesting to consider the behaviour of their uncertainties close to the transition to gain a more complete picture.

There are many options for defining phase uncertainty [129], most of which use the phase distribution $P(\varphi)$. In the synchronised steady state for our system, the phase preference oscillates with time despite the phase amplitude (i.e. $|\langle a \rangle|$) remaining constant, meaning that $P(\varphi)$ will also change with time. With this in mind, an appropriate choice for the phase uncertainty is an expression that only relies on the overall shape of the phase distribution, and does not take into account the location of the peak in φ (which will shift with time). A suitable suggestion is the entropic measure of uncertainty [130]

$$\Delta\varphi = -\int_{-\pi}^{\pi} \mathrm{d}\varphi P(\varphi) \ln P(\varphi). \tag{6.1.6}$$

The uncertainty of numbers of photons in a system is usually a straightforward quantity, frequently defined as

$$\Delta n = \sqrt{\langle n^2 \rangle - \langle n \rangle^2}. \tag{6.1.7}$$

Previously in this thesis we have used the Fano factor, a similar quantity but it is scaled by the numbers of photons. For this chapter we shall use another definition, however. A particular advantage of the entropic measure of phase uncertainty is that it can be used in the uncertainty relation [129]

$$-\int_{-\pi}^{\pi} \mathrm{d}\varphi P(\varphi) \ln P(\varphi) - \sum_{n=0}^{\infty} W_n \ln W_n \geq \ln(2\pi), \tag{6.1.8}$$

where W_n are the photon distribution probabilities $W_n = \langle n|\rho_n|n\rangle$. Therefore, in order to explore the relationship between the number and phase uncertainties, we will use the quantity

$$\Delta n = -\sum_{n=0}^{\infty} W_n \ln W_n \tag{6.1.9}$$

to define the uncertainty in the photon number.

Figure 6.6 (a) plots the steady-state values of these uncertainty values Δn and $\Delta\varphi$ along with $|\langle a \rangle|$, $\langle n \rangle$ and $\Delta n + \Delta\varphi - \ln(2\pi)$ as given in Eq. 6.1.8. We know already from Lee and Sadeghpour that the synchronisation order parameter $|\langle a \rangle|$ is zero until the critical value of ε, at which point it becomes

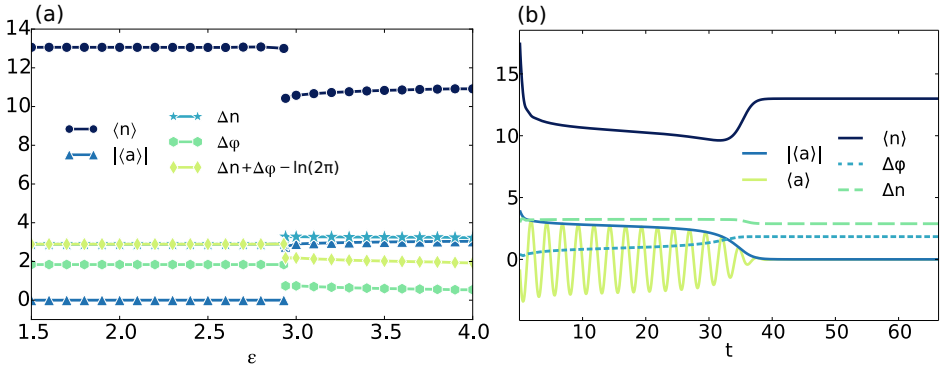


Figure 6.6: (a) The steady state values of some key quantities in the system across the synchronisation transition in ε. (b) An example of how some of these quantities evolve in time below the critical coupling value, in this case $\varepsilon = 2.7$. For both, $\kappa_2/\kappa_1 = 0.04$.

positive indicating partial phase synchronisation. In the unsynchronised state we know that $P(\varphi) = 1/2\pi$ so $\Delta\varphi = \ln(2\pi)$. The phase uncertainty drops at the transition point – this is expected from looking at the Wigner functions, which initially show a circularly symmetric distribution with no phase preference below the transition, then displaying a single peak with a well-defined phase above the transition. As the system becomes synchronised, a phase preference emerges and phase uncertainty drops. The conjugate variable, the average number of photons $\langle n \rangle$, drops significantly at this transition and the uncertainty in n goes up by a small amount. That a rise in photon number uncertainty should accompany a drop in phase uncertainty is expected due to their conjugate relationship, but the uncertainty relation Eq. 6.1.8 always stays well above the limit of $\ln(2\pi)$.

Figure 6.6 (b) shows these quantities evolving with time at $\varepsilon = 2.7$. After initially decaying quickly to find the "almost" steady state, all quantities keep fairly constant until the final fast timescale decay to the unsynchronised state. Interestingly, the average photon number decays downwards, similar to $|\langle a \rangle|$, despite eventually finding a state with a higher average number. $|\langle a \rangle|$ always decays *away* from the synchronised state towards the unsynchronised state; conversely $\langle n \rangle$ decays *towards* the synchronised state, before sharply transitioning to the unlocked steady state.

The next section considers a corresponding mean-field model for micromasers. This allows us to explore the extent to which features seen in the

van der Pol system exist generally, and also investigate how quantum characteristics such as number-squeezing may affect the transition.

6.2 Coupled Micromasers

In the previously studied micromaser systems, changing the value of Θ has yielded extremely different states, some of which have highly quantum properties. The parameter N is strongly linked to the numbers of photons in the system, and by association its classicality.

The same method of using a mean-field approximation of globally coupled oscillators will be used for the micromaser system as for the van der Pol oscillators, with the Hamiltonian

$$H_{\mathrm{mm}} = \varepsilon \left(\langle a \rangle a^{\dagger} + \langle a^{\dagger} \rangle a \right), \tag{6.2.1}$$

and the dissipative Lindblad operators are given in Eqs. 2.2.2–2.2.5. We will be looking at the behaviour of the system as the coupling strength is varied, and initially making a comparison between $N = 20$ and $N = 50$. In previous chapters we have gone as low as $N = 5$ to examine the quantum regime, but here a synchronised state could not be found for limit cycles as small as this. This is most likely due to the existence of a critical size of the limit cycle below which the coupling required for synchronisation diverges, as is seen in the van der Pol system [25]. For both values of N we focus mainly on a value of $\Theta = 2$. As we have seen in Sec. 2.2, N and Θ are interdependent and keeping a constant value of Θ does not guarantee similar states as N is varied. However, for $\Theta = 2$ there are well-defined limit cycles for $N = 20$ and $N = 50$ that are similar enough to be comparable, with the only difference being the relative sizes of them.

6.2.1 State Evolution and Bistability

Figure 6.7 builds a picture of the synchronised and unsynchronised states for the coupled micromasers at $N = 20$ and $N = 50$, both for $\Theta = 2$. The evolution of $|\langle a \rangle|$ over time is similar to the van der Pol oscillator system, with a two-timescale decay rate close to the synchronisation transition. For $N = 20$, the strength of phase synchronisation is lower, and the critical

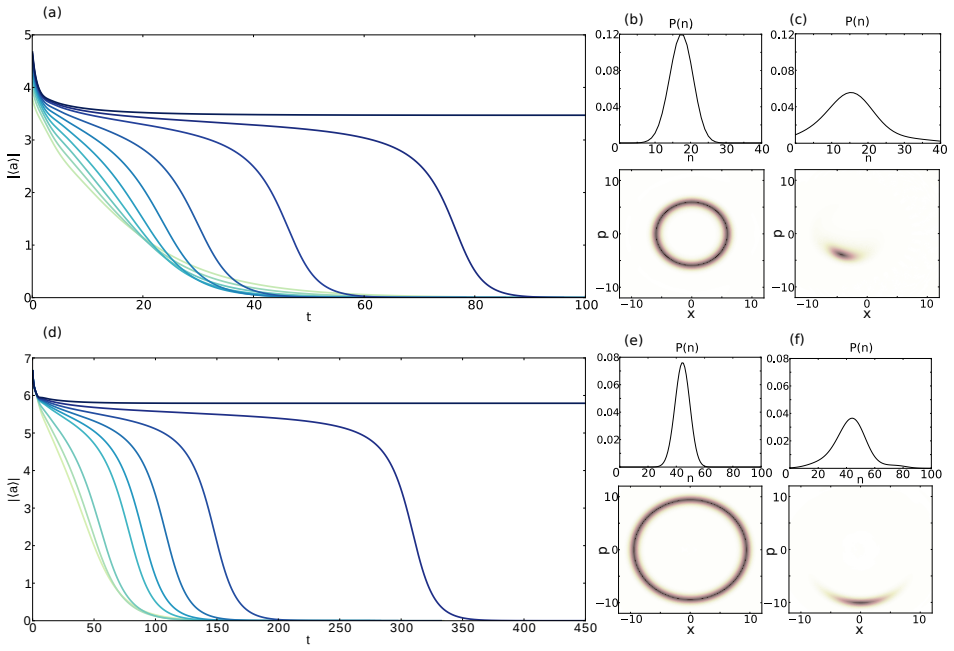


Figure 6.7: The evolution of $|\langle a \rangle|$ with time, for $\Theta = 2$, and a range of coupling values ε up to the locking transition for (a) $N = 20$ ($\varepsilon = 0.5$–1.3), (d) $N = 50$ ($\varepsilon = 0.5$–0.7). In each case the photon number distribution $P(n)$ and the Wigner function are shown for the unlocked state [$\varepsilon = 0$ for (b) and (e)] and the locked state [(c) $\varepsilon = 1.3$, (f) $\varepsilon = 0.7$].

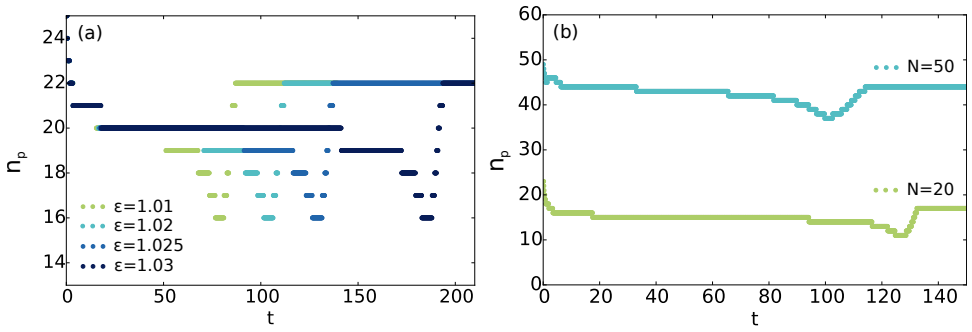


Figure 6.8: (a) Plot of the most probable number of photons (n at which $P(n)$ is peaked) as a function of the time taken to decay into an unsynchronised steady state, with $N = 25$ and $\Theta = 2$. (b) A comparison of the most probable number of photons for $N = 20$, $\varepsilon = 1.27$ and $N = 50$, $\varepsilon = 0.67$ with $\Theta = 2$. For both values of N, $(\varepsilon_{\text{crit}} - \varepsilon) \approx 0.02$.

strength of coupling required for the transition is higher than that for $N = 50$. Looking at the distributions, the limit cycle for $N = 50$ is larger and the photon number distribution peaked at a much higher number of photons. Both values of N for the micromaser systems display similar behaviour to the van der Pol oscillators in that they also have bistable steady states of phase locked/unlocked states after a critical point in the coupling strength, and this appears to occur via a saddle-node bifurcation.

Looking back at the van der Pol oscillator in Fig. 6.2, the peak of the photon probability distribution is always close to zero, and during the decay to the unsynchronised state it actually passes through zero. In this case, the phase information is quickly erased and the decay to the unsynchronised state occurs rapidly. Figure 6.8 shows the location of the peak in $P(n)$, n_p, for many micromasers at different values of coupling strength and N. Figure 6.8 (a) shows that there is always a dip in n_p, which is most pronounced just before the final fast decay to the unsynchronised state, and although ε dictates when in t this occurs, the shape of the dip is always the same. For Fig. 6.8 (b) we look at the two values of N, for which the numbers of photons in the systems are very different. Despite the different average photon number, the behaviour around the fast decay is very similar. It then seems likely that the transition of n_p through zero for the van der Pol oscillator (seen in Fig. 6.2) is a result of the average photon number already being low. Although the behaviour of the decay in Fig 6.8 (b) is similar for both $N = 20$ and $N = 50$, the combination of a slow timescale decay followed

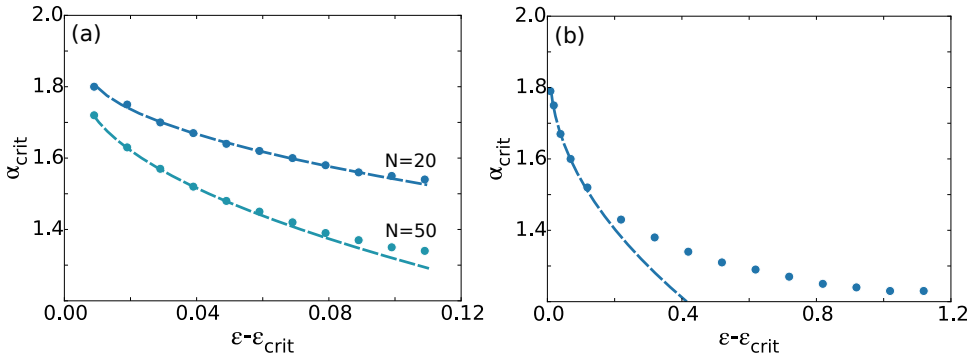


Figure 6.9: The critical value of the initial state α_{crit} plotted as a function of the distance from the critical point in ε for (a) $N = 20$ and $N = 50$, and (b) a larger range for $N = 20$, with $\Theta = 2$. The dashed lines are fits to the points, assuming a parabolic curve that is most accurate for small values of $\varepsilon - \varepsilon_{crit}$.

by a final fast decay appears to be more defined for the lower value of N.

We now explore the boundary of synchronised and unsynchronised phases set by the initial conditions. Figure 6.9 compares the critical point in initial conditions [using the same methods as were used for Fig. 6.4 (b)] for fixed values of ε, plotted as a function of the distance from the transition in ε. On this scale, an approximately parabolic curve can be seen for both values of N. However, from the fitted curves we can see that the parabolic nature of the points exists for a narrower range of $(\varepsilon - \varepsilon_{crit})$ for $N = 50$ than for $N = 20$. This suggests that the critical region is smaller as a function of $(\varepsilon - \varepsilon_{crit})$ for larger photon numbers as was found for the van der Pol system. In Fig. 6.9 (b) as we look further away from the transition for $N = 20$ the change in α_{crit} becomes a lot smaller, and the shape appears to be quite different. This is confirmed when we apply the same fitted curve from (a) to the larger range, and points far from the transition diverge from the initial parabolic behaviour.

6.2.2 Critical Scaling

As with the van der Pol oscillator system, as ε gets closer to the critical point there appears to be power-law scaling for the decay time. Figure 6.10 shows the decay time as a function of ε for $N = 20$ and $N = 50$, with fitted lines estimating the power law exponents. In this case ε_{crit} was chosen to

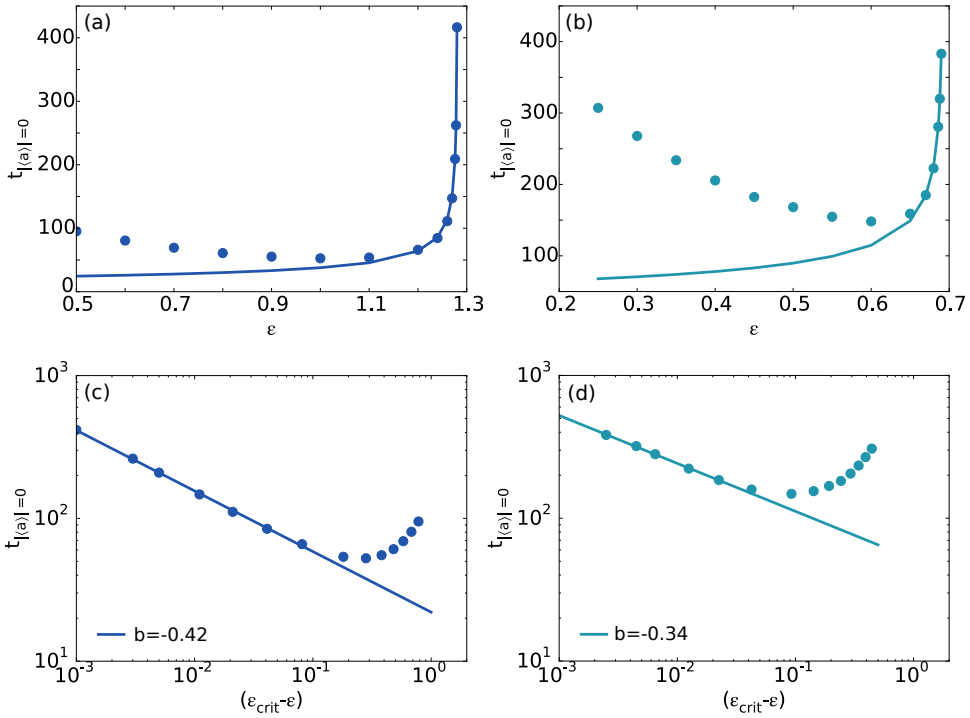


Figure 6.10: Plots of the time taken for $|\langle a\rangle|$ to decay to zero, $t_{|\langle a\rangle|=0}$, for different values of the coupling ε approaching the synchronisation transition for $\Theta = 2$ and (a) $N = 20$ and (b) $N = 50$. For (c) and (d) the same data is plotted on logarithmic axes, with the x-axis showing ε in relation to the estimated critical point $\varepsilon_{\text{crit}}$. The solid lines are taken from fitting the data points close to the transition.

find the best linear fit with the available data. Analysed in this way, the difference in the behaviour is similar to the van der Pol system – in each case the more classical system ($\kappa_2/\kappa_1 = 0.02$, $N = 50$) has a shallower slope and the power-law scaling occurs within a narrower range of $(\varepsilon_{\text{crit}} - \varepsilon)$.

When we consider this scaling in the context of the saddle-node bifurcation of fixed points we can make a prediction of b close to the transition [126]. Saddle-node bifurcations experience a critical slowing down of timescales as the transition is approached from below the critical value. This is due to a "bottleneck" remnant that appears after the stable and unstable fixed points have come together and annihilated, and decreases with distance from the transition.

Consider the approximate equation of motion for the effective potential model Eq. 6.1.3, $\dot{\nu} = \delta + \nu^2$, which is valid just below the transition. Focussing close to the bifurcation $\nu = (r - r_{\text{crit}})$ and $\delta = (\varepsilon_{\text{crit}} - \varepsilon)$ are small, with r_{crit} the location at which the unstable and stable fixed points merge. Following [126], the time taken to get through the slowly-evolving timescale is

$$\tau \approx \int_{-\infty}^{\infty} \frac{\mathrm{d}\nu}{\dot{\nu}} = \int_{-\infty}^{\infty} \frac{\mathrm{d}\nu}{\delta + \nu^2} = \frac{\pi}{\sqrt{\delta}}. \tag{6.2.2}$$

A critical exponent of $b = -0.5$ is a general result due to the fact that $\dot{\nu}$ will always have a ν^2 dependence at small values of δ for this type of bifurcation, something that can be demonstrated by using Taylor expansions for more complex effective potential functions (constants that account for other parameters in the system do not affect the overall form). This means that the result τ is approximately proportional to $\delta^{-0.5}$ is universal for this type of transition regardless of the parameter space, however this appears to be contrary to what we have found in Figs. 6.5 and 6.10 where the exponent seems to depend on the parameters of the system. To understand this discrepancy, we will need to look in more detail across a range of parameters and look at the impact of potential numerical errors very carefully.

For the micromaser system we are restricted to approximately the N =20–50 range, but by looking at different values in this range we can build up a picture of the behaviour with N. Figure 6.11 shows (a) the critical coupling value and (b) the power law exponent as a function of $1/N$. There is a clear trend in the critical values of ε across $1/N$, and despite the limited range there is the beginnings of a convergence as $1/N$ becomes small. Likewise,

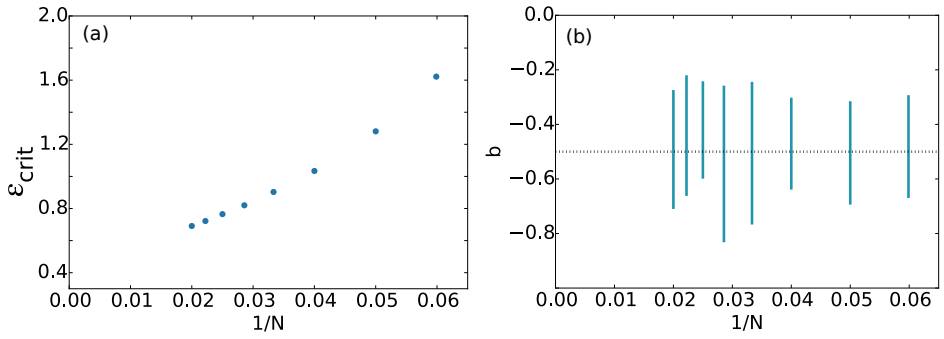


Figure 6.11: (a) The critical value of coupling ε and (b) a predicted range for the slope that determines the power law exponent, plotted against $1/N$ for $\Theta = 2$. The semiclassical limit is approached as $1/N \to 0$. The method for creating the range in uncertainty is detailed in Appendix E.3, and for (a) the error bars are smaller than the marker size.

as it becomes large the critical coupling begins to diverge as the limit cycle is smaller. Both these features also appear for the van der Pol oscillator as κ_2/κ_1 is varied [25]. In Fig. 6.11 (b) the behaviour of the critical component b is much less clear, with large errors making it difficult to identify a trend. Due to the high sensitivity of b to various factors, it seems appropriate to define upper and lower bounds to b. A careful analysis and explanation of the errors involved are given in Appendix E.3. This range in b, although quite large, includes the mean-field prediction of $b = -0.5$ for all values of N.

6.2.3 Properties of the Transition in Parameter Space

Figure 6.12 shows how a selection of other observables behave at the transition for $N = 20$ and $N = 50$, with (a) and (b) looking at the steady state and (c) and (d) showing an example decay to the unsynchronised state. Here, we also include the von Neumann entropy S – defined in Sec. 5.3.1 – to see how this behaves around the transition. The difference between Fig. 6.12 (a) and (b) is most noticeable for the average photon number $\langle n \rangle$, which is much higher for $N = 50$. The higher photon number is also linked to a higher $|\langle a \rangle|$ in the synchronised state for $N = 50$. However, the other quantities are for the most part extremely similar. Due to the density op-

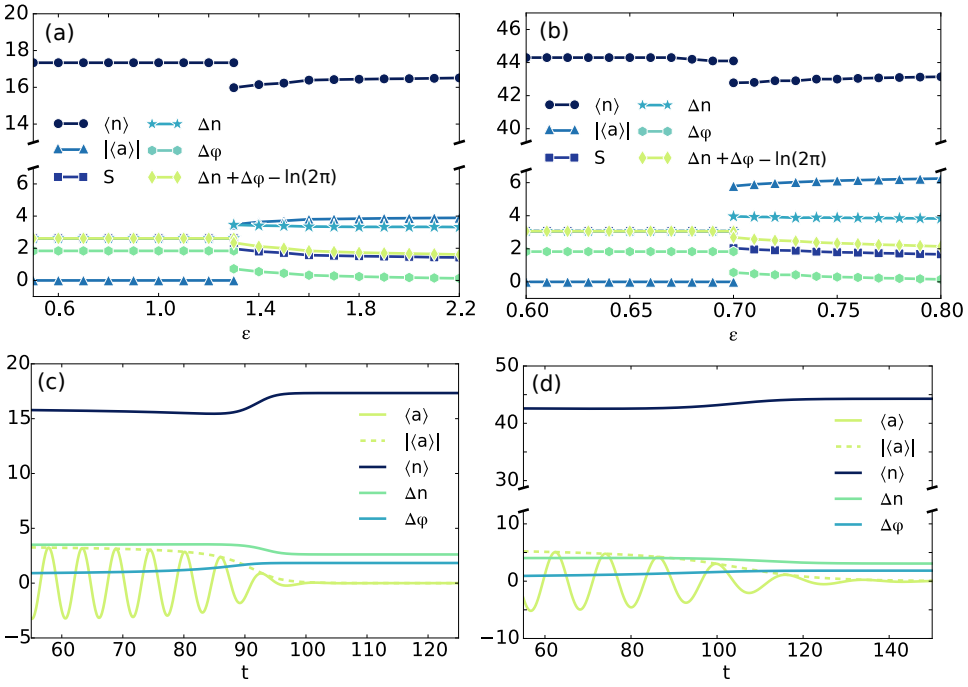


Figure 6.12: The steady-state values of some key quantities, and their uncertainties, in the micromaser systems as they transition to a synchronised regime in ε for $\Theta = 2$. Below are example evolutions of the decay to an unsynchronised state. (a), (c) $N = 20$ and (b), (d) $N = 50$. For (c) and (d) $(\varepsilon_{\text{crit}} - \varepsilon) \simeq 0.02$.

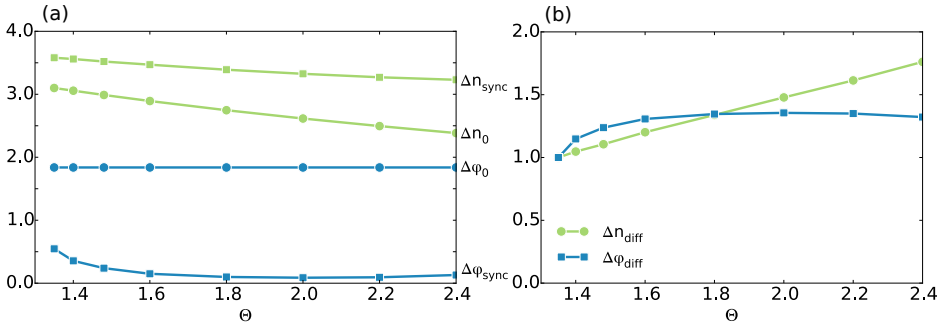


Figure 6.13: (a) Comparing the uncertainties in number and phase for the unsynchronised $(\Delta n_0, \Delta\varphi_0)$ and synchronised $(\Delta n_{\text{sync}}, \Delta\varphi_{\text{sync}})$ states as a function of Θ. For each value of Θ, the ε value used for the synchronised state is double the value of $\varepsilon_{\text{crit}}$ for that Θ. (b) The difference between the synchronised and unsynchronised states for Δn and $\Delta\varphi$, plotted as the relative change from the first value at $\Theta = 1.35$. Here, $N = 20$ throughout.

erator being diagonal in the unsynchronised state we find that $\Delta n = S$ in this region, in addition to $\Delta\varphi = \ln(2\pi)$. As with the van der Pol oscillator, the average photon number decreases and its uncertainty increases slightly for both micromaser systems when they are phase synchronised. Also as before, when a phase preference arises for the system the phase uncertainty decreases significantly. Although Δn always increases whilst $\Delta\varphi$ decreases at the transition, there is an overall drop in both S and $\Delta n + \Delta\varphi$; the uncertainty limit $\Delta n + \Delta\varphi = \ln(2\pi)$ is not approached in either case, however. Figures 6.12 (c) and (d) show the decay in both micromaser systems at the same proportional distance from the critical point in ε. They are both quite similar, showing that the evolution to the steady state depends more on the values of ε and $\varepsilon_{\text{crit}}$ than N or Θ. However, the transition to the unsynchronised state is much less pronounced for $N = 50$ than it is for $N = 20$, particularly for $\langle n \rangle$ – the jump in $\langle n \rangle$ does not seem to grow in proportion to N.

We now look to see how the value of Θ affects the behaviour of the phase and number uncertainties for fixed N. Figure 6.13 shows that there is always a jump in phase and number uncertainties before and after the transition. As Θ increases, we can see that both the unsynchronised and synchronised states have less number uncertainty (see Fig. 2.4). The rate at which the uncertainty drops is different for each one however, and the size

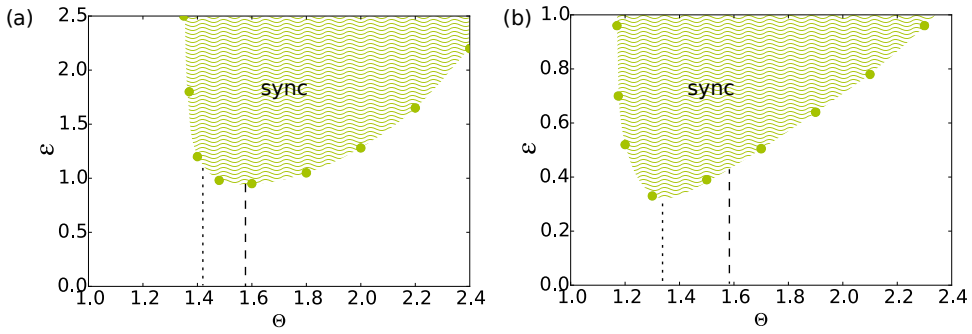


Figure 6.14: A map of how Θ affects the critical transition point in ε for (a) $N = 20$ and (b) $N = 50$. The dashed lines indicate the maximum in $\langle n \rangle$ and the dotted lines indicate the minimum in the linewidth.

of the jump increases steadily with Θ. For the phase uncertainty, the unsynchronised state is at a maximum for all parameters. The synchronised state jumps to a much lower value that is approximately the same for most of the range of Θ that we looked at. However, the phase uncertainty in the synchronised state increases slightly for smaller values of Θ where the limit cycle becomes smaller and less well-defined as the threshold is approached towards $\Theta = 1$.

We have seen that there is a substantial difference in the critical value of ε when N is varied. As N and Θ are related, a relationship between Θ and the critical value of ε would also be expected. Figure 6.14 maps out this relationship for (a) $N = 20$ and (b) $N = 50$. The shaded region indicates where phase synchronisation exists in the steady state. The maps for both values of N are similar, with the value of Θ at which the minimum ε occurs being approximately the same. The coupling strength required for synchronisation increases extremely rapidly as Θ moves towards the threshold value of $\Theta = 1$, and also increases as Θ gets larger. The critical value of ε required for synchronisation is in general much larger for $N = 20$ than $N = 50$. This – combined with the shape of the dependence of ε on Θ – implies a relationship with the number of photons in the cavity, where the higher the average photon number the less coupling is required to reach synchronisation. However, the relationship is not quite so simple as the peaks in $\langle n \rangle$ do not exactly correspond to the minima in $\varepsilon_{\text{crit}}$. The locations in Θ for the $\langle n \rangle$ peaks are very similar, whereas the minima in Fig. 6.14 are somewhat different for the two values of N. Likewise, the minimum linewidth in Θ for an undriven micromaser is a very good match for $N = 50$ [see also Fig. 4.4

(b)], but much less so for $N = 20$.

6.3 Summary and Conclusions

This chapter looked at synchronisation for many oscillators with all-to-all coupling, both for the van der Pol oscillator and the micromaser. Both systems exhibited similar dynamics, with a stable unsynchronised state existing for all values of coupling with an additional pair of stable/unstable synchronised states appearing spontaneously above a critical value of coupling that depended on the system parameters. Though the location of the transition could vary, the nature of the bifurcation and critical dynamics was found to be the same for both of the systems studied, and independent from the system parameters.

Above the critical coupling strength there exists a synchronised steady state with a constant value of the order parameter $|\langle a \rangle|$ but a time-dependent oscillating phase. The nature of the decay to an unsynchronised state depends on the value of the coupling and initial conditions. For weak coupling, the evolution of $|\langle a \rangle|$ to the unlocked state is a fast decay. As the coupling nears the critical point, this decay develops a slow timescale decay in addition to a final fast decay. During this slow timescale decay the state behaves as though it is almost in the synchronised steady state, with a rotating preferred phase. The closer to the critical point, the slower the decay, and the longer it takes for the fast decay to occur, until at the critical point there is a transition and the synchronised state becomes stable. This is consistent with a saddle-node bifurcation description and has been noted in similar systems [125]. The decay timescale follows a power law, and a prediction of the critical exponent to be $b = -0.5$ was consistent with numerical results for both systems. There was difficulty in obtaining precise results due to the long relaxation times close to the transition. However, it became clear that the critical region got smaller with larger photon numbers.

We also looked in detail at the final fast decay to the unsynchronised state. We found that photon numbers always seemed to drop before rising rapidly to the final higher value of the unsynchronised state in a "latching" type behaviour. This is in contrast to the phase, which always decays towards its final steady state, never away from it. This behaviour was reflected in the

peak in the $P(n)$ distribution, which always dropped initially before finally rising during the final stage of the decay. For smaller limit cycles in the van der Pol oscillator system, the peak reaches zero facilitating the rapid loss of phase information. For larger limit cycles it does not necessarily pass through zero, but does always dip.

Comparing the properties of the unsynchronised and synchronised steady states, there were changes in many quantities other than the phase. The photon number always dropped as the system became phase locked. The significant change in $\langle n \rangle$ could provide a simple way to detect the location of the transition in an experiment. When looking at the phase and number uncertainties, the phase uncertainty dropped (as expected when moving from no preferred phase to a synchronised state) while the number uncertainty grew. Since the number and phase are canonical variables, this relationship is not surprising; however, the value of the entropic uncertainty relation always stayed well above the bound of $\ln(2\pi)$. For the micromaser system, jumps in uncertainty for number and phase were also examined over a range of Θ. As Θ grew larger, the unsynchronised system became more number squeezed and the jump in Δn became stronger. The unordered phase always had a maximum uncertainty value, but the synchronised value of $\Delta\varphi$ was fairly constantly small – the exception being for low values of Θ (approaching the threshold) where it became larger.

When looking at the difference in the two steady states for different values of N for the micromaser system, there was a large difference in photon numbers but little difference for the phase, uncertainties or entropy. A map of the approximate synchronised regions over Θ for $N = 20$ and $N = 50$ was also created. The shape suggests that the number of photons may influence the synchronised regions in some way, but the picture is likely not a very simple one as the minima in these maps do not exactly correspond to the maxima in $\langle n \rangle$ or minima in linewidths.

6.4 Future Directions

Potential future expansions of this work could take several directions. It would be worthwhile to attempt to expand the parameter space for the micromaser, both in N and Θ. As N increases it would be interesting to see if

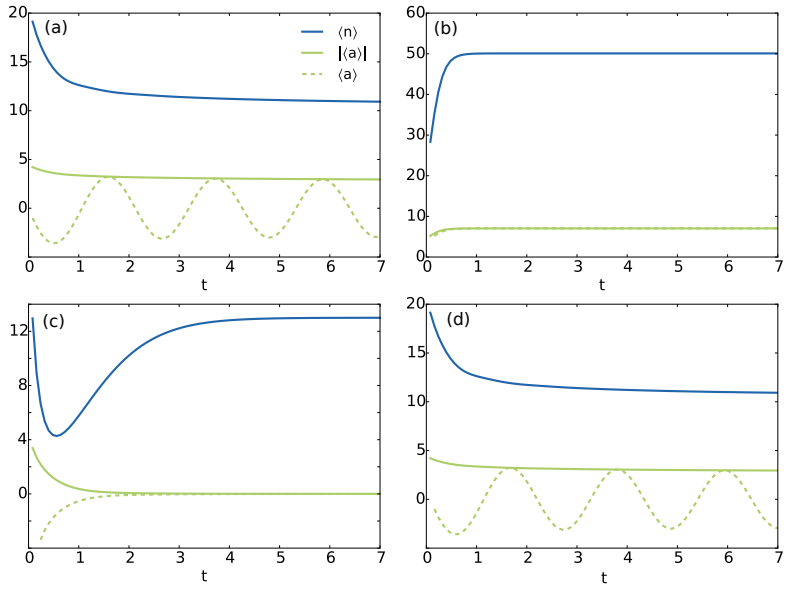


Figure 6.15: The evolution over time of the vdP oscillator for (a) $\psi = 0$, (b) $\psi = \pi/2$, (c) $\psi = 3\pi/2$, and (d) $\psi = \pi$ with $\kappa_2/\kappa_1 = 0.04$.

quantities such as $\varepsilon_{\text{crit}}$ converge. From Fig. 6.11 we can see the beginnings of a convergence for the critical coupling, but exploring higher values of N would give us a much more accurate description. In the classical van der Pol system, as noise approaches zero so does the coupling strength threshold required for synchronisation [25]. A more detailed look into how the quantum van der Pol oscillator and micromaser systems act for quantum noise that is relatively weak could give insight as to whether they behave similarly to each other or their respective classical analogues. Being able to access more diverse states in Θ could also be very interesting. For example, the trapping state locations in Θ were explored for the micromaser system, but no synchronisation could be found here for the ranges of coupling that were attempted (up to $\varepsilon = 6$ with two trapping state locations for $N = 20$). These can be highly number-squeezed states that are very sensitive to coupling in the other micromaser systems looked at in this thesis, so it would be informative to explore this further and see whether it is the nature of the trapping state or some other reason this region is more resistant to synchronisation for all-to-all coupling. For certain values of Θ bistabilities develop with two coexisting limit cycles, and it is not clear how a transition to synchronisation would occur here.

One notable feature of the synchronised steady state for both the van der Pol oscillator and the micromaser is that the phase preference changes periodically in time. The periodicity of these oscillations appears to depend on the coupling strength (see Fig. 6.1). We could investigate this further by generalising the coherent coupling to introduce a phase, for example

$$H = \varepsilon \left(\langle a^\dagger \rangle a \, \mathrm{e}^{i\psi} + \langle a \rangle a^\dagger \, \mathrm{e}^{-i\psi} \right). \tag{6.4.1}$$

Figure 6.15 shows the effect of different choices of ψ for the coupling. Both (a) and (d) both show results for real values of coupling, each with a different sign, and $\langle a \rangle$ oscillates as we have seen throughout this chapter. The values of $\langle n \rangle$, $\langle a \rangle$ and $|\langle a \rangle|$ are the same despite the change in sign. With different choices of phase, Fig. 6.15 (b) and (c) have non-oscillating values of $\langle a \rangle$ that match the corresponding value of $|\langle a \rangle|$ in the steady state. However, the initial conditions seem to have an impact on the value of the steady states, and each one differs to the steady state found with real coupling values. An investigation into why this occurs and what implications it has could be informative. Additionally, different forms of coupling such as dissipative coupling could be studied.

As well as varying the form of coupling, more complex mean-field models of oscillators may be considered. Plaquette or cluster models consisting of more than one oscillator, similar to what is considered in Ref. [131], could expand on this work. Mean-field models have been used in other many-body quantum oscillator systems [17, 26, 120, 121, 125, 132]. Recent alternative approaches such as matrix product methods have been used to show that accounting for short-range correlations can produce quite different behaviour, however [131, 133]. As noted in Sec. 6.1, proposals have been made for all-to-all coupling for large numbers of superconducting resonators [123], with realisable quantum circuits with similar (adjustable) properties also being proposed [134, 135], suggesting that mean-field models can now have a way to be tested.

Appendices

Appendix A

Semiclassical approximations for a single driven micromaser

A.1 On-resonance calculation of the phase diffusion constant

Working through the calculations made in Ref. [54] we begin by relating the evolution of $\langle a^\dagger \rangle$ in time to the off-diagonal elements of the density matrix by

$$\langle a^\dagger(t) \rangle = \sum_n \sqrt{n+1}\rho_{n,n+1}(t). \tag{A.1.1}$$

The master equation is written in the form given in Eq. 4.1.11. In this form we can see how transitions between photon states in the density matrix occur (Fig. A.1). Assuming that the detailed balance conditions that lead to a steady state in the diagonal elements also apply to the off-diagonal ones, we look to the long-time limit to obtain the approximate phase diffusion constant. We can create a detailed balance equation by looking at the individual processes and transitions as the master equation evolves and finding which ones would need to be equal in the steady state. For this system

$$c_n \rho_n^{(k)} = d_{n+1} \rho_{n+1}^{(k)} \tag{A.1.2}$$

$$c_{n-1} \rho_{n-1}^{(k)} = d_n \rho_n^{(k)} \tag{A.1.3}$$

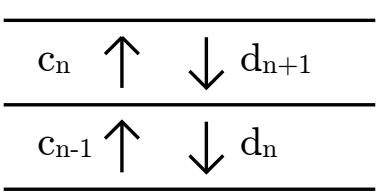


Figure A.1: Visualising the evolution of the density matrix in terms of the individual processes from Eq. 4.1.11 to understand the conditions needed for detailed balance in this system.

would need to be true to satisfy detailed balance. From the above conditions,

$$\rho_n^{(k)}(t) = \prod_{m=1}^{n} \frac{c_{m-1}}{d_m} \rho_0^{(k)}(t). \tag{A.1.4}$$

Now we can suggest the ansatz

$$\rho_n^{(k)}(t) = \mathrm{e}^{-D_n(t)} \rho_n^{(k)}(0) \tag{A.1.5}$$

to describe the time evolution of the density matrix, where $D_n(t)$, an as yet uncalculated function, controls the timescale of this evolution. From this, it follows that

$$\rho_n^{(k)}(t) = \mathrm{e}^{-D_n(t)} \prod_{m=1}^{n} \frac{c_{m-1}}{d_m} \rho_0^{(k)}(0) \tag{A.1.6}$$

$$\rho_{n+1}^{(k)}(t) = \mathrm{e}^{-(D_{n+1}-D_n)} \frac{c_n}{d_{n+1}} \rho_n^{(k)}(t) \tag{A.1.7}$$

$$\rho_{n-1}^{(k)}(t) = \mathrm{e}^{-(D_{n-1}-D_n)} \frac{d_n}{c_{n-1}} \rho_n^{(k)}(t) \tag{A.1.8}$$

and that

$$\dot{\rho}_n^{(k)}(t) = -\dot{D}_n \rho_n^{(k)}(t). \tag{A.1.9}$$

Now we can find an expression for $\dot{D}_n$:

$$\dot{D}_n = \frac{\mu_n(k)}{2} + c_n \left(1 - \mathrm{e}^{-(D_{n+1}-D_n)}\right) + d_n \left(1 - \mathrm{e}^{-(D_{n-1}-D_n)}\right). \tag{A.1.10}$$

Assuming $D_n(t)$ is a slowly changing function of n, so that $|D_n^{(k)} - D_{n-1}^{(k)}| \ll 1$, we can expand the exponentials, drop the small terms, and find [54]

$$\dot{D}_n(t) \simeq \frac{\mu_n(k)}{2} \;\Rightarrow\; D_n(t) \simeq \frac{\mu_n(k)t}{2}. \tag{A.1.11}$$

Thus our assumption is equivalent to

$$\frac{1}{2}|\mu_n(k) - \mu_{n-1}(k)|t \;\simeq\; \frac{1}{2}\left|\frac{\partial \mu_n(k)}{\partial n}\right| t \ll 1, \tag{A.1.12}$$

which holds true when $\mu_n(t)$ changes very slowly with n. Now using this in Eq. A.1.9 with $k = 1$

$$\rho_n^{(1)}(t) = \simeq \mathrm{e}^{-\frac{1}{2}\mu_n(k=1)t}\rho_n^{(1)}(0). \tag{A.1.13}$$

If we assume that the distribution over n states is strongly peaked at a certain value (not changing with time) then we can replace

$$\mu_n(k=1) \longrightarrow \mu_{\langle n\rangle}(k=1) \tag{A.1.14}$$

so that

$$\langle a^\dagger(t)\rangle = \mathrm{e}^{-\bar{D}t/2}\langle a^\dagger(0)\rangle \tag{A.1.15}$$

which means $\bar{D}$ becomes the expression given in Eq. 4.1.16.

A.2 Off-resonance

A.2.1 Analytic Frequency Calculation

Continuing to use the simple phase diffusion picture, we can use the Fokker-Planck equation (3.1.4) to calculate the average rate of phase evolution. Then using Eq. 4.1.5 (this time keeping the Δ term to include off-resonance regions) we can find an analytic expression of the common frequency of the system, ω_c.

Following Ref. [2], the frequency at which the phase now evolves on average (in a non-rotating frame) is Eq. 4.2.1 for which we require $\omega_\varphi = \langle\dot{\varphi}\rangle$, the average rate of phase evolution. We can rewrite the Fokker-Planck equation as

$$\frac{\partial P}{\partial t} + \frac{\partial F}{\partial \varphi} = 0 \tag{A.2.1}$$

where

$$F = -P\frac{\partial V}{\partial \varphi} - \bar{D}\frac{\partial P}{\partial \varphi} \tag{A.2.2}$$

and

$$-\frac{\partial V}{\partial \varphi} = -\Delta - \frac{\varepsilon}{\sqrt{\langle n\rangle}}\cos\varphi. \tag{A.2.3}$$

Using the knowledge that $P(\varphi)$ is 2π-periodic, we have

$$\omega_\varphi = \left\langle -\frac{\partial V}{\partial \varphi} \right\rangle \tag{A.2.4}$$

$$= \int_0^{2\pi} \frac{\partial V}{\partial \varphi} P(\varphi)\, \mathrm{d}\varphi = \int_0^{2\pi} \left(-P\frac{\partial V}{\partial \varphi} - \bar{D}\frac{\partial P}{\partial \varphi} \right) \mathrm{d}\varphi \tag{A.2.5}$$

$$= \int_0^{2\pi} F\, \mathrm{d}\varphi. \tag{A.2.6}$$

In the steady state

$$\frac{\partial P}{\partial t} = -\frac{\partial F}{\partial \varphi} = 0 \tag{A.2.7}$$

so F is independent of φ, and we have

$$\omega_\varphi = 2\pi F. \tag{A.2.8}$$

Again, making use of the fact that $P(\varphi)$ is a periodic function, we can write it as a Fourier series

$$P(\varphi) = \sum_{n=-\infty}^{\infty} P_n \mathrm{e}^{in\varphi}. \tag{A.2.9}$$

Substituting Eq. A.2.9 into the Fokker-Planck equation (3.1.4) and simplifying, we get

$$F\,\delta_{n,0} = -(\Delta + in\bar{D})P_n - \frac{\varepsilon}{2\sqrt{\langle n \rangle}}(P_{n-1} + P_{n+1}). \tag{A.2.10}$$

First we consider the case where $n > 0$, $\delta_{n\neq 0} = 0$ to get

$$-f(n)P_n = P_{n-1} + P_{n+1} \tag{A.2.11}$$

where $f(n) = -\frac{2\sqrt{\langle n \rangle}}{\varepsilon}(\Delta + in\bar{D})$. For the $n = 0$ case,

$$F = -\Delta P_0 - \frac{\varepsilon}{\sqrt{\langle n \rangle}}(P_{-1} + P_1). \tag{A.2.12}$$

Using normalisation and the fact that $P(\varphi)$ is real and periodic we can say $P_0 = 1/2\pi$ and $P_1 = P_{-1}$, $P_1 + P_{-1} = P_1 + P_1^* = 2\,\mathrm{Re}[P_1]$, and finally obtain

$$\omega_\varphi = 2\pi F = -\Delta - \frac{2\pi\varepsilon}{\sqrt{\langle n \rangle}}\mathrm{Re}[P_1]. \tag{A.2.13}$$

and from this we obtain the common frequency by

$$\omega_c = \omega_d + \omega_\varphi. \tag{A.2.14}$$

To obtain the value of P_1 we can solve the iterative equation Eq. A.2.11 numerically, to a sufficiently large value of n.

A.2.2 Generalisation of the semiclassical phase distribution

To generalise the semiclassical phase distribution description to non-zero values of Δ we begin with the same Fokker-Planck description as before, but this time with the addition of the Δ terms. We require a solution to Eq. 4.2.3. Following [98], let $W = \mathrm{e}^{-\tilde{D}\varphi+\tilde{D}_s\sin\varphi}P(\varphi)$ so that

$$\frac{dW}{d\varphi} = \mathrm{e}^{-\tilde{D}\varphi+\tilde{D}_s\sin\varphi}C_1P(\varphi) \tag{A.2.15}$$

where $C_1 = \frac{\mathrm{d}P}{\mathrm{d}\varphi} - (\tilde{D} - \tilde{D}_s\cos\varphi)P(\varphi)$ is a constant. Rewriting with a new phase variable ψ and integrating between an arbitrary lower value $\psi = C_2$ and upper value $W(\varphi)$ gives

$$W(\varphi) - W(C_2) = C_1\int_{C_2}^{\varphi}\mathrm{e}^{-\tilde{D}\psi+\tilde{D}_s\sin\psi}\,\mathrm{d}\psi. \tag{A.2.16}$$

Dropping the constant on the left hand side (as one will already be generated on the right), and substituting back into $P(\varphi)$ results in

$$P(\varphi) = C_1\mathrm{e}^{\tilde{D}\varphi-\tilde{D}_s\sin\varphi}\int_{C_2}^{\varphi}\mathrm{e}^{-\tilde{D}\psi+\tilde{D}_s\sin\psi}\,\mathrm{d}\psi. \tag{A.2.17}$$

To be a valid description of the phase distribution this solution needs to obey the rules

$$P(\varphi) = P(\varphi+2\pi) \tag{A.2.18}$$

$$\int_0^{2\pi}P(\varphi)\,\mathrm{d}\varphi = 1. \tag{A.2.19}$$

For the first, the solution needing to be 2π-periodic, we set $C_2 = -\infty$ and replace $\varphi \to \varphi + 2\pi$ to find that it indeed satisfies this condition. To satisfy the second condition, we must find a constant so that the solution normalises to 1. We can rewrite A.2.17 as

$$P(\varphi) = C_1\mathrm{e}^{2\pi\tilde{D}}\mathrm{e}^{\tilde{D}\varphi-\tilde{D}_s\sin\varphi}Q\int_{\varphi}^{\varphi+2\pi}\mathrm{e}^{-\tilde{D}\psi+\tilde{D}_s\sin\psi}\,\mathrm{d}\psi, \tag{A.2.20}$$

where $Q = 1 + \mathrm{e}^{2\pi\tilde{D}} + \mathrm{e}^{2(2\pi\tilde{D})} + \cdots$ takes the form of a geometric series, which for the condition $|2\pi\tilde{D}| < 1$ has the solution $Q = (1 - \mathrm{e}^{2\pi\tilde{D}})^{-1}$. We can now group these terms together as a normalisation constant N

$$P(\varphi) = \frac{1}{N}\mathrm{e}^{\tilde{D}\varphi-\tilde{D}_s\sin\varphi}\int_{\varphi}^{\varphi+2\pi}\mathrm{e}^{-\tilde{D}\psi+\tilde{D}_s\sin\psi}\,\mathrm{d}\psi. \tag{A.2.21}$$

where $N = -\frac{1-e^{-2\pi\tilde{D}}}{C_1}$. Using Eq. A.2.19 we can now evaluate N. With a change of variables so that $\chi = \psi - \varphi$ we can write

$$\begin{aligned} N &= \int_0^{2\pi} d\varphi \int_0^{2\pi} d\chi \, e^{-\tilde{D}\chi} e^{-\tilde{D}_s[\sin\varphi - \sin(\chi+\varphi)]} \\ &= \int_0^{2\pi} d\varphi \int_0^{2\pi} d\chi \, e^{-\tilde{D}\chi} e^{2\tilde{D}_s \cos(\varphi+\frac{\chi}{2})\sin(\frac{\chi}{2})}, \end{aligned} \tag{A.2.22}$$

where the final line uses the identity $\sin(A+B) - \sin(A-B) = 2\cos A \sin B$. We can say that

$$\int_0^{2\pi} e^{X\cos(\varphi+\frac{\chi}{2})}\, d\varphi = \int_{\psi_1}^{\psi_2} e^{2X\cos(\psi-\frac{\pi}{2})}\, d\psi = \int_{\psi_1}^{\psi_2} e^{2X\sin\psi}\, d\psi = 2\pi I_0(2X), \tag{A.2.23}$$

where $X = \tilde{D}_s \sin(\frac{\chi}{2})$, we have had another change of variables so that $\psi = \varphi + \frac{\chi}{2} + \pi/2$ and we are still integrating between $\varphi_1 = 0$ and $\varphi_2 = 2\pi$. The remaining integral can be split, so that

$$N = 2\pi \left[\int_0^{\pi} e^{-\tilde{D}\chi} I_0\left(2\tilde{D}_s \sin(\chi/2)\right) + \int_{\pi}^{2\pi} e^{-\tilde{D}\chi} I_0\left(2\tilde{D}_s \sin(\chi/2)\right) \right]. \tag{A.2.24}$$

With a final change of variables $\chi = \pi - 2y$ ($d\chi = -2y$) we can rewrite the integral as [136]

$$N = 8\pi e^{-\tilde{D}\pi} \int_0^{\frac{\pi}{2}} \cosh(2\tilde{D}y) I_0(2\tilde{D}_s \cos y)\, dy \tag{A.2.25}$$

$$= 4\pi^2 e^{-\pi\tilde{D}} I_{-i\tilde{D}}(\tilde{D}_s) I_{i\tilde{D}}(\tilde{D}_s). \tag{A.2.26}$$

We can now put this normalisation constant back into Eq. A.2.21 to obtain the phase probability density distribution for non-zero Δ.

Appendix B

Perturbation theory for a single driven micromaser

B.1 Full perturbation theory

We begin with the master equation for a single undriven micromaser in the form given in Eq. 4.1.11, with $\rho_n^{(k)} \equiv \langle n|\rho|n+k\rangle$. To this we can add new terms that arise when we introduce a coherent drive ε

$$\dot{\rho}_n^{(k)} = -i\varepsilon\left[\sqrt{n+1}\,\rho_{n+1}^{(k-1)} + \sqrt{n}\,\rho_{n-1}^{(k+1)} - \sqrt{n+k}\,\rho_n^{(k-1)} - \sqrt{n+k+1}\,\rho_n^{(k+1)}\right]. \tag{B.1.1}$$

When k and ε are sufficiently small, we can use a perturbation theory to lowest order, i.e. we will only consider $k = 0, \pm 1$. Adding Eq. B.1.1 to Eq. 4.1.11 for $k = 1$ gives

$$\begin{aligned}\dot{\rho}_n^{(1)} = &-\frac{\mu_n(1)}{2}\rho_n^{(1)} - c_n^{(1)}\rho_n^{(1)} - d_n^{(1)}\rho_n^{(1)} \\ &+ c_{n-1}^{(1)}\rho_{n-1}^{(1)} + d_{n+1}^{(1)}\rho_{n+1}^{(1)} \\ &- i\varepsilon\left[\sqrt{n+1}(\rho_{n+1}^{(0)} - \rho_n^{(0)})\right],\end{aligned} \tag{B.1.2}$$

with a similar expression for $k = -1$. Our first option is to solve this numerically. We can construct a tridiagonal matrix of coefficients that is solved using linear algebra, a much more computationally efficient method than finding the full steady-state density matrix. We need to solve the equation

$$A\hat{\rho} = \hat{B}, \tag{B.1.3}$$

with

$$\hat{\rho} = \begin{pmatrix} \rho_0^{(1)} \\ \rho_1^{(1)} \\ \rho_2^{(1)} \\ \vdots \end{pmatrix}, \qquad \hat{B} = i\varepsilon \begin{pmatrix} \sqrt{1}\,(\rho_1^{(0)} - \rho_0^{(0)}) \\ \sqrt{2}\,(\rho_2^{(0)} - \rho_1^{(0)}) \\ \sqrt{3}\,(\rho_3^{(0)} - \rho_2^{(0)}) \\ \vdots \end{pmatrix} \tag{B.1.4}$$

and

$$A = \begin{pmatrix} \tilde{k}_0 & \tilde{d}_0 & & & \\ \tilde{c}_1 & \tilde{k}_1 & \tilde{d}_1 & & \\ & \tilde{c}_2 & \tilde{k}_2 & \tilde{d}_2 & \\ & & \tilde{c}_3 & \ddots & \ddots \\ & & & \ddots & \end{pmatrix} \tag{B.1.5}$$

where $\tilde{k}_n = -\frac{\mu_n^{(1)}}{2} - c_n^{(1)} - d_n^{(1)}$, $\tilde{c}_n = c_{n-1}^{(1)}$ and $\tilde{d}_n = d_{n+1}^{(1)}$. Once we have solved for $\hat{\rho} = \rho_n^{(1)}$ we can use this quantity to find the phase distribution. The phase distribution Eq. 3.2.2 is given by

$$P(\varphi) = \frac{1}{2\pi} \sum_{n=0}^{\infty} \sum_{m=0}^{\infty} \rho_{nm} \mathrm{e}^{i(m-n)\varphi}. \tag{B.1.6}$$

We can rewrite this distribution to take into account that we will use the perturbation theory $\rho_n^{(1)}$ rather than the full system density matrix by writing

$$\begin{aligned} P(\varphi) =& \frac{1}{2\pi} \sum_{n=0}^{\infty} (\rho_{n,n} + \rho_{n,n+1} \mathrm{e}^{i\varphi}) \\ &+ \frac{1}{2\pi} \sum_{n=1}^{\infty} \rho_{n,n-1} \mathrm{e}^{-i\varphi}, \end{aligned} \tag{B.1.7}$$

where $\rho_{n,n} = \langle n|\rho|n\rangle$. Then re-summing the last term using $m = n - 1$ we get

$$P(\varphi) = \frac{1}{2\pi} \left(1 + \sum_{n=0}^{\infty} \left[\rho_{n,n+1} \mathrm{e}^{i\varphi} + \rho_{n+1,n} \mathrm{e}^{-i\varphi} \right] \right), \tag{B.1.8}$$

where we have used $\sum_{n=0}^{\infty} \rho_{n,n} = 1$. Finally, we can say that $\rho_{n+1,n} = \rho_{n,n+1}^*$, and returning to the notation $\rho_n^{(k)} \equiv \rho_{n,n+k}$ we have the distribution

$$P(\varphi) = \frac{1}{2\pi} \left(1 + 2\,\mathrm{Re} \left[\mathrm{e}^{i\varphi} \sum_{n=0}^{\infty} \rho_n^{(1)} \right] \right), \tag{B.1.9}$$

which depends on the quantity $\rho_n^{(1)}$ found in Eq. B.1.3 through numerical linear algebra.

B.2 Simplified perturbation theory

Equation B.1.3 is an easier problem to solve numerically than finding the steady state of the full system due to the exploitation of the tridiagonal structure, but we can make further simplifications to the perturbation theory by making some assumptions.

If we carry out a sum over n for both sides of Eq. B.1.2 we obtain

$$\begin{aligned}\sum_{n=0}^{\infty}\dot{\rho}_n^{(1)} = &\sum_{n=0}^{\infty}\left(-\frac{\mu_n(1)}{2}\rho_n^{(1)} - c_n^{(1)}\rho_n^{(1)} - d_n^{(1)}\rho_n^{(1)}\right)\\ &+\sum_{n=1}^{\infty}c_{n-1}^{(1)}\rho_{n-1}^{(1)} + \sum_{n=0}^{\infty}d_{n+1}^{(1)}\rho_{n+1}^{(1)}\\ &-i\varepsilon\sum_{n=0}^{\infty}\left[\sqrt{n+1}(\rho_{n+1}^{(1)} - \rho_n^{(0)})\right].\end{aligned} \tag{B.2.1}$$

However, $d_0^{(1)} = c_{-1}^{(1)} = 0$ so we can simplify Eq. B.2.1 by re-summing the final two terms

$$\begin{aligned}\sum_{n=0}^{\infty}\dot{\rho}_n^{(1)} = &\sum_{n=0}^{\infty} -\frac{\mu_n(1)}{2}\rho_n^{(1)}\\ &+i\varepsilon\sum_{n=1}^{\infty}\left[\sqrt{n+1} - \sqrt{n}\right]\rho_n^{(0)} + i\varepsilon\rho_0^{(0)}.\end{aligned} \tag{B.2.2}$$

Now we make an assumption that both $\rho_n^{(0)}$ and $\rho_n^{(1)}$ have a narrow enough distribution around $\langle n\rangle$ that we may write $-\sum_{n=0}^{\infty}\frac{\mu_n}{2}\rho_n^{(1)} \simeq -\frac{\mu_{\langle n\rangle}}{2}\sum_{n=0}^{\infty}\rho_n^{(1)}$ and $\langle\sqrt{n+1}\rangle \simeq \sqrt{\langle n\rangle + 1}$. In the steady state we now have

$$\sum_{n=0}^{\infty}\rho_n^{(1)} \simeq \frac{2i\varepsilon}{\mu_{\langle n\rangle}(1)}\left(\rho_0^{(0)} + \sqrt{\langle n\rangle + 1} - \sqrt{\langle n\rangle}\right) \tag{B.2.3}$$

where $\mu_{\langle n\rangle}(1)$ is given by Eq. 4.1.12 with $k = 1$ and $n \to \langle n\rangle$. Substituting this into Eq. B.1.9 gives the final simplified version of the phase distribution using perturbation theory,

$$P(\varphi) \simeq \frac{1}{2\pi}\left[1 - 2X\sin\varphi\right] \tag{B.2.4}$$

with

$$X = \frac{2\varepsilon}{\mu_{\langle n\rangle}(1)}\left(\rho_0^{(0)} + \sqrt{\langle n\rangle + 1} - \sqrt{\langle n\rangle}\right). \tag{B.2.5}$$

Appendix C

Two dissipatively coupled micromasers

For two dissipatively coupled micromasers, in addition to the density matrix terms that describe the two uncoupled micromasers A and B, given by Eq. 2.2.1, we have a coupling term

$$L_c\rho = \varepsilon\left[(a-b)\rho(a^\dagger - b^\dagger) - \frac{1}{2}(a^\dagger - b^\dagger)(a-b)\rho - \frac{1}{2}\rho(a^\dagger - b^\dagger)(a-b)\right], \tag{C.0.1}$$

which we can write in the form

$$\begin{aligned} L_c\rho = {} & \varepsilon\left[a\rho a^\dagger - \frac{1}{2}a^\dagger a, \rho\right] + \varepsilon\left[b\rho b^\dagger - \frac{1}{2}b^\dagger b, \rho\right] \\ & - \varepsilon\left[a\rho b^\dagger + b\rho a^\dagger - \frac{1}{2}a^\dagger b, \rho - \frac{1}{2}b^\dagger a, \rho\right]. \end{aligned} \tag{C.0.2}$$

Since we are working in the zero temperature limit, the full master equation of the system now looks like

$$\begin{aligned} \dot{\rho} = {} & N\left[\cos(\phi\sqrt{aa^\dagger})\rho\cos(\phi\sqrt{aa^\dagger}) + a^\dagger\frac{\sin(\phi\sqrt{aa^\dagger})}{\sqrt{aa^\dagger}}\rho\frac{\sin(\phi\sqrt{aa^\dagger})}{\sqrt{aa^\dagger}}a - \rho\right] \\ & + N\left[\cos(\phi\sqrt{bb^\dagger})\rho\cos(\phi\sqrt{bb^\dagger}) + b^\dagger\frac{\sin(\phi\sqrt{bb^\dagger})}{\sqrt{bb^\dagger}}\rho\frac{\sin(\phi\sqrt{bb^\dagger})}{\sqrt{bb^\dagger}}b - \rho\right] \\ & + (1+\varepsilon)\left[a\rho a^\dagger - \frac{1}{2}\left\{a^\dagger a, \rho\right\}\right] + (1+\varepsilon)\left[b\rho b^\dagger - \frac{1}{2}\left\{b^\dagger b, \rho\right\}\right] \\ & - \varepsilon\left[a\rho b^\dagger + b\rho a^\dagger - \frac{1}{2}\left\{a^\dagger b, \rho\right\} - \frac{1}{2}\left\{b^\dagger a, \rho\right\}\right]. \end{aligned} \tag{C.0.3}$$

Until this point we have been evolving the master equation so that

$$\dot{\rho} = \frac{\mathrm{d}\rho}{\mathrm{d}\tau}, \;\; \tau = \gamma t \tag{C.0.4}$$

and using units such that $\gamma = 1$. We can rescale the time so that $\gamma \to \gamma + \varepsilon$ and define

$$\tilde{\varepsilon} = \frac{\varepsilon}{\gamma + \varepsilon}, \;\; \tilde{N} = \frac{N}{\gamma + \varepsilon}. \tag{C.0.5}$$

As we are focussing on the steady-state behaviour, the different time-scaling for the different couplings will not cause any complications. The rescaled master equation can then be written as

$$\begin{aligned}
\dot{\tilde{\rho}} = {} & \tilde{N}\left[\cos(\phi\sqrt{aa^\dagger})\rho\cos(\phi\sqrt{aa^\dagger}) + a^\dagger\frac{\sin(\phi\sqrt{aa^\dagger})}{\sqrt{aa^\dagger}}\rho\frac{\sin(\phi\sqrt{aa^\dagger})}{\sqrt{aa^\dagger}}a - \rho\right] \\
& + \tilde{N}\left[\cos(\phi\sqrt{bb^\dagger})\rho\cos(\phi\sqrt{bb^\dagger}) + b^\dagger\frac{\sin(\phi\sqrt{bb^\dagger})}{\sqrt{bb^\dagger}}\rho\frac{\sin(\phi\sqrt{bb^\dagger})}{\sqrt{bb^\dagger}}b - \rho\right] \\
& + \left[a\rho a^\dagger - \frac{1}{2}\left\{a^\dagger a, \rho\right\}\right] + \left[b\rho b^\dagger - \frac{1}{2}\left\{b^\dagger b, \rho\right\}\right] \\
& - \tilde{\varepsilon}\left[a\rho b^\dagger + b\rho a^\dagger - \frac{1}{2}\left\{a^\dagger b, \rho\right\} - \frac{1}{2}\left\{b^\dagger a, \rho\right\}\right].
\end{aligned} \tag{C.0.6}$$

Appendix D

Semiclassical calculation for two dissipatively coupled micromasers

The master equation of the dissipatively coupled system consists of Eqs. 5.2.3 and 5.2.4 where where $\Lambda^{(k)}_{n,m}$ are the coupling terms.
Defining $\tilde{\Lambda} = \sum_{n,m=0}\sum_{k=1}^{\infty} \mathrm{e}^{ik\varphi_-}\Lambda$ and considering each of the six coupling terms we can rewrite these as

$$\begin{aligned}\tilde{\Lambda} = \frac{\tilde{\varepsilon}}{2}\Bigg[\sum_{k=1}^{\infty}\mathrm{e}^{ik\varphi_-}\sum_{n,m=o}^{\infty}\rho^{(k)}_{nm}\Bigg\{\mathrm{e}^{i\varphi_-}\left[\sqrt{n(m+k+1)}+\sqrt{m(n+k+1)}-2\sqrt{nm}\right]\\ -\ \mathrm{e}^{-i\varphi_-}\left[2\sqrt{(n+k)(m+k)}-\sqrt{(n+1)(m+k)}-\sqrt{(m+1)(n+k)}\right]\Bigg\}\Bigg]\\ -\frac{\tilde{\varepsilon}}{2}\mathrm{e}^{i\varphi_-}\sum_{n,m=0}^{\infty}\rho^{(0)}_{nm}\left[2\sqrt{nm}-\sqrt{n(m+1)}-\sqrt{m(n+1)}\right]. \qquad \text{(D.0.1)}\end{aligned}$$

so that the master equation becomes

$$\begin{aligned}\sum_{k=1}^{\infty}\mathrm{e}^{ik\varphi_-}\sum_{n,m=0}^{\infty}\dot{\rho}^{(k)}_{n,m} = \sum_{n,m=0}^{\infty}\rho^{(0)}_{nm}f_0(\tilde{\varepsilon})\\ +\sum_{k=1}^{\infty}\mathrm{e}^{ik\varphi_-}\sum_{n,m=0}^{\infty}\left[f_1(\tilde{\varepsilon})-\frac{1}{2}\left(\mu^{(k)}_n+\mu^{(k)}_m\right)\right]\rho^{(k)}_{n,m}, \qquad \text{(D.0.2)}\end{aligned}$$

where

$$f_0(\tilde{\varepsilon}) = \frac{1}{2}\tilde{\varepsilon}\mathrm{e}^{i\varphi_-}\left[\sqrt{n(m+1)}+\sqrt{m(n+1)}-2\sqrt{mn}\right] \qquad \text{(D.0.3)}$$

and

$$f_1(\tilde{\varepsilon}) = \frac{1}{2}\tilde{\varepsilon}\left[e^{i\varphi_-}\left(\sqrt{n(m+k+1)}+\sqrt{m(n+k+1)}-2\sqrt{nm}\right)\right.$$
$$\left.-e^{-i\varphi_-}\left(2\sqrt{(m+k)(n+k)}-\sqrt{(m+k)(n+1)}-\sqrt{(n+k)(m+1)}\right)\right]. \tag{D.0.4}$$

Now we can introduce some approximations. Firstly we assume we are in the semiclassical limit so that $\langle n\rangle \gg 1$. We will also assume that we are in a weak coupling regime where $\tilde{\varepsilon} \ll 1$ so that $k \ll n, m$. The final assumption is that the photon number distribution is strongly peaked around its average value so that $n \to \langle n\rangle$. As a result of the assumptions, we approximate k/n, k/m, $1/n$, $1/m$ as small quantities. Additionally we replace n, m, $n+1$, $m+1$ with $\langle n\rangle$. Applying this to Eq. D.0.3 and Eq. D.0.4 we can make the following simplifications

$$\sqrt{n(m+k+1)}+\sqrt{m(n+k+1)}-2\sqrt{nm} \simeq k+1$$
$$2\sqrt{(m+k)(n+k)}-\sqrt{(m+k)(n+1)}-\sqrt{(n+k)(m+1)} \simeq k-1$$
$$\sqrt{n(m+1)}+\sqrt{m(n+1)}-2\sqrt{mn} \simeq 1.$$

Doing the same for $\mu_n^{(k)}$ gives

$$\begin{aligned}\mu_n^{(k)} &\simeq \left[4\tilde{N}\sin^2\left(\frac{k\phi}{4\sqrt{n+1}}\right)+\frac{k^2}{4n}\right]\\ &\simeq \tilde{N}\frac{\phi^2k^2}{4(n+1)}+\frac{k^2}{4n}\\ &\simeq \tilde{D}k^2,\end{aligned} \tag{D.0.5}$$

where $\tilde{D} = \frac{\tilde{N}\phi^2+1}{4\langle n\rangle}$ is the micromaser linewidth. Adding these simplified terms back into the master equation we have

$$\sum_{k=1}^{\infty} e^{ik\varphi_-}\sum_{n,m=0}^{\infty}\dot{\rho}_{n,m}^{(k)} = \frac{1}{2}\tilde{\varepsilon}e^{i\varphi_-}-\sum_{k=1}^{\infty}e^{ik\varphi_-}\sum_{n,m=0}^{\infty}\rho_{n,m}^{(k)}$$
$$\times\left[k^2\tilde{\Delta}-\tilde{\varepsilon}(\cos\varphi_- + ik\sin\varphi_-)\right]. \tag{D.0.6}$$

Finally, knowing that Eq. 5.2.2 can be written equivalently as

$$\dot{P}(\varphi_-) = \frac{1}{2\pi}\left(\sum_{k=1}^{\infty}e^{ik\varphi_-}\sum_{n,m=0}^{\infty}\dot{\rho}_{nm}^{(k)}+\text{c.c.}\right), \tag{D.0.7}$$

and using Eq. D.0.6 and Eq. 3.2.4 we can write the evolution of the phase distribution in the form of a Fokker-Planck equation

$$\begin{aligned}\dot{P}(\varphi_-) = \frac{1}{2\pi}\Bigg\{ & \tilde{\varepsilon}\cos\varphi_- \left[1+\left(\sum_{k=1}^{\infty} e^{ik\varphi_-}\sum_{n,m=0}^{\infty}\rho_{nm}^{(k)} + \text{c.c.}\right)\right] \\ & +\tilde{\varepsilon}\sin\varphi_-\frac{d}{d\varphi_-}\left[1+\left(\sum_{k=1}^{\infty} e^{ik\varphi_-}\sum_{n,m=0}^{\infty}\rho_{nm}^{(k)} + \text{c.c.}\right)\right] \\ & +\tilde{D}\frac{d^2}{d\varphi_-^2}\left[1+\left(\sum_{k=1}^{\infty} e^{ik\varphi_-}\sum_{n,m=0}^{\infty}\rho_{nm}^{(k)} + \text{c.c.}\right)\right]\Bigg\} \end{aligned} \tag{D.0.8}$$

to obtain

$$\dot{P}(\varphi_-) = \left(\frac{d}{d\varphi_-}A_{\varphi_-} + \tilde{D}\frac{d^2}{d\varphi_-^2}\right)P(\varphi_-), \tag{D.0.9}$$

where $A_{\varphi_-} = -\tilde{\varepsilon}\sin\varphi_-$. We can now find the steady-state solution for this Fokker-Planck equation with periodic boundary conditions using Ref. [98] to get

$$P(\varphi_-) = \frac{1}{2\pi I_0(\tilde{\varepsilon}/\tilde{D})}e^{\tilde{\varepsilon}\cos\varphi_-/\tilde{D}}. \tag{D.0.10}$$

Appendix E

Methodology for Many-Body Quantum Synchronisation

We know that in the systems discussed in chapter 6 a bifurcation occurs at a critical coupling strength resulting in a region of bistability of phase locked (synchronised) and unlocked states. This appendix lays out the methods used to obtain the results in that chapter, including details of how the critical points were found and other properties of the phase transition.

We are interested in finding the steady-state solutions to many-oscillator systems to investigate how and when they phase lock. In previous chapters, a steady-state solution has been readily found using the QuTiP toolbox [40, 41] in Python, which utilises a number of different methods to solve the master equation

$$\dot{\rho} = \mathcal{L}\rho, \tag{E.0.1}$$

for example an exact (numerical) matrix diagonalisation or finding the eigenvector of $\mathcal{L}$ that corresponds with its zero eigenvalue. The many-oscillator systems differ in two ways: firstly, due to the mean-field approximation the steady state is found by iteratively updating the quantity $\langle a \rangle$ until convergence; and secondly, the steady state happens to be time dependent. It is this second point that is important – the phase evolution is dynamic, so we can only find the true steady state through numerical integration where $\langle a \rangle$ is updated for each time-step. For this, our tool of choice is the Runge-Kutta method.

E.1 Runge-Kutta Method

Though there are many different existing choices for numerical integration, Runge-Kutta methods are considered amongst the most stable with good accuracy [137].

The general form of the midpoint method to solve an ordinary differential equation $\dot{y} = f(y,t)$ with initial condition y_0 for i iterations is

$$y_{i+1} \approx y_i + sf\left(y_i + \frac{s}{2}f(t_i, y_i), t_i + \frac{s}{2}\right), \tag{E.1.1}$$

where the step size s is determined by $s = (t_{\text{final}} - t_{\text{initial}})/N$ with N the total number of iterations. This second-order method approximates the differential of y_i and y_{i+1} by finding the slope at the midpoint between them. There are various Runge-Kutta methods that are variations on the same principle, for example the fourth-order method, which gives an approximation based on four points between the steps rather than two. The fourth-order method has the advantage that it is usually more stable; however, for the systems we looked at the stability and accuracy were approximately the same for each so the midpoint method was chosen for the advantage in speed.

E.2 Details in Methodology

For the van der Pol oscillators system, the master equation to be solved takes the form (in the Fock basis)

$$\begin{aligned}\dot{\rho}_{n,m} = -i\Big(&\varepsilon^*\langle a^\dagger\rangle\sqrt{n+1}\rho_{n+1,m} + \varepsilon\langle a\rangle\sqrt{n}\rho_{n-1,m} \\ &-\varepsilon^*\langle a^\dagger\rangle\sqrt{m}\rho_{n,m-1} - \varepsilon\langle a\rangle\sqrt{m+1}\rho_{n,m+1}\Big) \\ &+\kappa_1\Big(2\sqrt{nm}\rho_{n-1,m-1} - (n+m+2)\rho_{n,m}\Big) \\ &\kappa_2\Big(2\sqrt{(n+1)(n+2)(m+1)(m+2)}\rho_{n+2,m+2} \\ &- n(n-1)\rho_{n,m} - m(m-1)\rho_{n,m}\Big).\end{aligned} \tag{E.2.1}$$

In the region of bistability, the chosen initial conditions can have an important effect on the final steady state obtained. To map the extent of the bistable region in ε, one technique is to start in the bistable region and

slowly decrease the coupling, using the synchronised state of a slightly higher coupling value as the initial state for a lower value of coupling. Eventually the limit of the bistability will be reached and only an unsynchronised steady state will exist.

However, to investigate other properties of the phase transition it is useful to form a consistent way of generating an initial state that does not depend on steady-state solutions of similar coupling strengths, as often we are trying to find the transition in an unknown location. The method used here was to take an initial value $\langle a \rangle_{\text{init}} = \langle a^\dagger \rangle_{\text{init}} = 1$ and find the state corresponding to the zero eigenvalue of the Liouvillian superoperator, which for both the van der Pol and micromaser systems is the equivalent to the steady state of a single oscillator driven coherently by an external field. For the small values of ε that we use in this chapter it is a suitable choice as this consistently places the initial value of $|\langle a \rangle|$ at slightly higher than the eventual true steady state if it were to lock. This means the phase locking is fairly predictable in that it evolves in approximately the same way each time, even for different values of N, Θ or κ_2/κ_1.

E.3 Errors in the Critical Scaling

An initial estimate for $\varepsilon_{\text{crit}}$ was undertaken by approximately locating where in ε the critical behaviour broke down, then finding the best fit for whichever points remained closer to the transition (seen in Figs. 6.5 and 6.10). This yielded a systematic error where b would decrease as the number of photons in the system increased, most likely due to the narrowing range of the critical region contributing to an increasingly curved line, which then affected the slope value b. This behaviour was seen for both the van der Pol and micromaser systems, and could be misleading in its implied relationship between b and N or κ_2/κ_1. The following alternative approach to estimating b was therefore devised.

The error in b derives from two main sources: the estimated value of $\varepsilon_{\text{crit}}$ and the choice of data points to be fitted linearly. Figure E.1 illustrates the importance in finding $\varepsilon_{\text{crit}}$ with accuracy and precision in order to gain a good estimate of the system close to the transition. Further away from the transition, $\varepsilon_{\text{crit}}$ has very little effect on the shape of the curve, but it becomes

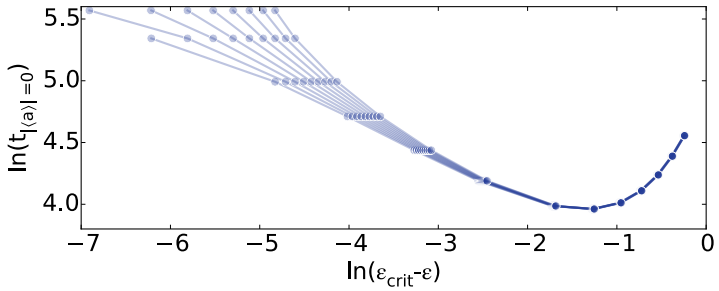


Figure E.1: Showing how the value of $\varepsilon_{\text{crit}}$ affects the shape of the curve in the micromaser system with $N = 20$ and $\Theta = 2$. The different curves use the same data with $\varepsilon_{\text{crit}}$ ranging from 1.278—1.286.

increasingly important as $(\varepsilon_{\text{crit}} - \varepsilon)$ decreases. However, we are required to look in the small $(\varepsilon_{\text{crit}} - \varepsilon)$ region in order to investigate the expected linear behaviour.

A good strategy might be running through a range of $\varepsilon_{\text{crit}}$ then picking the value that returned the "best fit" to a linear model, but there are some extra considerations for this method. The fitted value of b is very sensitive to the choice of points. There is a region of large $(\varepsilon_{\text{crit}} - \varepsilon)$ where a linear fit is clearly inappropriate, but depending on $\varepsilon_{\text{crit}}$, the "most linear" part of the curve can change. Additionally, the number of points chosen influences how well the model fits.

If the systems do indeed exhibit critical power-law behaviour close to the transition, then we should expect two properties: the power-law approximation should consistently improve moving ever closer to the transition in ε, whilst the value of b should converge there. Figure E.2 shows the results of investigating this further in the van der Pol oscillator system. A moving range of five consecutive points is considered, with ε_{max} marking the highest value of ε in that range. For each range a linear model is fitted, and a value of b and coefficient of determination R^2 is extracted, with $R^2 = 1$ denoting zero variance from the model (in the linear case this indicates a perfect correlation). For both (a) and (b), as the selection of points approaches the transition R^2 approaches one, indicating that a linear model is a better description here. For each selection of points $\varepsilon_{\text{crit}}$ is chosen to maximise the fit, and this correspondingly affects the value of b. In the case of $\kappa_2/\kappa_1 = 0.04$, the value of b does not change a lot and hovers around a value of $b = -0.5$. In contrast, for $\kappa_2/\kappa_1 = 0.02$ it starts off as a high value

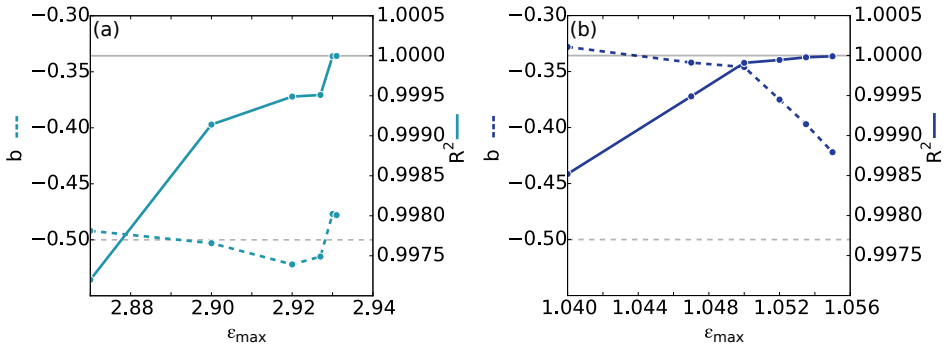


Figure E.2: Fitting a linear model to a range of five consecutive points, with the point closest to the transition denoted by ε_{max}, for (a) $\kappa_2/\kappa_1 = 0.04$ and (b) $\kappa_2/\kappa_1 = 0.02$ in the van der Pol oscillator system. For each selection of points, ε_{crit} is varied until there is a maximum in the coefficient of determination, R^2, and then b is extracted.

and steadily decreases as we approach the transition.

To characterise the total error in b, we use a combination of what we have learnt from Figs. E.1 and E.2. We will define a range in ε_{crit}, and for this range consider the points closest to the transition until the linear model appears to fail. To define the range in ε_{crit}, a lower bound is definite as it is clear which states decay further out from the transition. However, an upper bound is more difficult to define, as the slow timescale decay may have $|\langle a \rangle|$ evolving as slowly as 1×10^{-6} per time-step, making it practically indistinguishable from a true synchronised steady state. We therefore restrict the upper bound by a minimum value in R^2, since we can see from Fig. E.1 that at high/low values of ε_{crit} a curve begins to appear. To keep consistency, we will define both the upper and lower bounds as the maximum and minimum values of ε_{crit} that give a value of $R^2 \simeq 0.99$ when considering four similar data points closest to the transition.

In defining the upper bound in this way, we must accept the potential consequence of artificially truncating the range in b due to not having data points sufficiently close to the transition. There is also the consideration that R^2 is affected by the spacing and number of the points, in addition to how close they are to the true critical point – the relatively low value of $R^2 \simeq 0.99$ was chosen to limit the effect of these factors, with the result of increasing the error in b to a larger range. The only way to reduce this error

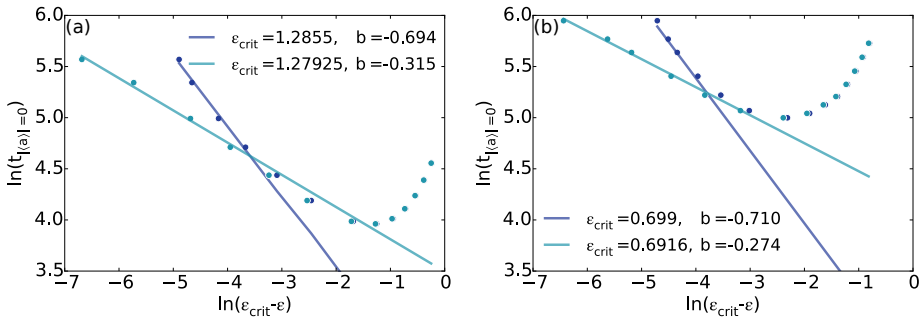


Figure E.3: Showing how the minimum and maximum estimated values of $\varepsilon_{\text{crit}}$ affect the value of the slope b for (a) $N = 20$ and (b) $N = 50$ in the micromaser system with $\Theta = 2$.

would be to obtain more data points even closer to the transition, as this would both improve the precision in $\varepsilon_{\text{crit}}$ and focus on a region that follows the linear behaviour to a better approximation.

Figure E.3 illustrates the range outlined above for two examples in the micromaser system, and shows the relationship between the estimate of $\varepsilon_{\text{crit}}$ and how this affects the calculation of b. We can see that for both values of N, a small change in $\varepsilon_{\text{crit}}$ has a large effect on b, which is also very sensitive to the choice of selection for the fitted points.

This method of finding an error range for b yielded similar results for both the van der Pol oscillator and micromaser system, with $b = -0.5$ falling consistently within the calculated ranges. In the van der Pol oscillator system the ranges were for $\kappa_2/\kappa_1 = 0.04$, $-0.647 < b < -0.373$, and for $\kappa_2/\kappa_1 = 0.02$, $-0.801 < b < -0.279$. The range is larger for the latter, which may reflect the fact that the critical region is narrower for larger numbers of photons (and points closer to the transition are required). However, this effect is not seen systematically in the micromaser system, perhaps due to the choice in points contributing to error ranges that are larger than the effect itself.

References

[1] C. Huygens. *Horologium Oscillatorium [The Pendulum Clock]*. A. F. Muguet, Paris, (1673) [R. J. Blackwell, Transl. Iowa State Univ. Press, Ames, IA, (1986)].

[2] A. Pikovsky, M. Rosenblum, and J. Kurths. *Synchronisation: A Universal Concept in Nonlinear Sciences*. Cambridge University Press, (2003).

[3] A. T. Winfree. *Biological Rhythms and the Behavior of Populations of Coupled Oscillators*. J. Theoret. Biol., **16** 15, (1967).

[4] Z. Jiang and M. McCall. *Numerical simulation of a large number of coupled lasers*. J. Opt. Soc. Am., **10** 155–163, (1993).

[5] R.-d. Li and T. Erneux. *Preferential instability in arrays of coupled lasers*. Phys. Rev. A, **46** 4252, (1992).

[6] A. Steane. *Quantum Computing*. Rep. Prog. Phys., **61** 117–173, (1998).

[7] M. Zhang, G. S. Wiederhecker, S. Manipatruni, A. Barnard, P. McEuen, and M. Lipson. *Synchronization of Micromechanical Oscillators Using Light*. Phys. Rev. Lett., **109** 233906, (2012).

[8] M. Bagheri, M. Poot, L. Fan, F. Marquardt, and H. X. Tang. *Photonic Cavity Synchronization of Nanomechanical Oscillators*. Phys. Rev. Lett., **111** 213902, (2013).

[9] M. H. Matheny, M. Grau, L. G. Villanueva, R. B. Karabalin, M. C. Cross, and M. L. Roukes. *Phase Synchronization of Two Anharmonic Nanomechanical Oscillators*. Phys. Rev. Lett., **112** 014101, (2014).

[10] K. Wiesenfeld, P. Colet and S. H. Strogatz. *Synchronization Transitions in a Disordered Josephson Series Array*. Phys. Rev. Lett., **76** 404, (1996).

[11] K. Wiesenfeld, P. Colet, and S. H. Strogatz. *Frequency locking in Josephson arrays: Connection with the Kuramoto model*. Phys. Rev. E, **57** 1563, (1998).

[12] S. Kaka, M. R. Pufall, W. H. Rippard, T. J. Silva, S. E. Russek and J. A. Katine. *Mutual phase-locking of microwave spin torque nano-oscillators*. Nature., **437** 389–392, (2005).

[13] S.-B. Shim, M. Imboden and P. Mohanty. *Synchronized Oscillation in Coupled Nanomechanical Oscillators*. Science., **316** 5821, (2007).

[14] M. Zhang, S. Shah, J. Cardenas, and M. Lipson. *Synchronization and Phase Noise Reduction in Micromechanical Oscillator Arrays Coupled through Light*. Phys. Rev. Lett., **115** 163902, (2015).

[15] A. Mari, A. Farace, N. Didier, V. Giovannetti, and R. Fazio. *Measures of quantum synchronization in continuous variable systems*. Phys. Rev. Lett., **111** 103605, (2013).

[16] G. Manzano, F. Galve, G. L. Giorgi, E. Hernandez-Garca and R. Zambrini. *Synchronization, quantum correlations and entanglement in oscillator networks*. Sci. Rep., **3** 1439, (2013).

[17] M. Ludwig and F. Marquardt. *Quantum many-body dynamics in optomechanical arrays*. Phys. Rev. Lett., **111** 073603, (2013).

[18] B. Zhu, J. Schachenmayer, M. Xu, F. Herrera, J. G. Restrepo, M. J. Holland and A. M. Rey. *Synchronization of interacting quantum dipoles*. New J. Phys., **17** 083063, (2015).

[19] M. R. Hush, W. Li, S. Genway, I. Lesanovsky and A. Armour. *Spin correlations as a probe of quantum synchronization in trapped-ion phonon lasers*. Phys. Rev. A, **91** 061401(R), (2015).

[20] S. Walter, A. Nunnenkamp, and C. Bruder. *Quantum Synchronization of a Driven Self-Sustained Oscillator*. Phys. Rev. Lett., **112** 094102, (2014).

[21] J. Teramae and D. Tanaka. *Robustness of the Noise-Induced Phase Synchronization in a General Class of Limit Cycle Oscillators*. Phys. Rev. Lett., **93** 204103, (2004).

[22] Y. Lai and M. Porter. *Noise-induced synchronization, desynchronization, and clustering in globally coupled nonidentical oscillators*. Phys. Rev. E, **88** 012905, (2013).

[23] C. Davis-Tilley and A. D. Armour. *Synchronisation of micromasers*. Phys. Rev. A, **94** 063819, (2016).

[24] A. Jenkins. *Self-oscillation*. arXiv:1109.6640v4 [physics.class-ph], (2012).

[25] T. E. Lee and H. R. Sadeghpour. *Quantum Synchronization of Quantum van der Pol Oscillators with Trapped Ions*. Phys. Rev. Lett., **111** 234101, (2013).

[26] T. E Lee, C.-K. Chan, and S. Wang. *Entanglement tongue and quantum synchronization of disordered oscillators*. Phys. Rev. E, **89** 022913, (2014).

[27] N. Lörch, E. Amitai, A. Nunnenkamp, and C. Bruder. *Genuine Quantum Signatures in Synchronization of Anharmonic Self-Oscillators*. Phys. Rev. Lett., **117** 073601, (2016).

[28] B. van der Pol. *On relaxation-oscillations*. The Lond. Ed. and Dub. Phil. Mag. and J. Sci., **2** 7, (1926).

[29] B. van der Pol and J. van der Mark. *Frequency demultiplication*. Nature, **120** 3019, (1927).

[30] A. P. Kuznetsov, N. V. Stankevich, and L. V. Turukina. *Coupled van der Pol-Duffing oscillators : Phase dynamics and structure of synchronization tongues*. Physica D, **238** 1203, (2009).

[31] A. P. Kuznetsov and J. P. Roman. *Properties of synchronization in the systems of non-identical coupled van der Pol and van der Pol-Duffing oscillators. Broadband synchronization*. Physica D, **238**, 1499, (2009).

[32] T. Weiss, S. Walter, and F. Marquardt. *Quantum-coherent phase oscillations in synchronization*. Phys. Rev. A, **95** 041802(R), (2017).

[33] S. Walter, A. Nunnenkamp, and C. Bruder. *Quantum synchronization of two Van der Pol oscillators*. Ann. Phys., **527** 131–138, (2015).

[34] V. Ameri, M. Eghbali-Arani, A. Mari, et al. *Mutual information as an order parameter for quantum synchronization*. Phys. Rev. A, **91** 012301, (2015).

[35] T. Weiss, A. Kronwald, and F. Marquardt. *Noise-Induced Transitions in Optomechanical Synchronization*. New J. Phys., **18** 013043, (2016).

[36] L. Morgan and H. Hinrichsen. *Oscillation and synchronization of two quantum self-sustained oscillators*. J. Stat. Mech., **9** P09009, (2015).

[37] E. Wigner. *On the Quantum Correction For Thermodynamic Equilibrium*. Phys. Rev., **40** 749, (1932).

[38] D. Liebfried, D. M. Meekhof, B. E. King, C. Monroe, W. M. Itano and D. J. Wineland. *Experimental determination of the motional quantum state of a trapped atom*. Phys. Rev. Lett., **77** 4281, (1996).

[39] C. C. Gerry and P. L. Knight. *Introductory Quantum Optics*. Cambridge University Press., (2004).

[40] J. R. Johansson, P. D. Nation, and F. Nori. *QuTiP: An open-source Python framework for the dynamics of open quantum systems*. Comp. Phys. Comm., **183** 1760, (2012).

[41] J. R. Johansson, P. D. Nation, and F. Nori. *QuTiP 2: A Python framework for the dynamics of open quantum systems*. Comp. Phys. Comm., **184** 1234, (2013).

[42] D. Meschede, H. Walther, and G. Müller. *One-atom maser*. Phys. Rev. Lett., **54** 551, (1985).

[43] P. Filipowicz, J. Javanainen, and P. Meystre. *Theory of a microscopic maser*. Phys. Rev. A, **34** 3077, (1986).

[44] E.T. Jaynes and F.W. Cummings. *Comparison of quantum and semiclassical radiation theories with application to the beam maser*. Proc. IEEE, **51**, (1963).

[45] G. Rempe, H. Walther, and N. Klein. *Observation of quantum collapse and revival in a one-atom maser*. Phys. Rev. Lett., **58** 353, (1987).

[46] B.-G. Englert. *Elements of Micromaser Physics*. arXiv:0203052v1 [quant-ph], (2002).

[47] J. P. Garrahan, A. D. Armour, and I. Lesanovsky. *Quantum trajectory phase transitions in the micromaser*. Phys. Rev. E, **84** 021115, (2011).

[48] P. Meystre, G. Rempe, and H. Walther. *Very-low-temperature behavior of a micromaser.* Opt. Lett., **13** 1078, (1988).

[49] M. Weidinger, B. T. H. Varcoe, R. Heerlein, and H. Walther. *Trapping States in the Micromaser*. Phys. Rev. Lett., **82** 3795, (1999).

[50] T. Quang, G. S. Agarwal, J. Bergou, M. O. Scully, H. Walther, K. Vogel and W. P. Schleich. *Calculation of the micromaser spectrum. I. Green's-function approach and approximate analytical techniques*. Phys. Rev. A, **48** 803, (1993).

[51] K. Vogel, W. P. Schleich, M. O. Scully, and H. Walther. *Calculation of the micromaser spectrum. II. Eigenvalue approach*. Phys. Rev. A, **48** 813, (1993).

[52] R. R. McGowan and W. C. Schieve. *Micromaser linewidth*. Phys. Rev. A, **55** 3813, (1997).

[53] M. O. Scully and M. S. Zubairy. *Quantum Optics*. Cambridge University Press, (1999).

[54] M. O. Scully, H. Walther, G. S. Agarwal, T. Quang and W. Schleich. *Micromaser Spectrum*. Phys. Rev. A, **44** 5992, (1991).

[55] W. C. Schieve and R. R. McGowan. *Phase distribution and linewidth in the micromaser*. Phys. Rev. A, **48** 2315, (1993).

[56] F. Casagrande, A. Ferraro, A. Lulli, R. Bonifacio, E. Solano and H. Walther. *How to measure the phase diffusion dynamics in the micromaser.* Phys. Rev. Lett., **90** 183601, (2003).

[57] J. Krause, M. O. Scully and H. Walther. *State reduction and $|n\rangle$-state preparation in a high-Q micromaser.* Phys. Rev. A, **36** 4547(R), (1987).

[58] J. Krause, M. O. Scully, T. Walther and H. Walther. *Preparation of a pure number state and measurement of the photon statistics in a high-Q micromaser.* Phys. Rev. A, **39** 1915, (1989).

[59] S. Qamar, K. Zaheer and M.S. Zubairy. *Generation of steady state squeezing in micromaser.* Opt. Commun., **78** 341, (1990).

[60] O. Benson, G. Raithel, and H. Walther. *Quantum jumps of the micromaser field: Dynamic behavior close to phase transition points*. Phys. Rev. Lett., **72** 3506, (1994).

[61] F. Casagrande, A. Lulli, and V. Santagostino. *Coherently driven and coherently pumped micromaser*. Phys. Rev. A, **65** 023809, (2002).

[62] J. A. Bergou and M. Hillery. *Pump-coupled masers: Transient regime*. Phys. Rev. A, **44** 353, (1991).

[63] J. A. Bergou, M. Hillery, and P. Bogár. *Pump-coupled micromasers: coherent and incoherent coupling*. Opt. Comm., **179** 289, (2000).

[64] S. Rinner, E. Werner, T. Becker, and H. Walther. *Decoherence measurement of two coupled micromasers*. Phys. Rev. A, **74** 041802(R), (2006).

[65] H. Walther. *Entanglement and superposition states in the micromaser*. Phil. Trans. R. Soc. Lond. A, **355** 2343, (1997).

[66] H. Walther, B. T. H. Varcoe, B.-G. Englert, and T. Becker. *Cavity quantum electrodynamics*. Rep. Prog. Phys., **69** 1325, (2006).

[67] D. A. Rodrigues, J. Imbers, and A. D. Armour. *Quantum Dynamics of a Resonator Driven by a Superconducting Single-Electron Transistor : A Solid-State Analogue of the Micromaser*. Phys. Rev. Lett., **98** 067204, (2007).

[68] M. Marthaler, J. Leppäkangas, and J. H. Cole. *Lasing, trapping states, and multistability in a circuit quantum electrodynamical analog of a single-atom injection maser*. Phys. Rev. B, **83** 180505(R), (2011).

[69] F. Chen, J. Li, A. D. Armour, E. Brahimi, J. Stettenheim, A. J. Sirois, R. W. Simmonds, M. P. Blencowe and A. J. Rimberg. *Realization of a single-Cooper-pair Josephson laser*. Phys. Rev. B, **90** 020506(R), (2014).

[70] P. D. Nation. *Nonclassical mechanical states in an optomechanical micromaser analog*. Phys. Rev. A, **88** 053828, (2013).

[71] S. Dambach, B. Kubala and J. Ankerhold. *Generating entangled quantum microwaves in a Josephson-photonics device*. New J. Phys., **19** 023027, (2017).

[72] A. Wallraff, D. I. Schuster, A. Blais, and L. Frunzio. *Strong coupling of a single photon to a superconducting qubit using circuit quantum electrodynamics*. Nat. Lett., **431** 162, (2004).

[73] J. Johansson, S. Saito, T. Meno, H. Nakano, M. Ueda, K. Semba and H. Takayanagi. *Vacuum Rabi Oscillations in a Macroscopic Superconducting Qubit LC Oscillator System*. Phys. Rev. Lett., **96** 127006, (2006).

[74] J. Q. You and F. Nori. *Atomic physics and quantum optics using superconducting circuits.* Nature, **474** 7353, (2011).

[75] R. J. Schoelkopf and S. M. Girvin. *Wiring up quantum systems.* Nature, **451** 664–669, (2008).

[76] D. Beckmann, H. B. Weber, and H. v. Löhneysen. *Evidence for Crossed Andreev Reflection in Superconductor-Ferromagnet Hybrid Structures*. Phys. Rev. Lett., **93** 197003, (2004).

[77] A. Blais, R.-S. Huang, A. Wallraff, S. M. Girvin and R. J. Schoelkopf. *Cavity quantum electrodynamics for superconducting electrical circuits: An architecture for quantum computation*. Phys. Rev. A, **69** 062320, (2004).

[78] O. Astafiev, K. Inomata, A. O. Niskanen, T. Yamamoto, Yu. A. Pashkin, Y. Nakamura and J. S. Tsai. *Single artificial-atom lasing.* Nature, **449** 7162, (2007).

[79] T. J. Harvey, D. A. Rodrigues, and A. D. Armour. *Spectral properties of a resonator driven by a superconducting single-electron transistor*. Phys. Rev. B, **81** 104514, (2010).

[80] A.D. Armour, M.P. Blencowe, E. Brahimi, and A.J. Rimberg. *Universal Quantum Fluctuations of a Cavity Mode Driven by a Josephson Junction*. Phys. Rev. Lett., **111** 247001, (2013).

[81] O. V. Zhirov and D. L. Shepelyansky. *Synchronization and Bistability of a Qubit Coupled to a Driven Dissipative Oscillator*. Phys. Rev. Lett., **100** 014101, (2008).

[82] G. Wendin and V. S. Shumeiko. *Superconducting Quantum Circuits, Qubits and Computing*. arXiv:0508729v1 [cond-mat.supr-con], (2005).

[83] J. D. Cohen, S. M. Meenehan, G. S. MacCabe, S. Gröblacher, A. H. Safavi-Naeini, F. Marsili, M. D. Shaw and O. Painter. *Phonon counting and intensity interferometry of a nanomechanical resonator*. Nature, **520** 522–525, (2015).

[84] M. Aspelmeyer, T. J. Kippenberg and F. Marquardt. *Cavity optomechanics*. Rev. Mod. Phys., **86** 1391, (2014).

[85] M. Eichenfield, R. Camacho, J. Chan, K. J. Vahala and O. Painter. *A picogram- and nanometre-scale photonic-crystal optomechanical cavity*. Nature, **459** 550–555, (2009).

[86] M. Eichenfield, J. Chan, R. Camacho, K. J. Vahala and O. Painter. *Optomechanical crystals*. Nature, **462** 78–82, (2009).

[87] G. Heinrich, M. Ludwig, J. Qian, B. Kubala and F. Marquardt. *Collective Dynamics in Optomechanical Arrays*. Phys. Rev. Lett., **107** 043603, (2011).

[88] P. Orth, D. Roosen, W. Hofstetter, and K. Le Hur. *Dynamics, synchronization, and quantum phase transitions of two dissipative spins*. Phys. Rev. B, **82** 144423, (2010).

[89] M. Xu, D.A. Tieri, E. C. Fine, J. K. Thompson, and M. J. Holland. *Synchronization of Two Ensembles of Atoms*. Phys. Rev. Lett., **113** 154101, (2014).

[90] M. Xu and M. J. Holland. *Conditional Ramsey Spectroscopy with Synchronized Atoms*. Phys. Rev. Lett., **114** 103601, (2015).

[91] S. H. Strogatz. *From Kuramoto to Crawford: exploring the onset of synchronization in populations of coupled oscillators*. Physica D., **143** 1–20, (2000).

[92] J. A. Acebrón, L. L. Bonilla, C. J. Pérez Vicente, F. Ritort, and R. Spigler. *The Kuramoto model: A simple paradigm for synchronization phenomena*. Rev. Mod. Phys., **77** 137, (2005).

[93] M. C. Cross, A. Zumdieck, R. Lifshitz, and J. L. Rogers. *Synchronization by Nonlinear Frequency Pulling*. Phys. Rev. Lett., **93** 224101, (2004).

[94] J. G. Restrepo, E. Ott, and B. R. Hunt. *Onset of synchronization in large networks of coupled oscillators*. Phys. Rev. E., **71** 036151, (2005).

[95] V. I. Arnold. *Mathematical Methods of Classical Mechanics*. [K. Vogtmann, A. Weinstein, Transl.], Springer-Verlag, New York, (1989).

[96] A. Balanov, N. Janson, D. Postnov, and O. Sosnovtseva. *Synchronisation: From Simple to Complex*. Springer, (2009).

[97] G. H. Z. Zheng and B. Hu. *Noise-Enhanced Phase Synchronization of Chaotic Oscillators*. Phys. Rev. Lett., **89** 014101, (2002).

[98] R. L. Stratonovich. *Topics in the Theory of Random Noise: Peaks of random functions and the effect of noise on relays nonlinear self-excited oscillations in the presence of noise*. Gordon and Breach, (1967).

[99] G. H. Z. Zheng and B. Hu. *Phase Slips and Phase Synchronization of Coupled Oscillators*. Phys. Rev. Lett., **81** 5318, (1998).

[100] S. Boccaletti, E. Allaria, R. Meucce, and F.T. Arecchi. *Experimental Characterization of the Transition to Phase Synchronization of Chaotic CO2 Laser Systems*. Phys. Rev. Lett., **89** 194101, (2002).

[101] J. E. Mooij and Yu. V. Nazarov. *Superconducting nanowires as quantum phase-slip junctions*. Nat. Phys., **2** 169, (2006).

[102] W. Schleich and M. O. Scully. *Quantum-noise quenching in the correlated spontaneous-emission laser as a multiplicative noise process. I. A geometrical argument*. Phys. Rev. A, **37** 1261, (1988).

[103] E. Schlottmann, S. Holzinger, B. Lingnau, K. Lüdge, C. Schneider, M. Kamp, S. Höfling, J. Wolters, and S. Reitzenstein. *Injection Locking of Quantum-Dot Microlasers Operating in the Few-Photon Regime*. Phys. Rev. Applied, **6** 044023, (2016).

[104] H. J. Carmichael. *Statistical Methods in Quantum Optics 1: Master Equations and Fokker-Planck Equations*. Springer, (2002).

[105] S. M. Barnett and P. M. Radmore. *Methods in Theoretical Quantum Optics*. Oxford University Press, (1997).

[106] S. M. Barnett and D. T. Pegg. *Quantum theory of optical phase correlations*. Phys. Rev. A, **42** 6713, (1990).

[107] A. Luis and L. L. Sánchez-Soto. *Probability distributions for the phase difference*. Phys. Rev. A, **53** 495, (1996).

[108] F. Galve, G. L. Giorgi, and R. Zambrini. *Quantum correlations and synchronization measures*. In: Fanchini F., Soares Pinto D. Adesso G. (eds) Lectures of Quantum Correlations and their Applications. Springer, 393–420 (2017).

[109] K. Pearson. *Notes on regression and inheritance in the case of two parents*. Proc. R. Soc. Lon., **58** 240–242, (1895).

[110] G. L. Giorgi, F. Galve, G. Manzano, P. Colet and R. Zambrini. *Quantum correlations and mutual synchronization*. Phys. Rev. A, **85** 052101, (2012).

[111] G. Vidal and R. F. Werner. *Computable measure of entanglement*. Phys. Rev. A, **65** 032314, (2002).

[112] M. A. Nielsen, I. L. Chuang. *Quantum Computation and Quantum Information*. Cambridge University Press, (2000).

[113] S. Boccaletti, J. Kurths, G. Osipov, D. L. Valladares and C. S. Zhou. *The synchronization of chaotic systems*. Phys. Rep., **366** 1-101, (2002).

[114] G. L. Giorgi, F. Plastina, G. Francica, and R. Zambrini. *Spontaneous synchronization and quantum correlation dynamics of open spin systems*. Phys. Rev. A, **88** 042115, (2013).

[115] J. D. Cresser, W. H. Louisell, P. Meystre, W. Schleich and M. O. Scully. *Quantum noise in ring-laser gyros. I. Theoretical formulation of problem*. Phys. Rev. A, **25** 2214, (1982).

[116] L. Fabiny, P. Colet, R. Roy, and D. Lenstra. *Coherence and phase dynamics of spatially coupled solid-state lasers*. Phys. Rev. A, **47** 4287, (1993).

[117] C. W. Gardiner. *Handbook of Stochastic Methods*. Springer, (2004).

[118] D. T. Pegg, S. M. Barnett. *Phase properties of the quantized single-mode electromagnetic field*. Phys. Rev. A, **39** 1665, (1989).

[119] B. C. Bag, K. G. Petrosyan and C.-K. Hu. *Influence of noise on the synchronization of the stochastic Kuramoto model*. Phys. Rev. E, **76** 056210, (2007).

[120] J. Jin, D. Rossini, R. Fazio, M. Leib and M. J. Hartmann. *Photon Solid Phases in Driven Arrays of Nonlinearly Coupled Cavities*. Phys. Rev. Lett., **110** 163605, (2013).

[121] M. Schiró, C. Joshi, M. Bordyuh, R. Fazio, J. Keeling, and H. E. Türeci. *Exotic Attractors of the Nonequilibrium Rabi-Hubbard Model*. Phys. Rev. Lett., **116** 143603, (2016).

[122] D. S. Rokhsar and B. G. Kotliar. *Gutzwiller projection for bosons*. Phys. Rev. B, **44** 328, (1991).

[123] S. Puri, C. Kraglund Andersen, A. L. Grimsmo and A. Blais. *Quantum annealing with all-to-all connected nonlinear oscillators*. Nat. Commun., **8** 15785, (2017).

[124] P. M. Chaikin and T. C. Lubensky. *Principles of condensed matter physics*. Cambridge University Press., (1995).

[125] M. Marcuzzi, E. Levi, S. Diehl, J. P. Garrahan, and I. Lesanovsky. *Universal Nonequilibrium Properties of Dissipative Rydberg Gases*. Phys. Rev. Lett., **113** 210401, (2014).

[126] S. H. Strogatz. *Nonlinear Dynamics and Chaos*. Avalon Publishing., (1994).

[127] M. I. Dykman. *Critical exponents in metastable decay via quantum activation*. Phys. Rev. E, **75** 011101, (2007).

[128] W. Casteels, R. Fazio, and C. Ciuti. *Critical dynamical properties of a first-order dissipative phase transition*. Phys. Rev. A, **95** 012128, (2017).

[129] I. Bialynicki-Birula, M. Freyberger and W. Schleich. *Various Measures of Quantum Phase Uncertainty: A Comparative Study*. Phys. Scr., **48** 113–118, (1993).

[130] I. Bialynicki-Birula, J. Mycielski. *Uncertainty relations for information entropy in wave mechanics*. Commun. Math. Phys., **44** 129–132, (1975).

[131] J. Jin, A. Biella, O. Viyuela, L. Mazza, J. Keeling, R. Fazio, and D. Rossini. *Cluster Mean-Field Approach to the Steady-State Phase Diagram of Dissipative Spin Systems*. Phys. Rev. X, **6** 031011, (2016).

[132] S. Diehl, A. Tomadin, A. Micheli, R. Fazio, and P. Zoller. *Dynamical Phase Transitions and Instabilities in Open Atomic Many-Body Systems*. Phys. Rev. Lett., **105** 015702, (2010).

[133] J. J. Mendoza-Arenas, S. R. Clark, S. Felicetti, G. Romero, E. Solano, D. G. Angelakis, and D. Jaksch. *Beyond mean-field bistability in driven-dissipative lattices: Bunching-antibunching transition and quantum simulation*. Phys. Rev. A, **93** 023821, (2016).

[134] N. Lörch, S. E. Nigg, A. Nunnenkamp, R. P. Tiwari, and C. Bruder. *Quantum Synchronization Blockade: Energy Quantization Hinders Synchronization of Identical Oscillators*. Phys. Rev. Lett., **118** 243602, (2017).

[135] S. E. Nigg. *Observing quantum synchronization blockade in circuit quantum electrodynamics*. arXiv:1706.04945 [quant-ph], (2017).

[136] I. S. Gradshteyn and I. M. Ryzhik. *Table of Integrals, Series, and Products*. Academic Press, (2014).

[137] J. D. Faires and R. L. Burden. *Numerical Methods*. Brooks Cole, (2012).